THE ASIAN SUMMER PRECIPITATION OVER THE PAST FIVE CENTURIES

A DISSERTATION SUBMITTED TO THE
GRADUATE DIVISION OF THE
UNIVERSITY OF HAWAI‘I AT MĀNOA
IN PARTIAL FULFILLMENT OF THE
REQUIREMENTS FOR THE DEGREE OF

DOCTOR OF PHILOSOPHY

IN

ATMOSPHERIC SCIENCES/ METEOROLOGY

December 2018

By

Daisy Hui Shi

Dissertation Committee:
Bin Wang, Chairperson
Edward Cook
Fei-fei Jin
Pao-shin Chu
Christina Karamperidou
Makena Coffman

Dedication

To my Savior, my Maker, and my Lord, who lighted up the darkness, gave me a new life, and leads me the way.

Acknowledgements

Gratitude overflows my heart, as I look back the five years of Ph.D. study on this beautiful island of Hawaii.

I am extremely blessed by my academic advisor, Prof. Bin Wang, who taught me not just knowledge, but also attitude to science and to people. He showed me humility, patience and a spirit of always being teachable. I especially thank him for his vision, which sees me when I am not; and for his continuous guidance and encouragement, without which I would never be able to finish. I experienced God's love through him who loves his students to completeness.

I also thank my committee member Prof. Edward Cook, who is very knowledgeable and extremely kind. Though he is residing in New York with time differences, he is always fast responding my emails and kindly help me with all my requests.

I am very grateful for all my committee members for their support and time dedicated: Profs. Fei-fei Jin, Pao-shin Chu, Christina Karamperidou and Makena Coffman.

My gratitude also extends to Profs. Jian Liu and Fei Liu for the fruitful discussions and continuing collaborations.

Many thanks go to my professors at Department of Atmospheric Sciences. I very much enjoyed the ENSO dynamic course taught by Prof. Fei-fei Jin and Prof. Christina Karamperidou. I am also very much benefited by the paleoclimate modeling & proxy syntheses course jointly taught by Prof. Christina Karamperidou and Prof. Jessica Conroy from UIUC.

Gratitude also goes to my colleagues in the department for their daily company, discussion, and help with courseworks; and to my research group members at IPRC for sharing ideas and discussion at group meetings, and enjoying "Happy Day" at luncheons. Especially I want to thank Dr. Tom Robinson for helping me with the synoptic class when I first started learning meteorology; and Dr. Juan Li for helping me with NCL when

I first started research, and continuing helping me in research till now. I also thank Xiao Zhou for helping me preprocess and prepare data. Besides, I thank Mike Gonsalves, Alex Lee and Francis Mai for always ready to help with anything logistic in the department.

I am very grateful for my advisor's wife Aunt Wang, who always puts me in her heart, and always gives me homemade buns every time I visit. Gratitude also goes to Tom and Cowley Robinson, who always invite me to their house every holiday so that I won't be alone.

My good friends and sisters in Christ Yunjie Rao and Ning Li are angels that God sent to me. I am daily blessed by our conversations and prayers. I am also very grateful for Sister Evelyn and her Saturday fellowship. Her teaching and prayers are open doors of God's wisdom and blessings. The prayers and support from the sisters are the source of my strength. Besides, I thank the Campus Fellowship and the First Chinese Church of Christ for giving me a place to worship and serve. Especially I thank Brother Coco Wu for his leading in the worship team.

I thank my dear friends and former roommates Annette Foerster and Eva Kakone for their company and I am grateful for all the fond memories we made together. I thank Dr. Zhiwei Zhu and Xinyi Yang for being the best hiking bodies. My thanks extend to many other friends: Leigh Anne Eaton, Vanessa Almanza, Alyssa Sockol, Nicole Evans, Emma Nuss, Tom and Cowley Robinson, Andy Dewald, Bob and Maureen Ballard, for the good times enjoying the island together and for many pleasant movie/musical nights.

I am also very grateful for my landlords John and Priscilla Kan for their kindness, generosity, and hospitality. They always fill up my refrigerator with food besides providing me a safe and comfortable home on this island. Lastly, I can't say enough thank you to my family for the love, understanding, support and freedom they constantly give me throughout my life. I am truly blessed to have a family like mine.

Abstract

Sparse long-term Asian monsoon (AM) records have limited our ability to understand and accurately model low-frequency AM variability. This dissertation presents a gridded 544-year (from AD 1470 to 2013) Reconstructed Asian summer Precipitation (RAP) dataset by the weighted merging of two complementary proxies including 453 tree ring width chronologies and 71 historical documentary records. Verification against observations and evaluation with various proxies (speleothem, ice core and upwelling) supports the RAP as a valuable dataset for study of large-scale low-frequency Asian summer precipitation variability. Four major modes of variability of the Asian summer precipitation are identified with the long record of RAP, including a biennial El Niño-Southern Oscillation (ENSO) mode, a low-frequency ENSO mode, a central Pacific El Niño-like decadal mode, and an interdecadal mode.

It is shown that the relationship between the RAP and ENSO is ENSO phase-dependent since 1470. Two major modes of *interannual* variability are found to be associated with the ENSO developing and decaying phases, respectively. The mechanisms behind the modern monsoon-ENSO relationship can reasonably well explain the past monsoon behavior. In response to a developing ENSO, precipitation anomalies from the Maritime Continent (MC) via India to northern China are in phase, and this "chain reaction" tends to be largely steady since around 1620 AD; during the decaying phase, however, the summer rainfall-ENSO relationship over the Yangtze River Valley-southern East China (YRV-SEC), the MC and central Asia, has gone through large multidecadal to centennial changes over the past five centuries. The Pacific Decadal Oscillation and ENSO intensity are speculated to be associated with these multidecadal to centennial changes of rainfall-ENSO relations.

An area-averaged All Asian Rainfall Index (AARI) was constructed with the RAP, and significant low-frequency periodicities of the AARI are found on decadal (8-10 years), quasi-bidecadal (22 years), and semi-centennial or multidecadal (50-54 years), as well as centennial time scales. A remarkable abrupt frequency shift from semi-centennial to decadal is detected around AD 1700 across the entire Asian land area, which nearly

concurs with a dramatic upswing of the Indian summer monsoon and AAR. The leading EOF modes on the decadal, multidecadal, and centennial timescales all exhibit a similar spatially uniform structure, suggesting a tendency of in-phase variations among the rainfall over South Asia, East Asia, and MC across the three time scales. The leading mode of the decadal variation of AAR is associated with a mega-El Niño-Southern Oscillation (ENSO) in the Pacific, a cool western Indian Ocean, and a warm North Atlantic and cool tropical South Atlantic. The leading mode of semi-centennial (or multi-decadal) variation exhibits a more spatially uniform pattern and significantly correlated with the reconstructed Atlantic Multidecadal Oscillation (AMO) and the proxy mega-ENSO. Centennial variation of the AAR follows more closely the volcanic forcing variation, while is uncorrelated with solar forcing variability. Both the AARI-mega-ENSO and AARI-AMO relationships are nonstationary and experience significant centennial changes, especially around AD 1700; so is the AARI-volcanic forcing relation.

Table of Contents

List of tables

List of figures

Chapter 1. Introduction

The Asian monsoon (AM) is the most powerful and complex component of the global monsoon system. The thermal contrast between the world's largest landmass (Eurasian continent) and ocean basin (Indo-Pacific Ocean), and the presence of the world's largest high land, the Tibetan Plateau, also known as the third pole, adds to its power in response to the seasonal evolution of the sun. Within the AM system are active interactions among earth's surface, ocean, and atmosphere (Wang 2006a). About two-thirds of the world's population resides in the AM region, where the monsoon rain is the key to agriculture and monsoon prediction is crucial to people's livelihood. However, great challenges remain for the models to accurately predict its seasonal anomalies (e.g., Wang et al. 2009) and its year-to-year fluctuations (e.g., Webster et al. 1998; Webster 2006), and its low-frequency variabilities (e.g., Goswami et al. 2006; Wang et al. 2018) are not yet fully understood.

1.1 Need for long-term Asian monsoon reconstructions and more

The lack of understanding of the AM system, especially on decadal and large spatial scales, is primarily due to the limited number of long-term monsoon records with insufficient spatiotemporal resolution. Instrumental data, which only dates back to a century or so, makes it difficult to investigate the low-frequency (interdecadal to centennial) variability of the AM (Clemens 2006). Existing long-term AM records and reconstructions, usually confined to a specific region due to the limitations of the paleoclimate proxies in use (e.g., Duan et al. 2004; Sinha et al. 2011), are only able to provide partial pictures of the large-spatial scale circulation. A well-calibrated, high spatial resolution reconstruction with full coverage of the AM region is in great need.

The AM interacts with the El Niño-Southern Oscillation (ENSO), and the non-stationarity of their relationship has been recognized as a specter for seasonal forecast

(Webster, 2006). The changes in AM-ENSO relation have been associated with various factors such as anthropogenic warming (e.g., Kumar et al. 1999; Ashrit et al. 2001), interdecadal variations (e.g., Chang et al. 2001; Krishnamurthy and Krishnamurthy 2014; Wang et al. 2008, Li and Wang 2018) and random weakening due to interference by other interannual phenomenon (e.g., Ashok et al. 2001; Ashok and Saji 2007). The answer is not yet clear. A potential better understanding of the cause(s) could be obtained with long data records that cover more cycles of such interdecadal changes under different mean climate state. However, how the monsoon-ENSO relationship underwent secular changes on the interdecadal-centennial timescale beyond instrumental period has rarely been discussed.

Skillful long-term prediction of the monsoon rainfall is required for city infrastructure planning, water resource management, and sustainable development. Since the late twentieth century, the impacts of anthropogenic climate change on monsoon precipitation changes have been studied intensively, and considerable progress has been made (e.g., Meehl et al. 2007; Lee and Wang 2014). In comparison, knowledge and understanding of large-amplitude natural decadal variability remains limited. However, the natural variability of monsoon often overwhelms the anthropogenic trend on the decadal time scale (Wang et al. 2018). Thus, the mechanisms associated with low-frequency internal variability of AM need to be further examined with the help of model simulations and monsoon reconstructions that span centuries.

1.2 Research questions

It is beyond the scope of this dissertation to answer all questions raised in the previous subsection, especially concerning the mechanisms of the AM variability. The major goal of this research is to reconstruct the past Asian summer precipitation (Chapter 2) and to provide a history of its changing relationship with the ENSO (Chapter 3), and to present a comprehensive documentary of its low-frequency variability features across the past five centuries (Chapter 4). Specific questions are address in each chapter as described below.

In Chapter 2: How does the reconstructed Asian summer precipitation (RAP) perform compared with the observations and other proxies? What are the leading modes of

variability of the RAP? How are these modes associated with the global sea surface temperatures?

In Chapter 3: What are the leading interannual modes of variability of the RAP? What are their dynamical origins? To what degree are the proposed mechanisms for the current AM-ENSO relationship applicable to the past AM-ENSO relationship? What could be the causes of the centennial changes of the AM-ENSO relationship in the past?

In Chapter 4: What are the leading periodicities of the Asian summer precipitation and how do they change? What are the leading variability modes of the Asian summer precipitation on the decadal, multidecadal and centennial timescales? How are these low-frequency variations associated with internal coupled dynamic modes and/or external forcing? How do the rainfall-internal and -external forcing relationship change over the past 544 years?

Chapter 2. Asian Summer Precipitation over the Past 544 Years Reconstructed by Merging Tree Rings and Historical Documentary Records

2.1. Abstract

Sparse long-term Asian monsoon (AM) records have limited our ability to understand and accurately model low-frequency AM variability. Here I present a gridded 544-year (from AD 1470 to 2013) Reconstructed Asian summer Precipitation (RAP) dataset by weighted merging two complementary proxies including 453 tree ring width chronologies and 71 historical documentary records. The RAP dataset provides substantially improved data quality compared with single proxy-type reconstructions. Skillful reconstructions are obtained in East and North China, northern India and Pakistan, Indochina Peninsula, mid-latitude Asia, Maritime Continent, and southern Japan. The RAP faithfully illustrates large-scale regional rainfall variability but has more uncertainties in representing small-scale local rainfall anomalies. The RAP reproduces realistic climatology and captures well the year-to-year rainfall variability averaged over monsoon Asia, arid central Asia, and entire Asia during the 20th century. It also shows a general agreement with other proxies (speleothems and ice cores) during the period of 1470-1920. The RAP captures the remarkably abrupt change during the 1600s recorded in an upwelling proxy over the Arabian Sea. Four major modes of variability of the Asian summer precipitation are identified with the long record of RAP, including a biennial El Niño-Southern Oscillation (ENSO) mode, a low-frequency ENSO mode, a central Pacific El Niño-like decadal mode, and an interdecadal mode. In sum, the RAP provides a valuable dataset for study of the large-scale Asian summer precipitation variability, especially the decadal-centennial variability that are caused by the external forcing and internal feedback processes within the Earth climate system.

2.2. Introduction

The Asian monsoon region supports the livelihoods of about two-thirds of the world's humanity. Monsoon rainfall amount, variability and associated climate extremes have been crucial to agricultural production and the welfare of the population for millennia. However, it remains a great challenge for models to accurately predict its seasonal anomalies (e.g., Wang et al. 2009). The year-to-year fluctuations of the monsoon rainfall are generally non-stationary over multi-decadal to centennial time scales (e.g., Webster et al. 1998; Webster 2006). The causes of decadal-centennial variations of the Asian summer monsoon are not well understood (e.g., Goswami et al. 2006; Wang et al. 2018). Limited length of the instrumental data, which only dates back to a century or so, makes it difficult to investigate the interdecadal to centennial variability of the AM (Clemens 2006).

Multiple proxies, including ice cores, tree rings, speleothems, lake sediments and historical documents, have been used to extend the monsoon climate records back in time at annual to decadal temporal resolution (Clemens 2006; Wang et al. 2005a, 2014). But these climate reconstructions have been frequently restricted by the temporal resolution and spatial coverage of the proxies used, which only allows monsoon subsystems to be studied separately on regional scales (e.g. Zhu and Wang 2002; Zhang et al. 2003; Duan et al. 2004; Chen et al. 2011; Yi et al. 2012; Shi et al. 2014; Sinha et al. 2011, 2015, Xu et al. 2013, 2015; Gou et al. 2015; Tan et al. 2015). To assess the regional differences and their linkages to large-scale circulation, a well-calibrated, high spatial resolution reconstruction with full coverage of the Asian continental region is in great need.

Cook et al. (2010) presented the first gridded monsoon reconstruction, the Monsoon Asia Drought Atlas (MADA), for the past millennium based on a spatially extensive tree ring network over the AM region. While the response of incremental tree growth to both soil moisture and temperature variation might be expected to parallel a drought severity index, the Palmer Drought Severity Index (PDSI, Dai et al. 2004) is not an ideal variable to pinpoint the dynamical processes and circulation patterns related to monsoon rainfall variability. It is also noted that the MADA performs poorly in reproducing dry/wet

conditions in East China (Yang et al. 2013a, 2014; Zheng et al. 2014b; Ge et al. 2016; Kang et al. 2014) likely due to the tree-ring data void in this region (Figure 2.1a).

An invaluable resource recording past monsoon variability in East China is the dryness/wetness index. Although the sources of these indices vary (e.g., Bureau 1981; Chinese Academy of Meteorological Science 1981; Zhang 1983; Wang and Zhao 1979), they are all derived from local chronicles across China since 1470 and/or the 500-year flood/drought atlas, and are considered to reflect the changes in the East Asian monsoon rainfall. These indices, combined with other proxies, e.g. tree rings, ice cores, and long-term instrumental measurements, have been used to reconstruct the past boreal warm season (May-September) precipitation for the Asian continent (Feng et al. 2013; Shi et al. 2017b). One of the issues related to such reconstructions, and also discussed in previous studies, is that the documentary data are temporally inhomogeneous. Depending on the availability of the instrumental data at each station, the dryness/wetness index could be derived exclusively from observed precipitation data (Zhang and Liu 1993). This is especially the case for the stations that have relatively long records, whose indices after 1950 are derived from observation alone (Wang et al. 2000b). This means that the calibration using the data for the 1950-1999 period is essentially inadequate. In addition, Feng et al. (2013) incorporated long-term instrumental records from India and South Korea, which might make the reconstruction spatially inhomogeneous.

In this study, I initiated multiple efforts to produce a new long-term monsoon record contributing to the AM reconstruction endeavor. Firstly, I used only tree ring data and historical documentary records in the reconstruction; no individual long instrumental records and other sparsely distributed proxy data were directly used in order to ensure the homogeneity of the reconstruction. Secondly, compared with the previous tree ring network (Cook et al. 2010a), a more comprehensive tree ring dataset was used with additional 126 chronologies (Cook 2015; Cook et al. 2013). Thirdly, a frequency-based reconstruction method was applied to the historical documents to improve their ability to reflect the historical extreme events (Zheng et al. 2014a). An objective extrapolation method was then used basing on the teleconnections between the precipitation in East China and other remote regions. Fourthly, to better avoid signal aliasing (Shi et al. 2013),

instead of directly compositing the tree rings and historical documents, I performed two individual reconstructions first, and then combined them into one dataset by a "correlation skill-based weighting" method. Lastly, I establish the weighting models using the data before 1950, during which the historical documentary records are largely free of the impact of instrumental data so that the impact of instrumental data on the weighting process is minimized.

Section 2 describes how the Reconstructed Asian summer Precipitation (RAP) dataset is generated, including descriptions of the tree rings and historical documents used, and the reconstruction methods. In section 3, the RAP dataset is verified against independent instrumental data from the Climate Research Unit (CRU, Harris et al. 2014) for the early 20th century and the long-term instrumental precipitation records that go back to 1770s (Seoul) and 1810s (India). Section 4 presents an intercomparison between the RAP and other proxies before instrumental period, including speleothem records, ice core records, and a marine upwelling record. The RAP climatology and large-scale interanual-decadal variability during 20th century is also compared with the results derived from another observed dataset compiled by the Global Precipitation Climatology Centre (GPCC, Schneider et al. 2015) (Section 4). The leading modes of variability of the RAP are examined in Section 5. Finally, discussions (Section 6) and conclusions (Section 7) are presented.

2.3. Reconstruction of the Asian summer precipitation: data and methods

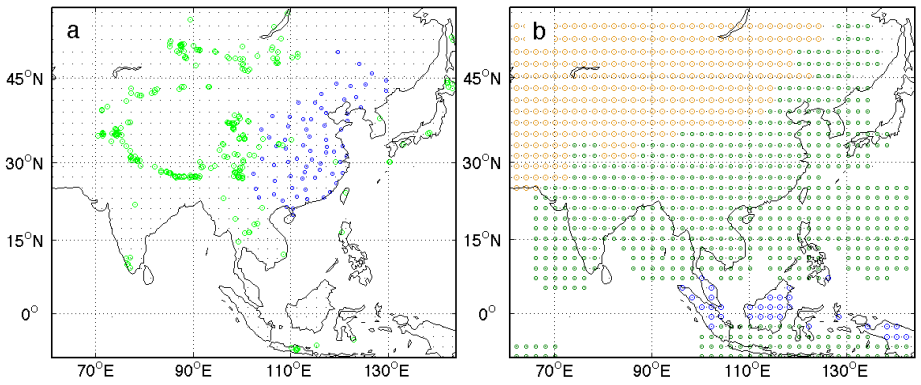

Figure 2.1 (a) Research domain with locations of the 453 tree ring chronologies (green dots) and 71 historical documentary records (blue dots). (b) Monsoon Asia (dark green), arid Asia (dark yellow) and Maritime Continent (blue). The monsoon Asia domain is defined by the following criteria: annual range of precipitation exceeds 300 mm (or 2mm/day); and local summer (May to September) precipitation exceeds 55% of the annual total precipitation (Wang and Ding, 2008). To the northwest side of the monsoon domain is considered the semi-arid/arid region.

The reconstruction domain is shown in Figure 2.1 (from 8.75°S to 55.25°N, and from 61.25°E to 143.25°E), covering the South Asian and East Asian monsoon subsystems, the Maritime Continent (MC), and the semi-arid/arid central Asia. The summer (June-July-August, JJA) precipitation was reconstructed with an annual temporal resolution and a 2 by 2-degree spatial resolution. The datasets used for reconstruction and their temporal spans are shown in Figure 2.2.

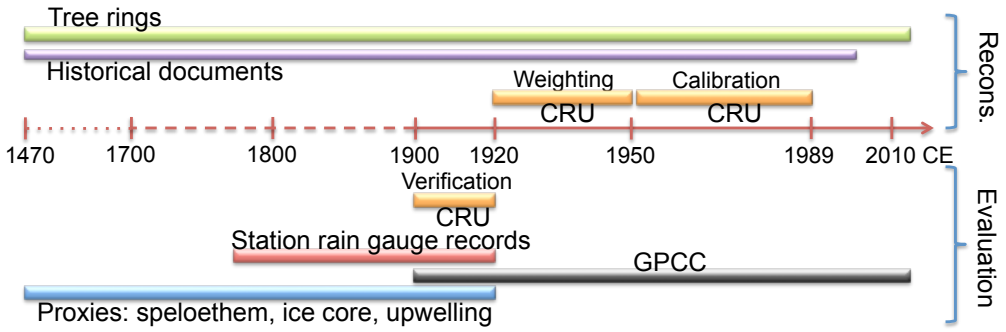

Figure 2.2 Data used for reconstruction and evaluation

2.3.1. The historical documentary records and reconstruction method

The historical documentary records I used are flood/drought level coded data in East China dating back to 1470 (1470-2003, Figure 2.2). The level coded data were derived from a 500-year flood/drought atlas, which was originally defined by five levels: severe flood, flood, normal, drought, and severe drought (Wang and Zhao 1979). Li et al. (2005) added two more levels, i.e. extreme flood and extreme drought by going through local chronicles for extreme climate events, which occur once in 30 years. 71 stations (blue dots in Figure 2.1a) were selected because they have relatively long precipitation records, and are almost evenly distributed across East China (Wang et al. 2000b; Li et al. 2005).

The key to reconstruct precipitation from historical documentary records lies in the occurrence frequencies of the seven drought/flood levels, which are 0.033, 0.100, 0.233, 0.268, 0.233, 0.100, and 0.033, respectively. I used observed JJA mean precipitation over 1951-1989 as a reference. For each station location, the 39-year rainfall series was ordered from maximum to minimum and binned into seven groups to obtain similar frequencies of occurrence mentioned above (i.e., order number 1, 2-5, 6-14, 15-25, 26-34, 35-38, and 39, respectively). For each group, precipitation is then averaged to represent the rainfall amount of the corresponding drought/flood level. With this transformation, annual summer precipitation amount was estimated for the level coded data and extended back to 1470.

The historical documentary records are limited only in East China. To extend the reconstruction from East China onto the whole Asian domain, I applied an objective extrapolation method basing on the teleconnections between precipitation in East China and other remote regions and using stepwise regression. The high-resolution gridded monthly precipitation product CRU TS 3.22 is used for extrapolation. For each grid point outside East China, I correlated the local CRU precipitation series with the 71 time series in East China from 1951 to 1989 (Figure 2.2). I selected significantly correlated time series above the 80% confidence level ($p<0.2$, 2-tailed) as potential "predictors", because the resultant extrapolation was most satisfactory among sensitivity test results for various significance levels. I then applied stepwise multiple linear regression with these

predictors. Stepwise regression is a systematic method for adding and removing predictors from a multi-variable linear regression model based on the statistical significance of their contributions to the overall variance explained by the model (Draper and Smith 1998). I chose the maximum p value for a predictor to be added as 0.05, and the minimum p value for a predictor to be removed as 0.10. Through these procedures, I extended the precipitation series in East China both temporally and spatially to the entire study domain for the past five centuries.

Such extrapolation is not merely a statistical remedy; it does have its physical basis. For instance, there is a robust linkage in summer precipitation among northern East China, India and Maritime Continent. Using 116-year GPCC data (1901-2016), the northern East China summer precipitation has a significant correlation with those over India ($r=0.38$, $p<0.05$) and Maritime Continent ($r=0.49$, $p<0.05$). The stalagmite records from Wanxiang Cave in the northern East China and from Dandak Cave in the central India are shown to vary coherently (Berkelhammer et al. 2010), albeit the ambiguity of the meaning of the speleothem records (e.g., Tan 2016; Chen et al. 2016). Here I assume that the relationship in summer precipitation between East China and other regions is stable over time.

2.3.2. The tree ring network and reconstruction method

The tree ring network I used was achieved through collective effort of many tree ring scientists over decades in developing climatically sensitive tree ring chronologies in the AM region (e.g., Shao et al. 2005; Li et al. 2006; Fang et al. 2010; Gou et al. 2015; Cook et al. 2010b; Yang et al. 2013b). An updated version with a total of 453 tree ring chronologies were used for the reconstruction (Cook 2015; Cook et al. 2013). The earliest starting year of the tree ring series is AD 150, and the common (i.e., earliest) last year of the series is 1989, with most of them clustered after AD 1500. The spatial coverage of the network is limited, due to the intrinsic availability of trees and limited accessibility of existing tree ring chronologies. For example, over central Asia, parts of western China, and the Tibetan Plateau, no forest cover can be found; in lowland tropics, only a few tree species are suitable to sample. It was suggested that a screening procedure for tree ring

chronology is necessary for quality control, because not all of them respond well to the precipitation change in China (Shi et al. 2017b). However, some studies have shown that screening may provide artificial skill (e.g. DelSole and Shukla 2009). Therefore, I did not perform screening before the reconstruction.

I used the tree ring width chronologies, and applied the "point-by-point regression" method (PPR, Cook et al. 1999). PPR is a well-tested principal components regression method, and has produced high quality drought reconstruction over North America (Cook et al. 2007) and over the AM region (Cook et al. 2010a). PPR is based on the proposition that only tree ring chronologies relatively close to a given grid point are likely to have a stable relationship with the climate variables at that location, thus are likely to be true "predictors". Due to the limited spatial coverage of the tree ring network over Asia, to find the minimum amount of tree ring series (here set to 10) for each grid point requires a much larger search radius than the e-folding distance (i.e., 490km, Figure 2.3) of the precipitation correlation decay. Though greatly expanded search radii from 500km up to 3800km were used in reconstructing the summer monsoon precipitation, there are still effective correlations found (Figure 2.3). This is similar to what was done in producing the MADA (Cook et al. 2010a). They assumed that over broad areas with relative low topographic complexity, as the Tibetan Plateau, and the Mongolian steppes, meaningful correlations can be found between tree rings and climate. In area where no trees were available, such as in East China and the Tarim Basin in the western China, the adjacent tree rings can to some degree extrapolate over the void and provide useful climate information.

The calibration data I used is monthly precipitation from CRU TS 3.22. The calibration period was chosen from 1951, to the common last year of the tree ring series, i.e., 1989 (Figure 2.2). Because the data quality of this time period is relatively high compared with that before 1950 (Cook et al. 2010a). The output is a 2 by 2 degrees gridded summer precipitation with full coverage of the Asian land region dated back to AD 1300.

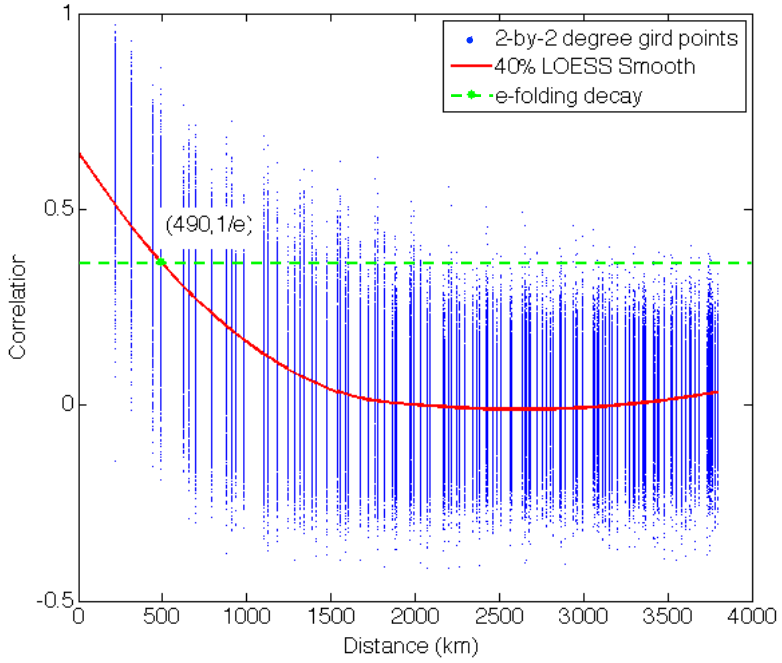

Figure 2.3 Correlation decay with distance for CRU TS 3.22 summer precipitation over the Asian monsoon domain. The data was smoothed using the locally weighted scatter plot smooth (LOESS) method with a span of 40%. The e-folding (1/e) decay in correlation is at the distance of 490km.

2.3.3. Method to combine the two reconstructions

To combine the precipitation reconstruction from tree ring chronologies and that from historical documents into one unified dataset, I applied a correlation skill-based weighting method. The argument is that in the region where one reconstruction has a higher correlation with observation, this reconstruction should be given a higher weight.

As discussed at the beginning, the historical level-coded data are not homogeneous. For the 71 historical documentary records used in this study, the levels were determined solely with instrumental precipitation after 1950. From 1900 to 1950, however, the percentage of instrumental data involved in determining the levels is significantly lower (~34%, Wang et al. 2000). Therefore, I use the period from 1921 to 1950 as the weighting period (Figure 2.2). By doing so, the bias towards putting higher weights on the historical documents can be reduced. Only positive correlations are selected for determining the weights. As such, only grid points with positive correlations are used as

candidates to enter the weighting. In rare cases when both correlations are negative for both reconstructions, I applied equal weights.

As expected, the weights for the tree ring-based and for the historical document-based reconstruction largely complement each other (Figure 2.4), although the highest weights are still found for the historical document-based reconstruction over East China where the original historical documents are obtained (Figure 2.4b). Relatively high correlations are also found over west and south India, showing the teleconnection between the rainfall in east China and in west India. High correlations are also found in the northern part of northeast China, northern part of Indo-China peninsula, and west Borneo for the historical document-based reconstruction. For the tree ring reconstruction, higher weights are found in other geographic regions (Figure 2.4a), where tree ring samples are incorporated. These regions include Siberia, northeast of Kazakhstan, Mongolia, and Hokkaido, Japan; Tajikistan, Kyrgyzstan, north Pakistan and north India; south of the Himalayas including Nepal, Bhutan, Bangladesh, northeast India, and western part of Xinjiang, China; Indo-China peninsula, Malay Peninsula, Sumatra, and west Borneo.

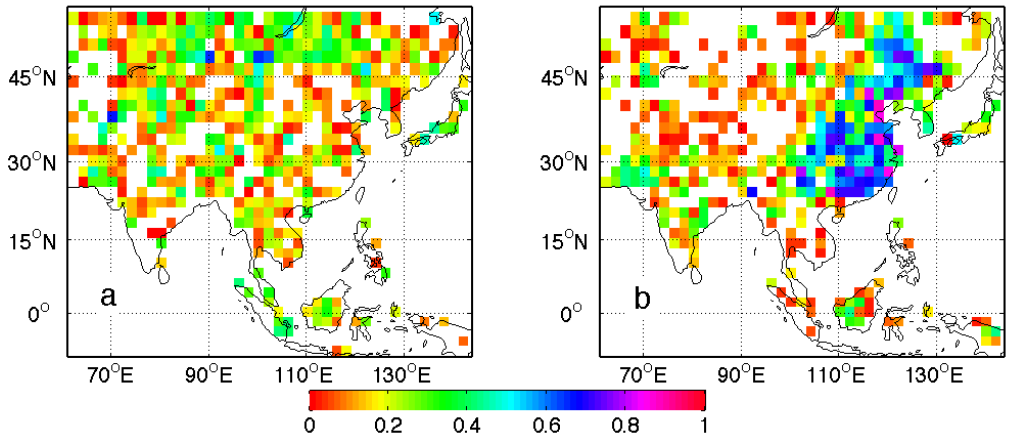

Figure 2.4 Weights assigned to (a) the tree ring-based and (b) the historical document-based reconstruction according to the correlation coefficients between the reconstructed and CRU (Harris et al., 2014) precipitation from 1921 to 1950. Only positive correlations are plotted. Equal weights are applied in rare cases when neither reconstruction has a positive correlation.

The combined reconstruction at each grid can be achieved through the following equation,

$$\mathrm{RECONS}_{combined} = \mathrm{RECONS}_{tr} \times \frac{cor_{tr}}{cor_{tr}+cor_{hist}} + \mathrm{RECONS}_{hist} \times \frac{cor_{hist}}{cor_{tr}+cor_{hist}},$$

where $\mathrm{RECONS}_{combined}$, RECONS_{tr}, and RECONS_{hist} represent combine reconstruction, tree ring-based reconstruction, and historical document-based reconstruction, respectively. cor_{tr} and cor_{hist}denote the correlation coefficients of the tree ring-based and historical document-based reconstruction with CRU data for the period from 1921 to 1950, respectively. The assumption for this combination is that the weights determined by the period from 1921 to 1950 are still valid before 1921.

2.4. Verification of the Reconstructed Asian summer Precipitation (RAP)

2.4.1. Verification of the RAP against CRU (1901-1920) data

The RAP was verified against the CRU precipitation anomalies for the 1901 to 1920 period. The reason for selection of this short period is that data from 1950 to 1989 were used for calibration and the data from 1921 to 1950 were used to determine the weight of merging the two reconstructions (Figure 2.2). The large-scale instrumental precipitation data are available only after 1901. The calibration and weighting processes left only the period from 1901 to 1920 for out-of-sample verification.

The reconstruction skill was evaluated using the standard statistical significance testing, which have been frequently used in previous studies for reconstruction verification (Cook et al. 2010a; Feng et al. 2013; Shi et al. 2017b). They include the square of the Pearson correlation coefficient (RSQ) between observation and reconstruction during the verification period, reduction of error (RE), and the coefficient of efficiency (CE). RE and CE are calculated as,

$$\mathrm{RE} = 1.0 - \left[\frac{\sum(\mathrm{x_i}-\hat{\mathrm{x}}_\mathrm{i})^2}{\sum(\mathrm{x_i}-\overline{\mathrm{x}}_\mathrm{c})^2}\right], \mathrm{CE} = 1.0 - \left[\frac{\sum(\mathrm{x_i}-\hat{\mathrm{x}}_\mathrm{i})^2}{\sum(\mathrm{x_i}-\overline{\mathrm{x}}_\mathrm{v})^2}\right],$$

respectively. $\overline{\mathrm{x}}_\mathrm{c}$ and $\overline{\mathrm{x}}_\mathrm{v}$ are the means of observation during the calibration and verification period, respectively. $\mathrm{x_i}$ and $\hat{\mathrm{x}}_\mathrm{i}$ are the observed and reconstructed values during the verification period, respectively. RE determines if the reconstruction is better than climatology of the calibration period, with RE>0 indicating positive skill of

reconstruction. CE is similar to RE but the values are smaller than RE when $\overline{x}_c \neq \overline{x}_v$. Thus, it is more difficult to pass the test with CE>0 for skillful reconstruction.

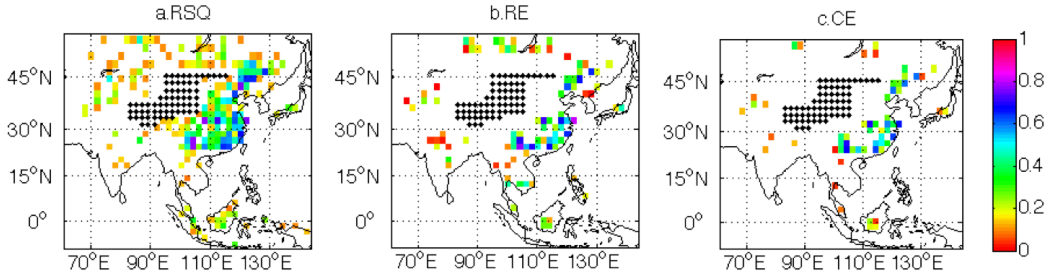

Figure 2.5 Verification statistics for the RAP against CRU from 1901 to 1920. (a) Square of the Pearson correlation coefficient (RSQ), only correlations that are higher than the 90% significance level (1-tailed) are shown. (b) Reduction of error (RE) and (c) coefficient of efficiency (CE), regions with positive skill are shown (RE>0, CE>0). Black doted areas are missing values in CRU dataset during this time period.

Relatively good agreement with RSQ higher than 0.16 ($p<0.1$, 1-tailed), albeit sparse, is found in East and North China, southern Japan, Mongolia, Siberian northeast of Kazakhstan, north Pakistan, and north India, and over the MC, including Borneo, Malay Peninsula, and South Sumatra (Figure 2.5a). However, over various parts of India, regions south of the Tibetan Plateau, and parts of the Indochina Peninsula, the RSQ is largely insignificant (Figure 2.5a). The RE in Figure (4b) shows skillful reconstruction in East and North China, Indochina Peninsula, MC, northern India and Pakistan, mid-latitude Asia, and south Japan. The CE (Figure 2.5c) shows similar spatial distribution of skill, but the magnitudes are lower than that of RE.

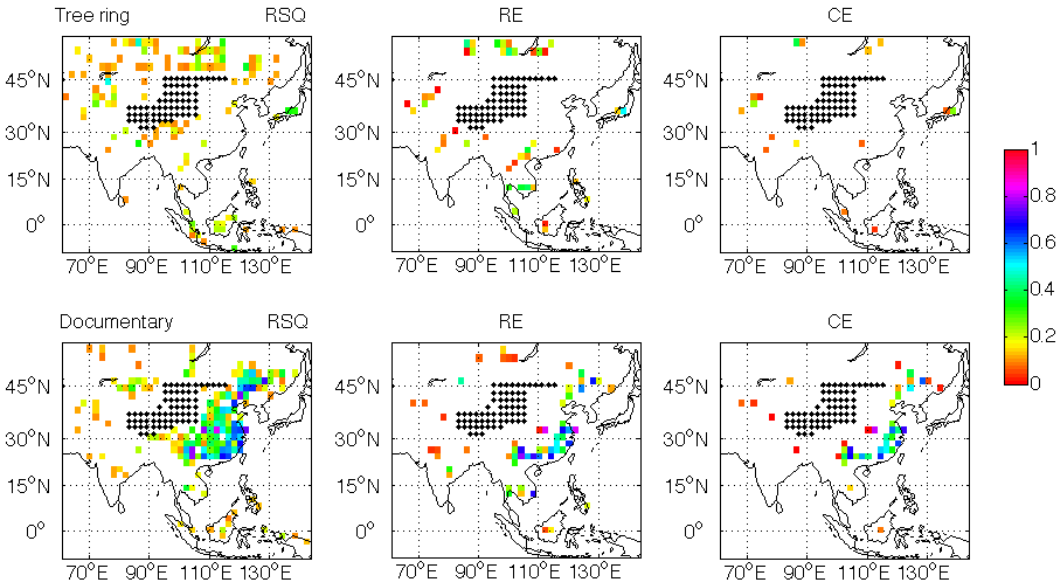

Figure 2.6 Same as Figure 2.5, but for only tree ring (top panel) and only historical document (bottom panel) reconstructions

I also examined individual reconstruction with single-type proxy and to evaluate how much the merged reconstruction has improved the skill. Standard verification statistics are applied to reconstructions with only tree rings and only historical documents, respectively (Figure 2.6). The reconstruction with only tree rings shows skill over middle-latitude Asia, central Asia, northern India, Indochina peninsula, MC, and southern Japan (top panel). The reconstruction with only historical documents shows skill over East China, north central India, and southern Indochina peninsula (bottom panel). The RSQ of the two individual reconstructions are largely complementary with each other. Although the RSQ from tree-ring records is relatively small compared to that produced by documentary records, the combination of the two is shown to have improved reconstruction skill over most of AM region (cf. Figure 2.5, Figure 2.6).

2.4.2. Verification against long-term instrumental data before 1920 (1771-1920)

I further verified the RAP against long-term instrumental records (Figure 2.2). One of such records is the IITM (Indian Institute of Tropical Meteorology) Indian regional/subdivisional Monthly Rainfall dataset dating back to 1813 (Sontakke et al. 2008). This "All-India" record comes from an extensive network of rain gauge stations,

and is area-weighted for India. Another record is from Seoul (37°N, 126°E), South Korea, which is one of the world's longest instrumental measurements of daily precipitation since 1771 (e.g., Wang et al. 2006). This record was compiled from ancient rain-measuring devices used during the Chosun Dynasty, as well as modern rainfall observations since 1908.

Table 2.1 Correlation coefficients between the RAP and long-term instrumental records

Regions (*subregions*)	Time period	Correlation coefficient
All-India	1813-1920	**0.22 (0.30)**
North mountainous India	1844-1920	**0.21 (0.21)**
Northwest India	1826-1920	**0.19 (0.26)**
North central India	1831-1920	**0.26 (0.32)**
Northeast India	1829-1920	0.09 (0.05)
West peninsula India	1817-1920	**0.24 (0.28)**
East peninsula India	1848-1920	**0.30**
South Peninsula India	1813-1920	0.02 (0.03)
Seoul	1771-1920	**0.18** (0.11)

Numbers in parentheses are correlations for the common period 1848-1920. Bold numbers are statistically significant at 90% confidence level ($p<0.1$, 1-tailed). The area for each index is determined based on the definition of each subregion in India (Sontakke et al. 2008, Figure 1), and the location of the record in Seoul.

General agreement is found between the RAP and the long-term rain gage records (Table 2.1). The 108-year All-India record shows significant positive correlation ($r=0.22$, $p=0.02$) with the reconstruction outside of the calibration period. Within India, significant correlations are found over most subregions except the northeast India and southern peninsula. The highest correlation is found in north central region ($r=0.32$, $p<0.1$), followed by eastern ($r=0.30$, $p<0.1$) and western peninsula region ($r=0.28$, $p<0.1$). In Seoul, the correlation coefficient is 0.18 ($p=0.03$), which is reasonably good given the Seoul record is a single station observation and the longest time span of the records from 1771 to 1920.

2.4.3. Sensitivity to parameter choices

As described in section 2, a relatively short weighting period (30 years, 1921-1950) was used for combining the two reconstructions (Figure 2.2). This is constrained by the data availability. The special property of the historical documentary records requires a

weighting model built with data prior to 1950, while the out-of-sample verification requires withholding of data. Therefore, I reserved the available CRU data during 1901-1920 for the out-of-sample verification. To test to what extent the low frequency variability of the precipitation is captured with this short weighting-training period, a reconstruction with longer weighting period (LONG), from 1901 to 1950 is fashioned to compare with this reconstruction (SHORT). The area-weighted index averaged over the entire Asia from LONG is significantly correlated with that from SHORT ($r=0.99$, $p<0.05$). In term of the periodicity, power spectra of the area-weighted indices averaged over Asia from both LONG and SHORT are shown to have preserved low frequency variability, and the locations of all low frequency peaks are the same (Figure 2.7).

Another possible concern is the choice of targeted season of reconstruction. Previous two reconstructions (Shi et al. 2017b; Feng et al. 2013) both aim at warm season (May to September, MJJAS) rainfall. The reason why I chose the JJA mean precipitation is based on (Wang and Zhao 1979). They compared the leading EOF modes using 508-year drought/flood indices from 25 stations located in East China with observed summer precipitation (24 years) from 100 weather stations and found that the spatial patterns of the variability modes are very similar. They concluded that the drought/flood indices could reflect the summer precipitation variability in the East China. I conducted sensitivity tests to compare the reconstructed JJA precipitation variations with the May to September (MJJAS) precipitation variability. The area-weighted index averaged over the entire Asia from JJA reconstruction accounts for almost half (46%) of the total variance of MJJAS rainfall. The correlation coefficient between the JJA and MJJAS indices reaches 0.94 ($p<0.05$), indicating that at least on large spatial scale, the JJA precipitation variations could largely reflect the MJJAS precipitation variability in the research domain.

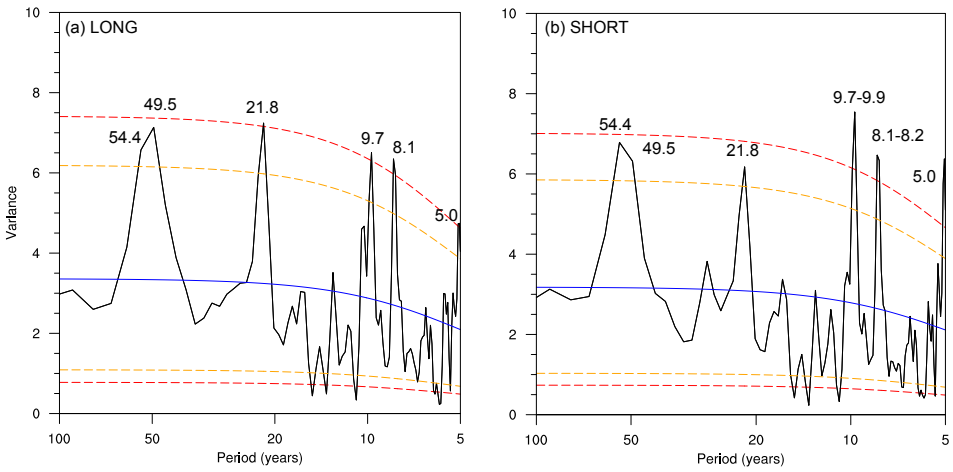

Figure 2.7 Periodicity of the reconstructed AM indices with (a) long and (b) short weighting period. The power spectra are derived by using forward Fast Fourier transformation, with 10% of the data tapered, and the modified Daniell window with a span of 4. Blue lines are the Markov Red Noise spectra. Red and orange dash lines indicate upper (lower) confidence bounds at 95% and 90% significance levels, respectively.

2.5. Further evaluation of the RAP

2.5.1. Intercomparison between the RAP and GPCC climatology and large-scale precipitation indices

The RAP climatology was compared with that derived from the GPCC monthly precipitation dataset from 1901 to present (Figure 2.2). As shown in Figure 2.8, the climatological mean of the reconstruction (Figure 2.8d) resembles that from the corresponding observation (Figure 2.8a) with a pattern correlation coefficient (PCC) of 0.89. Note that the reconstruction mean is essentially the CRU climatology from 1951 to 1989, i.e. the calibration period, because the reconstructed variable is rainfall anomaly. The standard deviation from the RAP (Figure 2.8e) is overall less in amplitude compared with that from the observation (Figure 2.8b), especially over Indo-China peninsula and the Tibetan Plateau, but the PCC between the two is reasonably good (0.76). However, for the verification period, the discrepancy over the Tibetan Plateau increases (Figure 2.8c, f) and the PCC drops to 0.57.

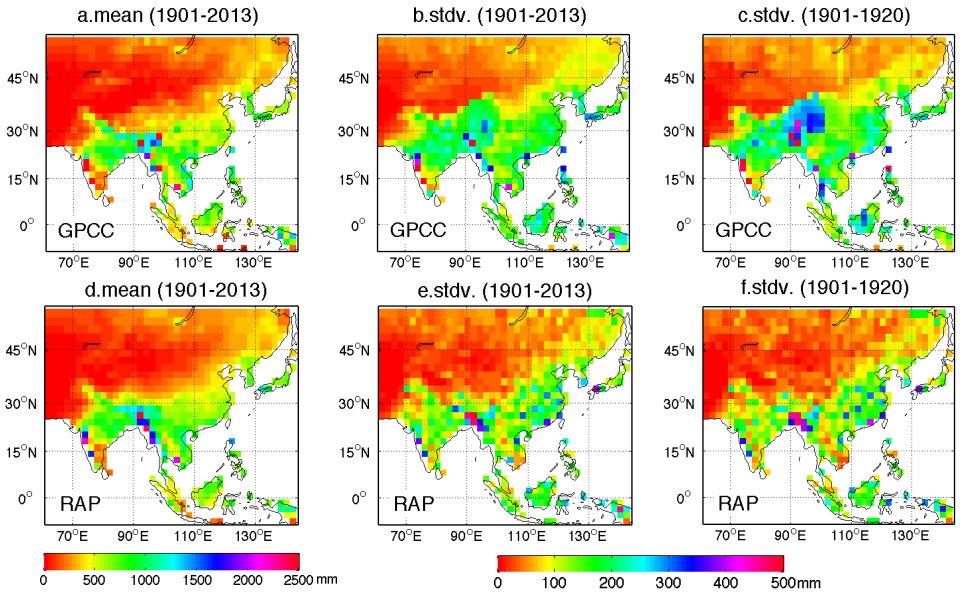

Figure 2.8 20th century climatological mean and standard deviation for the GPCC and RAP

Large-scale precipitation variability is represented by area-weighted mean RAP indices in Figure 2.9. Over all Asia, the reconstructed Asian precipitation index is significantly correlated with that from the GPCC with a correlation coefficient of 0.73 ($p<0.05$) for the 20th century and 0.67 ($p<0.05$) for the verification period (1901-1920) (Figure 2.9a). The Asian domain was further divided into monsoon Asia, arid Asia, and the MC (Figure 2.1b). The definition of monsoon domain follows Wang and Ding (2008).

For monsoon Asian precipitation index, the correlations are consistently high: 0.69 ($p<0.05$) for the 20th century, and 0.66 ($p<0.05$) for the verification period of 1901-1920 (Figure 2.9b). The high correlation in the monsoon Asian is likely attributed to the inclusion of abundant historical records in East China (Figure 2.1a). For arid central Asia, the area-weighted mean precipitation index shows fairly good relationship with the observed counterpart with $r= 0.66$ ($p<0.05$) for the 20th century and $r= 0.45$ ($p<0.05$) for the verification period. This indicates that tree rings and teleconnections have contributed to the RAP's improved representation of the rainfall variability outside the historical record-dense region in East China. Slightly lower correlations, albeit significant, are found over the MC ($r=0.60$, $p<0.05$), which is possibly due to lack of proxy samples.

These results suggest that the RAP can effectively capture large-scale rainfall variability in different parts of Asia during the 20th century. Yet the skill varies over the study region because of the differences in proxy coverage, proxy type, and the extent to which the climatological regime is driven in the region by large-scale factors.

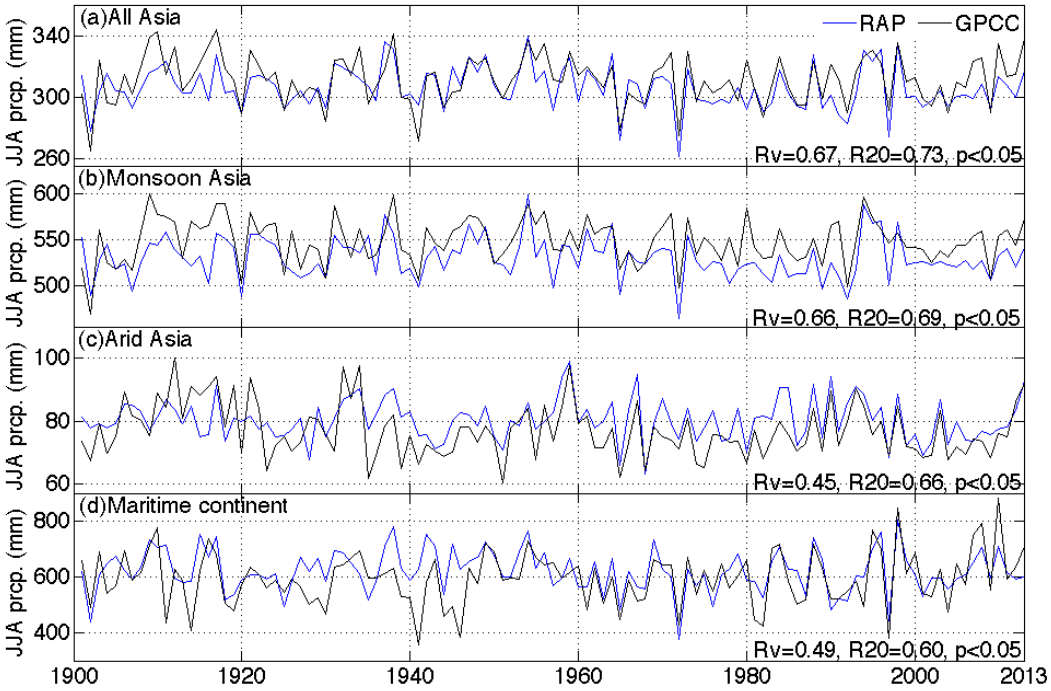

Figure 2.9 Comparison of the area-weighted precipitation indices derived the RAP (blue) and GPCC (black) for (a) all Asia, (b) monsoon Asia, (c) arid Asia and (d) maritime continent. Rv is the correlation coefficient during verification period (1901-1920); R20 is the correlation coefficient during the 20th century.

2.5.2. Intercomparison between the RAP and other proxies during 1470-1920

To evaluate the quality and reliability of the reconstruction before 1920, I further compared RAP to various published monsoon proxies, including eight speleothem $\delta^{18}O$ records from caves across AM region, three ice core records from the central Himalayas and Tibetan Plateau region, and one upwelling record from Arabian Sea (Figure 2.2). Speleothem $\delta^{18}O$ series have been used as proxies of monsoon variability in Asia, and negative correlations are expected between speleothem $\delta^{18}O$ series and precipitation anomalies (e.g., Xu et al. 2013, 2015; Gou et al. 2015; Tan et al. 2015). Ice core records have been shown to reflect past climatic conditions, large climate events, as well as

temperature and moisture variability (Thompson et al. 2006a). Monsoon intensity changes in particular have been associated with ice core dust and chloride concentrations, aerosol history, and snow accumulation (Thompson et al. 2000; Duan et al. 2004; Thompson et al. 2006b). In this study, I used the most straightforward variable, which is snow accumulation (Thompson et al. 2000; Duan et al. 2004), and positive correlations are expected with the monsoon reconstruction. For each proxy record, a 5 by 5 grid box centered at the location of the proxy is selected to calculate time series with the RAP. The size of the box is determined based on the correlation decay e-folding distance, which is 490 km (roughly 2.2 of the 2-degree grids). Pentad time series (average over every five year) from 1470-1920 are used to examine relationships on the decadal time scale.

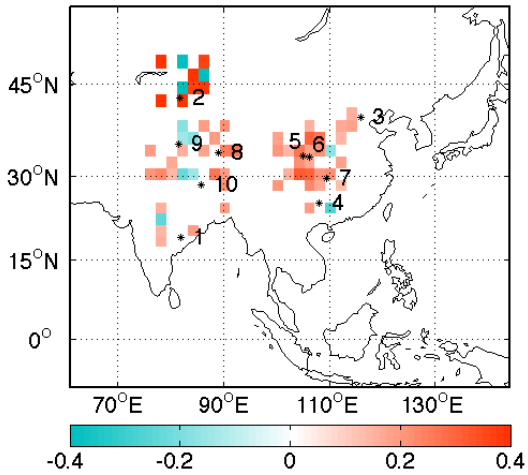

Figure 2.10 Comparison of RAP and proxy data. Shown are the correlation coefficients between the RAP and proxies (speleothem $\delta^{18}O$ records and ice core snow accumulation records) for the period of 1470-1900. Only significant correlations above the nominal 80% confidence level (2-tailed) are shown. List of names of the caves are: Cave 1, Jhumar and Dandak (Sinha et al. 2011); Cave 2, Kesang (Cheng et al. 2012); Cave 3, Shihua (Li et al. 1998); Cave 4, Dongge (Wang et al. 2005b); Cave 5: Wanxiang (Zhang et al. 2008) and Huangye (Tan et al. 2011); Cave 6: Dayu (Tan et al. 2009); Cave 7: Lianhua (Cosford et al. 2009). List of names of the ice cores are: Core 8, Puruogangri (Thompson et al. 2006b); Core 9, Guliya (Thompson 1997); Core 10, Dasuopu (Thompson et al. 2000).

The RAP shows overall agreement with speleothem and ice core records on decadal time scale, where warm color indicates negative (positive) correlation with speleothem (ice core series) (Figure 2.10). 83% of all the grid points show significant agreement ($p<0.2$,

1-tailed) with the other proxies. In comparison, the percentage of grids in agreement with proxies is 66% for the tree-ring only, and 76% for the historical-document only reconstructions (Figure 2.11), indicating an improvement of fidelity of the combined RAP. Agreement is found for most of the adjacent areas of all eight caves in central and northwest China and India and three ice cores located in central Himalayas and Tibetan Plateau (Figure 2.10). However, discrepancies remain in several places, including north of Kesang Cave in northwest China, near Dongge Cave in south China, near Guliya in Tibetan Plateau, and near Dasuopu ice cores in central Himalayas.

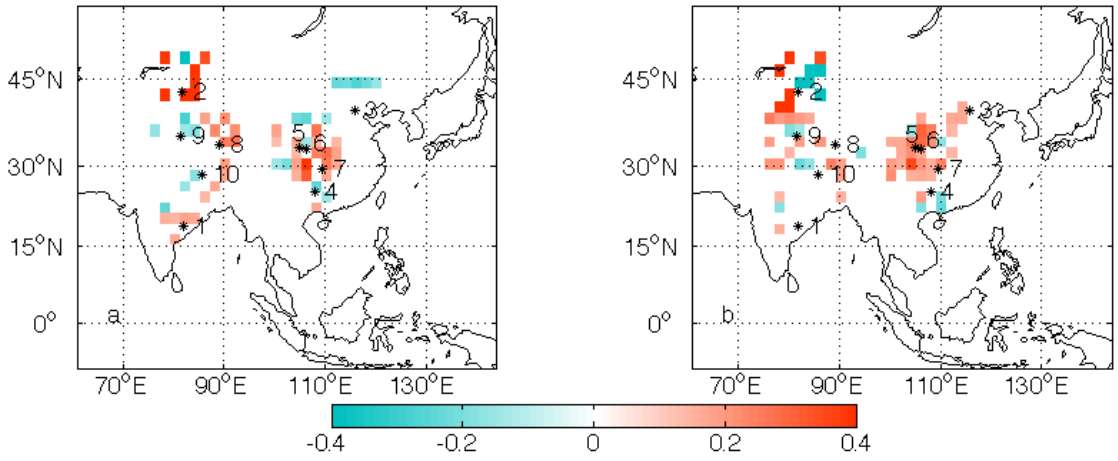

Figure 2.11 Same as Figure 2.10, but for (a) tree ring only and (b) historical record only reconstructions

The RAP was also compared with a 1000-year upwelling proxy record from the Arabian Sea (Anderson et al. 2002). The upwelling record is interpreted as a low frequency (50-year interval) Asian southwest monsoon index, which shows that the monsoon upwelling reached a minimum around 1600, and increased afterwards with a relatively rapid rate to around 1700. The low-frequency variations of the RAP show a salient strengthening of the Indian summer monsoon (ISM) that had occurred during 1630-1670 (Figure 2.12a). Before this increase at the turn of 1600, strong dry anomalies are shown over India, especially over western peninsula India during the period of 1580-1630 (Figure 2.12b). The time series of the area-averaged summer rainfall over India (Figure 2.12c) further illustrate the multidecadal changes of the ISM during the past 500 years. It is noted that the northern East China also strengthened as the ISM increase (Figure 2.12a). During the

dry phase of the ISM, other parts, including South-Central China, northern East China, and the MC also experience dry conditions (Figure 2.12b).

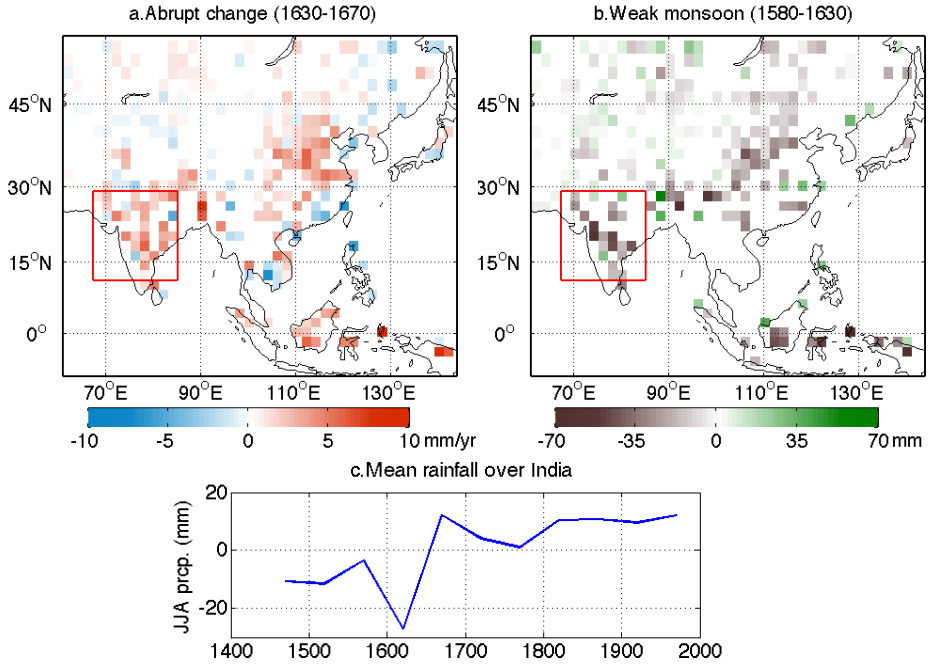

Figure 2.12 (a) Linear trends during 1630 to 1670; (b) Summer precipitation anomalies during 1580 to 1630 derived the RAP dataset. Only significant trends/anomalies above the 80% confidence level (2-tailed) are plotted. (c) 50-year smoothed summer precipitation averaged over India (red box).

2.6. Leading modes of the year-to-year variability of the RAP

To examine the long-term variability of the Asian summer precipitation, I utilized the full span of the RAP dataset. An empirical orthogonal function (EOF) analysis is applied to the yearly RAP data after spatially smoothing (3 grids in latitudinal and 5 grids in longitudinal), area weighting, and standardization (Figure 2.13, Figure 2.14). The linkages of the principal components (PCs) with global sea surface temperatures (SSTs) are examined to understand their origins (Figure 2.15). The SST data used is from the Hadley Center Sea Ice and Sea Surface Temperature dataset (HadISST, Rayner 2003) from 1870 to 2013.

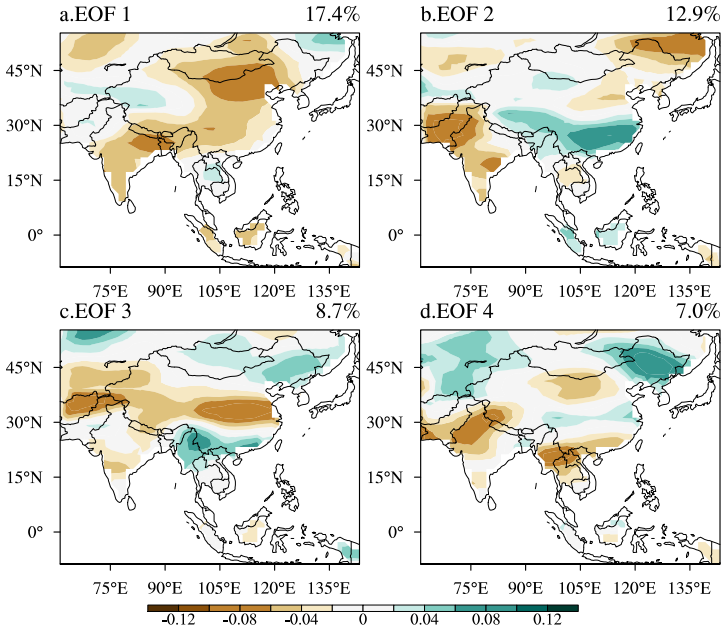

Figure 2.13 Spatial patterns of the leading EOFs of the RAP. The total explained variance of these four EOFs is 46.0%.

The first EOF mode shows a generally uniform drying pattern over most parts of the AM region, including India, East China and the MC (Figure 2.13a). It explains 17.4% of the total variance. The PC1 is correlated with a La Niña-like cooling pattern in the preceding winter (Figure 2.15, first column), which disappears during the spring, and from summer to the following winter an El Niño-like SST pattern develops, suggesting that the unified drying pattern is associated with the eastern Pacific El Niño developing process, or a transition from a cold to a warm phase of ENSO. Spectral analysis indicates that PC1 has significant peaks ranging from 2 to 3 years (Figure 2.14), reflecting its association with the biennial or high-frequency component of ENSO (Figure 2.15, first column). This mode can be properly identified as a biennial ENSO mode.

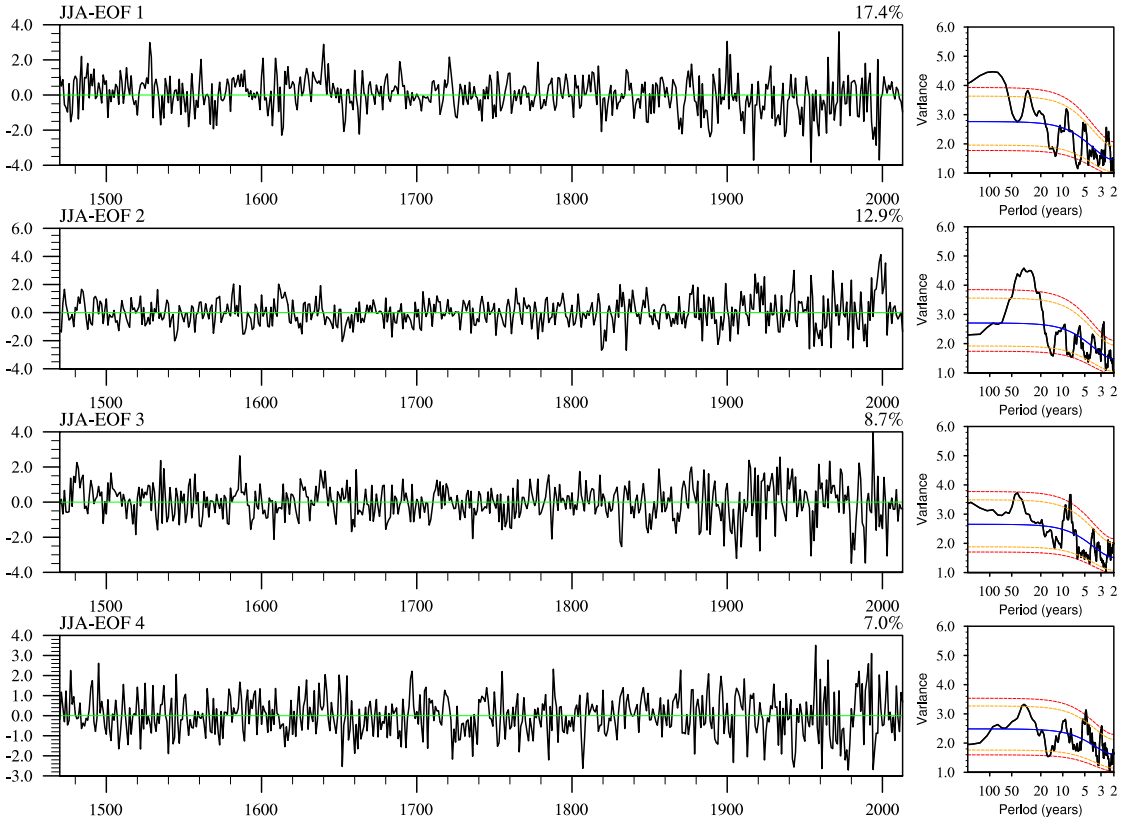

Figure 2.14 PCs and their power spectra derived by using forward Fast Fourier transformation, with 10% of the data tapered, and the modified Daniell window of span of 20. Blue lines are the Markov Red Noise spectra. Red and orange dash lines indicate upper (lower) confidence bounds at 95% and 90% significance levels, respectively.

In comparison, EOF4 is also found associated with eastern Pacific El Niño events (Figure 2.15, forth column). The difference is that during the preceding winter, the ocean conditions are El Niño-like rather than La Niña-like, and the eastern Pacific warming is long-lasting throughout the year till the following winter. Spectrum of PC4 shows a pronounced 5-year peak that passes the 95% significance level, reflecting its association with the low-frequency component of ENSO (Figure 2.14), as reflected by the relatively slow development of El Niño (Figure 2.15, forth column). Therefore, this mode is identified as the low-frequency ENSO mode. Drying over India and Indo-China peninsula is observed, and a quadrupole pattern over the East Asia is found (Figure 2.13d).

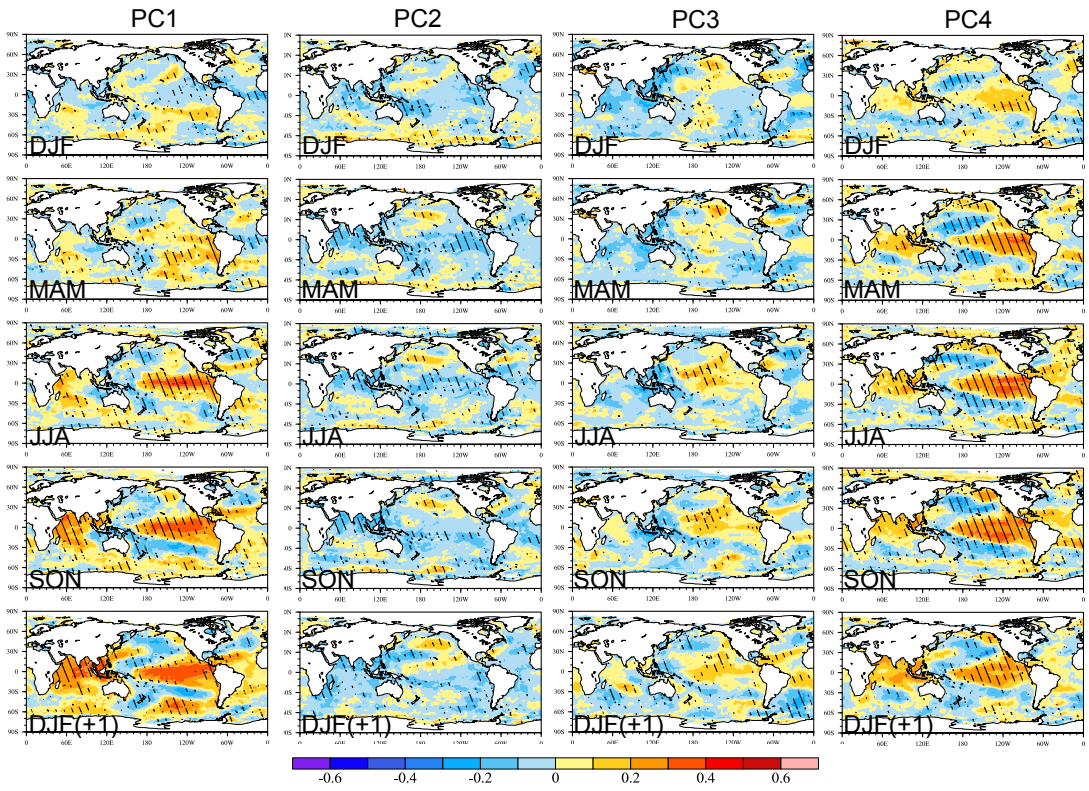

Figure 2.15 Spatial patterns of correlations with global SSTs for each PC from 1871 to 2013. Each column represents correlations for one PC; from top to bottom shown are seasonal evolutions of the PC-SST relations. Hatched areas are significant correlations at 80% level and higher (2-tailed).

EOF3 shows a tripole pattern over the East Asian land, and drying over the western China and north of India (Figure 2.13c). It explains 8.7% of the total variance. The PC3 is associated with the central Pacific (CP) warming that develops from the summer and sustains to the winter (Figure 2.15, third column). The major periodicity of PC3 is around 9 years (Figure 2.14). I identify this mode as a CP El Niño-like decadal mode.

EOF2 has a strong loading over the Yangtze River Valley (YRV) where the major subtropical frontal zone is located, and over South China. Loadings of the opposite sign are found over the India and Pakistan, and northeast Asia (Figure 2.13b). It explains 12.9% of the total variance. This mode does not seem to relate with ENSO (Figure 2.15, second column). Rather, PC2 is significantly correlated with anomalous SSTs over the Indian Ocean and mid-latitude North Pacific Ocean (Figure 2.15, second column). The spectrum of PC2 shows very strong peaks in the 20- to 50-year periods (Figure 2.14). Thus, I

conclude EOF2 is an interdecadal mode that is likely associated with oceanic low-frequency variability modes. The behavior of the major modes of variability revealed from RAP will be compared with those derived from other reconstructions in the next section.

2.7. Discussion

While the RAP represents large-scale precipitation anomalies with acceptable fidelity, its uncertainty increases toward small and local scales. Major uncertainties in assessing the fidelity of the RAP exist over the central Asia, southern and northeastern India, and regions south of the Tibetan Plateau (Figure 2.5). For the central Asia, uncertainty is partially due to the reduced quality of the CRU data (Cook et al. 2010b, 2013) and lack of observations in this area before 1920 (Figure 2.5). For regions including southern and northeast India, Nepal and Bangladesh, the high uncertainty of the reconstruction is likely due to a combination of lack of trees, low teleconnection with other parts, and high variability of local rainfall related to the vigorous air-sea interaction over the Bay of Bengal and topography. Therefore, local and small-scale rainfall anomalies derived from the RAP should be interpreted with caution.

There is some degree of mismatching between the reconstruction and other proxies (Figure 2.10). The mismatching with speleothem records, could be partially due to the obscure interpretation of the climate meaning of the oxygen isotope from the speleothem records raised in the recent studies (e.g. Chen et al. 2016; Tan 2016). The disagreement with the ice core record could arise from multi-sources. For instance, the ice flow dynamics could impact snow accumulation in ice core records (Thompson et al. 2000); and uncertainties associated with age models and dating methods in ice core records could also contribute to the disagreement (Clemens 2006).

The RAP agrees with the upwelling record on the timings of weak ISM and the rapid ISM strengthening (Figure 2 in Anderson et al. 2002). Similar increase is also found in speleothem records from central India (Sinha et al. 2011). But the duration of the monsoon-increasing period shown in the RAP (40 years) is shorter than that shown in the upwelling record (about a century), which could be due to much lower temporal

resolutions of the upwelling record in comparison to the RAP. Such comparison of the durations remains very difficult.

Differences in the interpretation of the major modes of Asian summer precipitation variability are noticed. Cook et al. (2010a) discussed the major variability modes of the MADA using Distinct EOF (DEOF) analysis. The MADA DEOF1 shows wet conditions over India and Southeast Asia (Figure 3 in Cook et al., 2010), which was found associated with La Niña conditions. DEOF4 shows strong positive loading over the Tibetan Plateau, and it is associated with El Niño conditions. The MADA DEOF1 largely resembles the RAP EOF4, and the DEOF4 is likely corresponding to RAP EOF1. Besides the differing relative importance of these modes, some fine spatial features in East Asia are less evident in the MADA compared with the RAP. For example, the clear quadrupole pattern over East Asia depicted in RAP EOF4 is very weak in MADA DEOF1. In MADA DEOF4, the wetting over the YRV during an El Nino condition might not be accurate (e.g., Yang et al. 2013, 2014), in comparison with the unified drying over East China in the RAP EOF1. Li et al. (2014) showed similar MADA EOF patterns as Cook et al. (2010), but both studies only discussed two modes of variability, without discussing the periodicity of the PCs. Compared to the MADA, the RAP provides a more comprehensive and perhaps more accurate description of the variability modes of the Asian summer precipitation in terms of a long reconstruction record.

Although the reconstruction made by Shi et el. (2017) is confined to China while RAP covers entire Asia, they share very similar spatial patterns of the leading EOFs over China. Both reconstructions show a uniformed EOF1 pattern, a dipole EOF2 pattern, and a tripole EOF3 pattern (Figure 8 in Shi et al., 2017). Shi et al. (2017) showed a significant connection between the Pacific Decadal Oscillation (PDO) and the low-frequency PC2 (9-year running average), which agrees with the RAP EOF2 as the interdecadal mode associated with mid-latitude northern Pacific Ocean SST variations. However, I don't think this mode is associated with ENSO as suggested by Shi et al. (2017). Besides, the dynamical origins of the EOF1 and EOF3 of RAP have been attributed to the biennial ENSO and CP El Niño-like decadal Pacific variability (Figure 2.14, Figure 2.15), respectively, which are novel in the literature.

2.8. Conclusions

A 544-year gridded (2 by 2 degree) summer (JJA) precipitation dataset was reconstructed for Asia (8.75°S-55.25°N, 61.25°E-143.25°E) using the complementary tree ring chronologies and historical documentary records. The PPR method was used for reconstruction with the tree ring width, and a frequency based reconstruction method was applied to the historical documents. A new weighting method that was used to synthesize the two field reconstructions, which yields quantitatively improved validation skill compared with each individual field reconstruction.

The quality and fidelity of the Reconstructed Asian summer Precipitation (RAP) data have been extensively verified against the independent modern instrumental data over entire Asia (1901-1920) and against the long-term rain gauge observations over India (1813-1920) and Seoul (1771-1920). The results show skillful reconstruction in East and North China, Indochina peninsula, Maritime Continent (MC), northern India and Pakistan, mid-latitude Asia, and southern Japan. The RAP is best to illustrate large-scale rainfall variability with more uncertainties in representing small-scale or local rainfall anomalies.

The RAP reproduces realistic 20^{th} century precipitation climatology. Four area-averaged precipitation indices were constructed for (a) entire Asia, (b) monsoon Asia, (c) arid (central and western) Asia, and (d) MC. The interannual variations of the four indices show good agreement with observations during the 20^{th} century, indicating the ability of the RAP to capture large-scale year-to-year rainfall variability. For the pre-instrumental period, general agreements are found between the RAP and other proxies such as speleothem $\delta^{18}O$ records in China and India, and ice cores over the Himalaya and Tibetan plateau on the decadal time scale. It also captures the remarkably abrupt change during 1600s recorded in the upwelling proxy record over the Arabian Sea. While the results indicate that the RAP is to certain degree reliable for long-term variability estimation, its accuracy is limited by regional differences, observational coverage both in time and space, and precipitation regimes.

The 544-year long record of RAP reveals four major modes of variability. The first EOF mode features a unified drying over most parts of the AM system, and it is identified as

forced by a rapidly developing El Nino or transition from a cold to a warm phase of the biennial ENSO mode. The second EOF is an interdecadal mode with wet conditions over the YRV and South China, and dry conditions over India and northeast Asia. The third EOF shows a tripole pattern over the East Asia, and it is identified as related to a CP El Niño-like decadal mode in the Pacific. The fourth EOF features Indian and Southeast Asian dryness and a quadrupole pattern over the East Asia. It is identified as associated with the low-frequency ENSO mode.

The results show that the RAP is able to describe long-term variability modes of the Asian summer precipitation. It provides a valuable dataset for study of the large-scale Asian summer precipitation variability, especially on the decadal to centennial timescales, to aid our understanding on the attribution of these low-frequency processes.

Citation: Shi, H., B. Wang, E. R. Cook, J. Liu, and F. Liu, 2018: Asian summer precipitation over the past 544 years reconstructed by merging tree rings and historical documentary records. *J. Clim.*, **31**, 7845–7861, doi:10.1175/JCLI-D-18-0003.1.

Dataset: The Reconstructed Asian summer Precipitation (RAP) has been archived in the NOAA World Data Service for Paleoclimatology archive at https://www.ncdc.noaa.gov/paleo/study/24391.

Chapter 3. How does the Asian summer precipitation-ENSO relationship change over the past 544 years?

3.1. Abstract

The secular change of the Asian monsoon (AM)-El Niño-Southern Oscillation (ENSO) relationship has been recognized as a specter for seasonal forecast. The causes of such changes have not been well understood. How the monsoon-ENSO relationship underwent secular changes beyond instrumental period has rarely been discussed. Here I explore the multidecadal to centennial changes of the AM-ENSO relationship with the recently compiled Reconstructed Asian summer Precipitation (RAP) dataset (1470-2013) and multiple ENSO proxy indices. During the past five centuries, two leading modes of interannual variability of RAP are found to be associated with the ENSO developing and decaying phases, respectively. The mechanisms behind the modern monsoon-ENSO relationship can reasonably well explain the past monsoon behavior. In response to a developing ENSO, precipitation anomalies from the Maritime Continent (MC) via India to northern China are in phase, and this "chain reaction" tends to be largely steady since around 1620 AD when the Indian summer monsoon abruptly strengthened. Further, the strengthening of the link between developing-ENSO and Indian-northern China rainfall since 1620 AD concurred with a phase reversal of the Pacific Decadal Oscillation. During the decaying phase, however, the summer rainfall-ENSO relationship over the Yangtze River Valley-southern East China (YRV-SEC), the MC and central Asia, has gone through large multidecadal to centennial changes over the past five centuries. A remarkable reversal of sign in the AM-decaying ENSO relationship occurred roughly from 1740 to 1760 over the YRV-SEC and MC, which may be associated with the long-term strengthening of ENSO intensity. Future research should continue focusing on revealing the possible causes of the low-frequency changes in the

monsoon-ENSO relationship using general circulation models and paleoclimate proxy reconstructions.

3.2. Introduction

The Asian monsoon (AM) system has been extensively studied owing to its great significance and dynamical complexity (Wang 2006b). On the interannual timescale, the seasonal evolution of ENSO is a major pace-maker of the AM variability (e.g., Rasmusson and Carpenter 1983; Ropelewski and Halpert 1987; Webster and Yang 1992; Wang et al. 2003, 2015). During the El Niño developing phase, the Indian summer monsoon (ISM) tends to weaken (e.g., Walker and Bliss 1932; Shukla and Mooley 1987; Webster et al. 1998; Sikka 1980; Keshavamurty 1982; Mooley and Parthasarathy 1984) due to the suppressed convection over the Maritime Continent (MC) caused by the eastward shift of the Walker circulation (e.g., Palmer et al. 1992; Lau and Nath 2000); meanwhile the northern East Asian summer monsoon (EASM) also tends to weaken in phase with the ISM (e.g., Yatagai and Yasunari 1995; Kripalani and Kulkarni 2001; Enomoto et al. 2003). During the decaying phase of an El Niño event, the subtropical EASM and the Meiyu/Baiu frontal rainfall tend to enhance (e.g., Fu and Teng 1988; Huang and Wu 1989; Zhang et al. 1996; Lau and Sheu 1988; Chang et al. 2001) through the variation of the western North Pacific (WNP) subtropical high and its interaction with underlying Indo-Pacific warm pool (Wang et al. 2000a, 2013b). For a more detailed review of the East Asian monsoon, readers are referred to Wang and Li (2004). If one does not distinguish between the developing and decaying phase of El Niño (La Niña), the simultaneous correlation between summer rainfall in East Asia and the SST anomalies in the eastern equatorial Pacific would not be significant during instrumental period (Chen et al. 1992).

In a longer time frame, historical megadroughts and monsoon failures in Asia are found associated with strong El Niño events (Cook et al. 2010a; Feng et al. 2013). The footprint of ENSO is also found embedded in drought reconstructions over Asia (Li et al. 2014) and warm season precipitation reconstructions over China for the past 500 years (Shi et al. 2017b). These studies indicate that ENSO played an important role in the past AM

variability. However, the ENSO phase-dependent features of the Asian precipitation anomalies have not been fully addressed with proxy data. Although one of these studies (Li et al. 2014) distinguishes between the monsoon responses to ENSO developing and decaying phases, the results are limited to the South Asia and MC sectors. No evident signal is found in the EASM, likely due to the limitation of the Monsoon Asia Drought Atlas (MADA, e.g., Yang et al. 2013, 2014) used in the study.

The AM-ENSO relationships are tantalizing due to the effects of local air-sea interaction, land surface anomalies, as well as impacts of one monsoon subsystem on another. For example, the atmosphere-ocean interaction generates the Indian Ocean Dipole (IOD) mode, which affects the ISM variability (Saji et al. 1999; Webster et al. 1999; Li et al. 2003; Wang et al. 2003; Ashok et al. 2004, 2001). The local cloud-radiation-SST feedback over the northern Indian Ocean also affects the ISM and tends to offset the ENSO impacts (Lau and Nath 2000). The Himalayan/Eurasian snow cover has been identified as an important remote forcing of the AM besides the ENSO (e.g., Blanford 1884; Hahn and Shukla 1976; Barnett et al. 1989; Yang 1996). Within the AM system, the anomalous ISM convection also impacts the northern EASM variability (Wu and Wang 2002). Whether these impacts on the past AM-ENSO relationships have been recorded with paleoclimate proxies is unknown.

What is more complicated is that the AM-ENSO relationship is nonstationary. Since the late 1970s, the ISM-ENSO relationship has been observed to have weakened or broken down (e.g., Kumar et al. 1999), accompanied by a reversed relationship between the northern EASM and ENSO during the decaying El Niño phrases around the same time (Wu and Wang 2002). On the other hand, Wang et al. (2008) showed that the relationships between ENSO and the western North Pacific, East Asian, and Indonesian monsoons have all become enhanced during ENSO's developing, mature, and decaying phases. Thus, the overall coupling between the Asian-Australian monsoon system and ENSO has been strengthened.

The non-stationarity of the Indian monsoon-ENSO relationship has been recognized as a specter for seasonal forecast (Webster et al. 1998). The recent weakening of the ISM-

ENSO relationship has been associated to various factors such as anthropogenic warming (e.g., Kumar et al. 1999; Ashrit et al. 2001), interdecadal variations (e.g., Chang et al. 2001; Feba et al. 2018; Krishnamurthy and Krishnamurthy 2014; Wang et al. 2008) and random weakening due to interference by other interannual phenomenon (e.g., Ashok et al. 2001; Ashok and Saji 2007). The answer is not yet clear. A potential better understanding of the cause(s) could be obtained with long records that cover more cycles of such interdecadal changes under different mean climate. However, how the monsoon-ENSO relationship underwent secular changes on the interdecadal-centennial timescale beyond instrumental period has rarely been discussed.

This study aims to use a new 544-year Reconstructed Asian summer Precipitation (RAP) dataset to investigate how the AM responds to ENSO evolution. One question I am trying to address is to what degree the proposed mechanisms for the current AM-ENSO relationship remain applicable to the past AM-ENSO relationship. I also attempt to detect how the AM-ENSO relationship has changed over the past five centuries and explore what caused these changes. Section 2 introduces the RAP dataset, and describes the observational data and other proxy records used, as well as methodology. Section 3 discusses the long-term leading modes of the AM interannual variability and their dynamical ties with ENSO phases. Section 4 presents the secular changes of the AM-ENSO relationship in the past 544 years, followed by discussion (Section 5) and conclusions (Section 6).

3.3. Data and methods

The RAP dataset is a 2-by-2 degree gridded 544-year (from AD 1470 to 2013) summer precipitation reconstruction generated by merging two complementary proxies including 453 tree ring width chronologies and 71 historical documentary records over the Asian land region (8.75°S to 55.25°N, 61.25°E to 143.25°E) (Shi et al. 2018). The RAP dataset shows significantly improved data quality compared with single-type proxy reconstructions, and skillful reconstruction is found over East and North China, northern India and Pakistan, the Indochina Peninsula, mid-latitude Asia, the MC, and southern Japan. The RAP dataset has also captures well the large-scale year-to-year rainfall

variability over monsoon Asia, arid central Asia, and entire Asia during the 20th century. Specifically, the RAP captures the abrupt strengthening of ISM in the 1600s recorded by other proxies (Anderson et al. 2002; Sinha et al. 2011); to a larger extent, it shows relatively weak ISM during the Little Ice Age (15th to 19th centuries, Bradley and Jones 1993) in comparison with that during the industrial period as shown from other studies (Sinha et al. 2007; Tejavath et al. 2017).

To examine the long-term leading interannual variability modes of the Asian summer precipitation, I first applied an 8-year high-pass filter to the detrended data. The rotated empirical orthogonal function (REOF) analysis is used because it tends to yield more regionally confined patterns and is thus more appropriate for the purpose of studying the regional monsoon-ENSO relationships. A correlation-based K-mean cluster analysis (Seber 1984; Spath 1985) was also conducted to illustrate the regionality of the RAP. Global sea surface temperature (SST) from the Hadley Center Sea Ice and Sea Surface Temperature dataset (HadISST, Rayner 2003) within a period from 1870 to 2013 was used to examine the dynamic origins of the leading principal components (PCs).

To extend the monsoon-ENSO relationship back to the pre-instrumental period, I utilized ten conventional reconstructions of boreal winter ENSO indices for the past millennium, among which seven indices are developed from one or multiple types of proxies (e.g., tree rings, coral, ice core, and sediment) with global coverage (Stahle et al. 1998; Mann et al. 2000; McGregor et al. 2010; Wilson et al. 2010; Li et al. 2011, 2013; Emile-Geay et al. 2013) and three are derived solely from the tree rings in southwest North America (D'Arrigo et al. 2005; Cook et al. 2008; Braganza et al. 2009).

To evaluate the quality of the reconstructed Niño indices, the observed Niño 3.4 index from the HadISST dataset (Rayner 2003), and the Global Precipitation Climatology Centre (GPCC) monthly precipitation dataset from 1901 to present (Schneider et al. 2015) were used. Pattern correlation coefficients (PCCs) and normalized root mean square errors (NRMSEs) between the observed and reconstructed rainfall-ENSO relationship were calculated so as to determine the "best estimates" of the past ENSO variability.

Selected Niño proxies were used to further demonstrate the long-term AM-ENSO relationship. Each AM subsystem was represented by an area-weighted averaging index over the corresponding region. Rolling correlations with 11-year and 51-year windows between monsoon and Niño indices were examined and discussed both individually and collaboratively.

3.4. Long-term leading modes of high-frequency RAP (1470-2013)

3.4.1. Rotated EOF modes

The Asian summer monsoon rainfall variability has been studied primarily on regional scales, such as in India, East Asia, the WNP and the MC (e.g., Kumar et al. 1999; Ding and Chan 2005; Wang et al. 2000; Chang 2004). Lau and Wu (2001) studied the rainfall-SST co-variability for a short period of 1979–1998 using singular value decomposition (SVD) analysis of the Asian summer monsoon rainfall and global SST anomaly (SSTA). They found that the first mode is a biennial mode and the second one is associated with La Niña development. Using REOF analysis, here I adopt long records to identify the major modes of Asian precipitation variability.

The first REOF mode displays coherent changes over India and the Yellow River Basin (Figure 3.1a). It explains 12.2% of the total variance. Such a coherence of Indian and northern China variability has been observed with instrumental data (e.g., Yatagai and Yasunari 1995; Kripalani and Kulkarni 2001; Wu and Wang 2002) and speleothem records for past millennia on the annual, decadal (Berkelhammer et al. 2010) and longer timescales (Kathayat et al. 2016). It should also be noted that Indonesian precipitation is in phase with Indian and northern China precipitation anomalies, which is a typical pattern during the El Niño/La Niña developing stage. The second REOF mode has a strong loading over the Yangtze River Valley (YRV) where the major subtropical frontal zone is located, while the loadings of the opposite sign are over northwest India and Pakistan, and northeast Asia (Figure 3.1b). It explains 11.0% of the total variance.

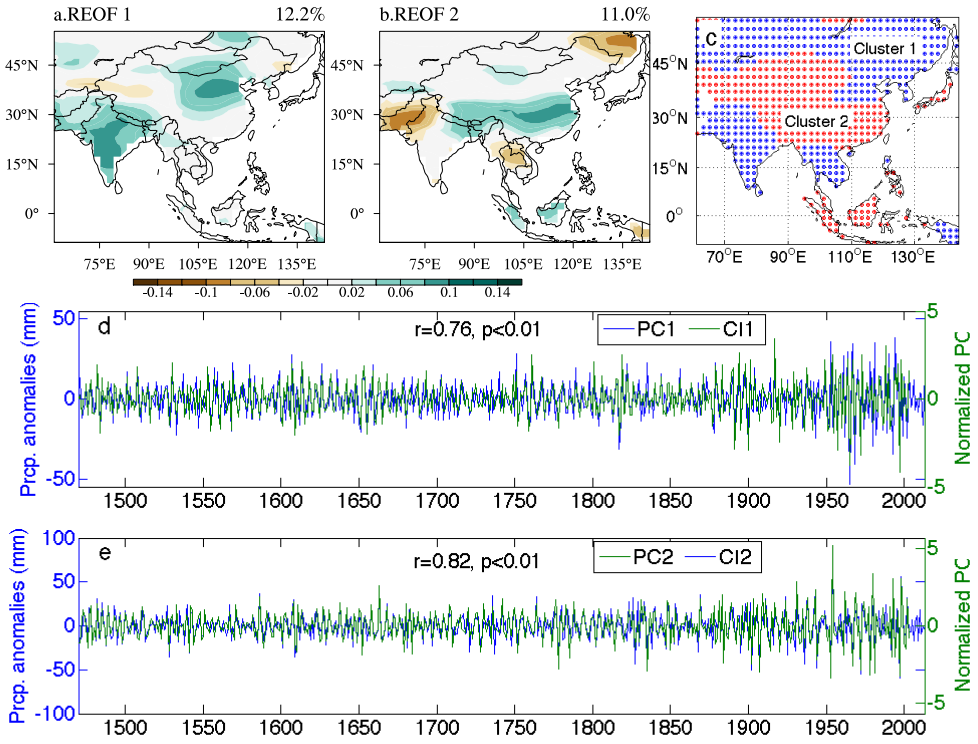

Figure 3.1 The spatial patterns of the first two leading interannual REOFs (a and b) and the two clusters (c), as well as their corresponding temporal coefficients PC1/CI1 (d) and PC2/CI2 (e) derived from the RAP for the period from 1470 to 2013.

The two leading REOF modes are in a general agreement with the results of the cluster analysis (Figure 3.1c). Cluster 1 in the blue color corresponds to the large loading areas in the first REOF mode, including north Asia, India, and the Yellow River Basin in northeastern China. Cluster 2 in red corresponds to the large loading areas of the second REOF mode, including western China, southern East China, and southern Japan. I define the area-weighted averages of precipitation anomalies in the blue and red regions as Cluster Index 1 (CI1) and Cluster Index 2 (CI2), respectively. CI1 and CI2 are significantly correlated with REOF1 and REOF2, respectively. The corresponding correlation coefficient is r=0.76 ($p<0.01$) and r=0.82 ($p<0.01$), respectively (Figure 3.1d, e).

3.4.2. Origin of the two leading modes

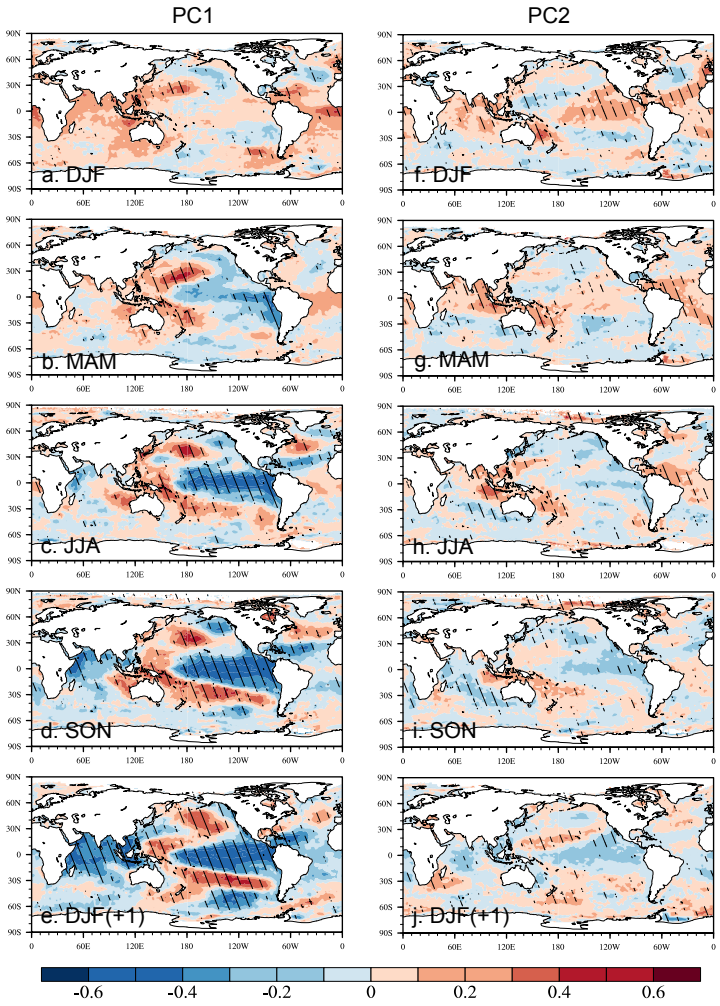

Figure 3.2 Spatial patterns of correlations with global SSTs for PC1 (a-e) and PC2 (f-j) from 1870 to 2013. Hatched areas are significant correlations at the 90% level and higher (2-tailed).

The linkages of the PCs with global SSTs are examined to understand their origins. The data cover the period of 1870-2013 when global SSTs are available. As shown in Figure 3.2, the increased precipitation shown in REOF1 corresponds to a developing La Niña in the Pacific (Figure 3.2a-e). Significant negative SST anomalies first appear over the cold tongue region in the preceding spring (March-April-May, Figure 3.2b). The negative SSTs become stronger during summer (Figure 3.2c) and maintain through the following fall (Figure 3.2d) and winter (Figure 3.2e). The results indicate that the increased rainfall over northern Asia, India, and the Yellow River Basin in northern China is associated

with the development and maintenance of a La Niña-like condition. The power spectrum of PC1 has a pronounced 5-year peak that passes the 95% significance level, indicating its association with the low-frequency component of ENSO (Figure 3.3a), which is reflected by the relatively slow development of La Niña (Figure 3.2a-e).

The SST anomalies associated with PC2 suggest that REOF2 may be more closely associated with the El Niño decaying phase or a transition from warm to cold ocean conditions (Figure 3.2f-j). An El Niño condition exists in the preceding winter (Figure 3.2f). The anomalous warming disappears during the spring (Figure 3.2g) and a La Niña-like SST pattern starts to develop from the summer to the following winter (Figure 3.2h-j), suggesting a rapid transition from warm to cold ocean conditions, which is a feature of quasi-biennial fluctuation. Spectral analysis confirms that strongest significant peaks of the PC2 range from 2.2 to 2.8 years (Figure 3.3b), thus reflecting its association with the biennial component of ENSO (Figure 3.2f-j).

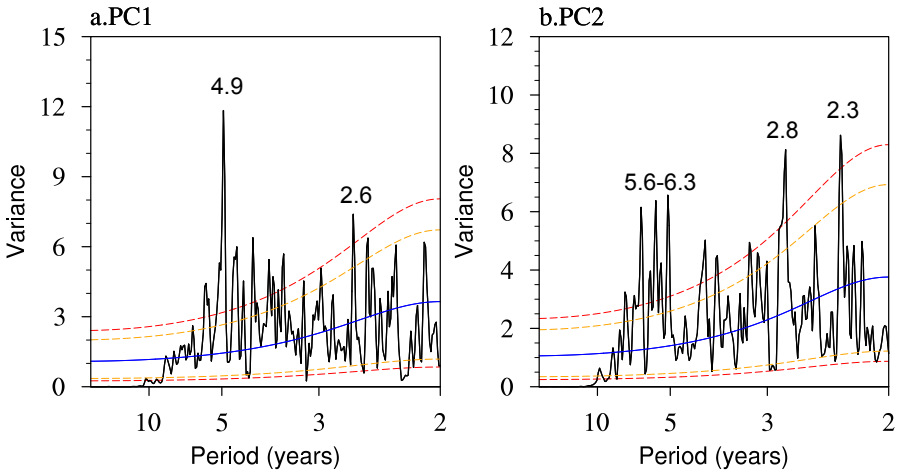

Figure 3.3 Power spectra for PCs derived by using forward fast Fourier transformation, with 10% of the data tapered, and the modified Daniell window with a span of 4. Blue lines are the Markov Red Noise spectra. Red and orange dash lines indicate upper (lower) confidence bounds at 95% and 90% significance levels, respectively.

The two major modes of variability identified here are consistent with the results of the EOF analysis of the Asian monsoon rainfall during the recent period of 1979-2010 made by Wang et al. (2015), who identified four major modes of variability. The first mode is

an El Niño-La Niña developing mode, and the second one is an ENSO decaying mode, which is an Indo-western Pacific monsoon-ocean coupled mode. The agreement in the resultant two leading modes between our REOF and cluster analyses of the RAP and the EOF analysis of Wang et al. (2015) lends confidence for the RAP analysis and suggests that the two leading modes are robust in both recent decades and the last 544 years.

3.4.3. Relationship between the leading patterns and Niño indices during 1870-2010

Before study of the ENSO relationship with the leading modes derived from the RAP for the entire 544-year period, I first assess their relations during the instrumental period from 1870 to 2010 when the Niño proxies are more reliable.

Table 3.1 Correlation coefficients between REOF PC1 (PC2) and Niño 0 (1) indices for the period of 1870 to 2010. Numbers in italic indicate insignificant correlations. 0 and 1 denote ENSO develop and decay cases, respectively.

		REOF PC1	PC2
Instrumental	Rayner et al., 2003	-0.42 (p<0.01)	*0.13*
Global proxy	Emile-Geay et al. 2013	-0.32 (p<0.01)	*0.07*
	Li et al. 2013	-0.38 (p<0.01)	*0.08*
	Braganza et al. 2009	*-0.09*	*0.02*
	Wilson et al. 2010	-0.32 (p<0.01)	*0.09*
	McGregor et al. 2010	-0.26 (p<0.01)	*0.10*
	Mann et al. 2000	-0.26 (p<0.01)	*0.09*
	Stahle et al. 1998	-0.27 (p<0.01)	*0.08*
NA Tree ring	Li et al. 2011	-0.19 (p<0.05)	*0.14*
	Cook et al. 2008	-0.30 (p<0.01)	*0.12*
	D'Arrigo et al. 2005	-0.31 (p<0.01)	*0.09*

Table 3.1 shows that correlations between PC1 and Niño (0) are relatively high and largely significant at the 1% confidence level, whereas correlations between PC2 and Niño (1) are insignificant. Here 0 denotes the ENSO developing year and 1 denotes the ENSO decaying year with respect to JJA rainfall, since ENSO tends to peak toward the end of the calendar year (0). The above result indicates that the relationship between the developing ENSO and summer (JJA) precipitation over the MC, India and northern China (REOF1) is robust. However, during the decaying phase of ENSO, the summer precipitation over the YRV (REOF2) is more variable and overall insignificant in response to the eastern Pacific SST anomalies.

The two types (global proxy- and North America (NA) tree ring-based) indices show largely equal strength in their relations with the RAP, except that Braganza et al. (2009) and Li et al. (2011) show lower correlations (Table 3.1). Previous studies have shown a significant relationship between the tree ring width chronologies in NA and in Asia on the interdecadal and longer timescales (Fang et al. 2015; Li et al. 2013). One concern is that the correlations here between the RAP and the NA tree ring-based Niño indices could be largely due to the trees. I cannot completely rule out this possibility since the RAP is partially derived from the tree ring width chronologies in Asia, but the fact that the global proxy-based indices show similar correlations indicates that such relation is likely a true signal between precipitation and ENSO reflected by indices from various proxy types. Among the global-proxy based reconstructions, Li et al. (2013) uses the first two PCs from the MADA (Cook et al. 2010a), which share many tree ring chronologies with the RAP over central Asia and the MC (Li et al. 2014). I decided to retain Li et al. (2013) reconstruction, however, because (1) it shows good quality compared with observed DJF Niño index ($r=0.75$, $p<0.01$); and (2) it is largely independent with the RAP in regions other than central Asia and the MC. Besides, sensitivity testing shows that excluding Li et al. (2013) Niño index would not change the conclusions.

Figure 3.4 and Figure 3.5 show the spatial patterns of correlations between Niño indices and rainfall during the ENSO developing and decaying phases, respectively. During the ENSO developing phase (Figure 3.4), the observed Niño-monsoon (May to Oct.) relationship largely resembles the pattern of RAP REOF1. Niño index reconstructed by Li et al. (2013) shows the highest PCC and lowest normalized RMSE, followed by that of Cook et al. (2008) and Emile-Geay et al. (2013). During the decaying phase (Figure 3.5), the PCCs are significantly lower. Niño index reconstructed by Cook et al. (2008) yields the best performance, followed by that of Li et al. (2013). Based on the above evaluations, I selected the top four, which are Niño reconstructions by Li et al. (2013), Emile-Geay et al. (2013), Cook et al. (2008) and D'Arrigo et al. (2005) to further analyze the long-term variability of the AM-ENSO relationship.

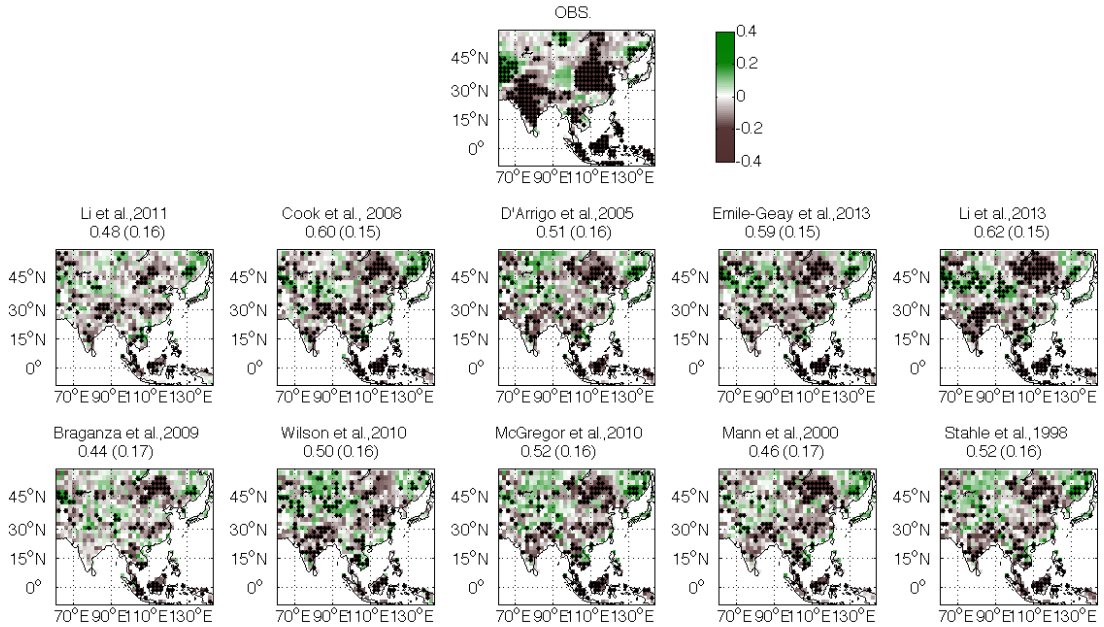

Figure 3.4 Spatial patterns of correlations between Niño indices and the RAP during ENSO developing years from 1901 to 2010 in comparison with observed correlation map. Dotted areas are significant correlations at the 90% level and higher (2-tailed). Numbers are PCCs and numbers in prentices are normalized RMSEs.

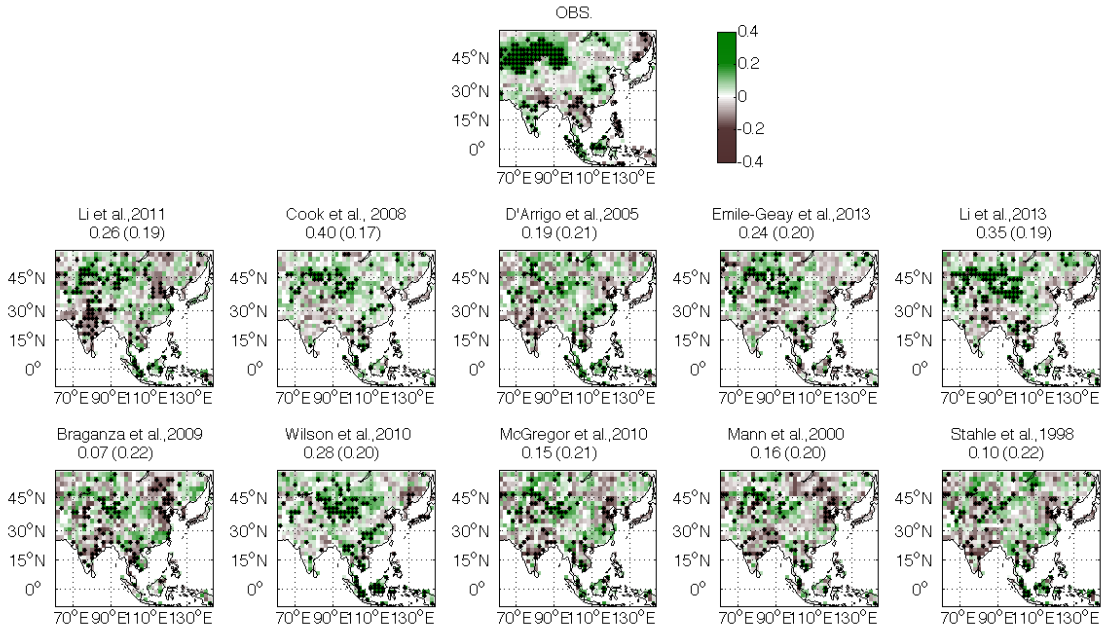

Figure 3.5 Same as Figure 3.4, except for the relationship between Niño indices and the RAP during the ENSO decaying years.

3.5. Secular changes of the AM-ENSO relationship in the past 544 years

In order to investigate the long-term relationship between the RAP and ENSO, I use the four proxy ENSO indices described in Section 3.3 and 3.4.

3.5.1. ENSO developing phase

Figure 3.6 shows the RAP response to developing El Niño events for the present (1901 to 2010, Figure 3.6b) and the past (1470 to 1900, Figure 3.6a). The pattern for the pre-1900 period largely resembles the one after 1900, especially for the key monsoon subsystems. Reduced rainfall is found over India, northern China and the MC, whereas enhanced rainfall occurs over central Asia. Differences also exist. For example, the positive correlations over the western China (35-45°E, 85-100°E) were negative before 1900; the negative correlations over southern China and along the Yangtze River after 1900 were nearly normal before 1900.

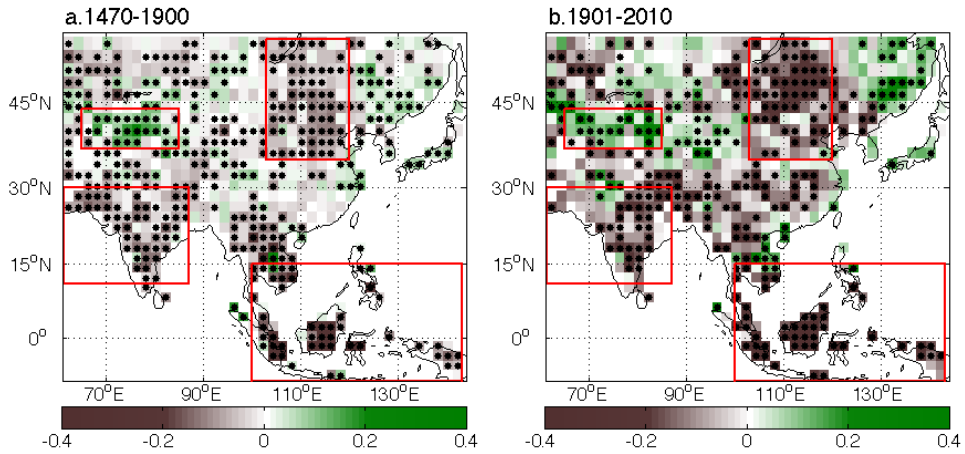

Figure 3.6 Relationship between Asian summer precipitation and developing ENSO events. Spatial patterns of correlations between Niño index and the RAP in ENSO developing Niño years for the periods of (a) 1470 to 1900 and (b) 1901 to 2010. Maps are averaged from four Niño reconstructions. Dotted areas are significant correlations at the 90% level and higher (2-tailed).

Four regions of significant correlations are identified, including the MC (9°S-15°N; 100-143°E), India (11-30°N, 61-87°E), northern China (35-55°N, 103-120°E), and northwestern China-central Asia (37-44°N, 65-85°E). Time evolutions of the summer precipitation-ENSO relationship over the four regions are shown in Figure 3.7. The

summer precipitation over the MC is significantly negatively correlated with the Niño indices except during the first half of the 19th century (Figure 3.7a), and the average of the 51-year rolling correlation for all four indices is -0.31. It's also noteworthy that the relationship is largely stable over time on multidecadal to centennial timescales (lines in Figure 3.7a). Slightly weakened correlations appear between 1740 and 1840. The relationship becomes strong after around 1860 to the end of the 20th century. On the interdecadal timescale (shading in Figure 3.7a), very few breaks of positive correlation occur around 1800, but they are not significant (Figure 3.7a). Meanwhile negative correlations dominate (overall r=-0.33), and significant negative correlations are more frequent.

The Indian rainfall-ENSO relationship (Figure 3.7b) is overall negative (r=-0.16). However, large fluctuations appear with periods of insignificant correlations and zero or slightly positive correlations on multidecadal to centennial timescales (lines in Figure 3.7b). On the interdecadal timescale (shading in Figure 3.7b), decades of positive correlations are found around 1520, 1570, 1730, and 1850, albeit insignificant. A similar case is found with respect to the northern China rainfall-ENSO relationship (Figure 3.7c). In fact, the correlations between the Indian rainfall-ENSO and northern China rainfall-ENSO relationships are as high as 0.72 on the interdecadal timescale, and 0.79 on multidecadal to centennial timescales, indicating coherent low-frequency changes over the two regions for the past 500 years. Periods with a strong ENSO tie are seen from around 1620 to 1700, and from around 1950 to 1990 for both India and northern China (Figure 3.7b, c), which coincide with the periods of strengthened MC rainfall-ENSO correlations (Figure 3.7a). It is noteworthy that the ENSO tie with the Indian and northern China rainfall seems to be strengthened since 1620, which nearly concurs with a well-documented abrupt strengthening of the Indian summer monsoon during the 1600s, as shown in an upwelling proxy (Anderson et al. 2002), speleothem records (Sinha et al. 2011) and the RAP (Shi et al. 2018). For the period of 1620-2010, the correlation coefficient between Indian monsoon rainfall and ENSO is -0.23 ($p<0.01$) and that between the northern China rainfall and ENSO is -0.19 ($p<0.01$).

The central Asia rainfall-ENSO relationship is largely positive on both interdecadal (r=0.21) and longer timescales (r=0.20) (Figure 3.7d). After 1620 AD, significant positive correlations often occur during the periods of strong negative AM-ENSO correlations (Figure 3.7 a-c), suggesting likely opposite phases between the AM-ENSO relationship and the arid central Asia-ENSO relationship.

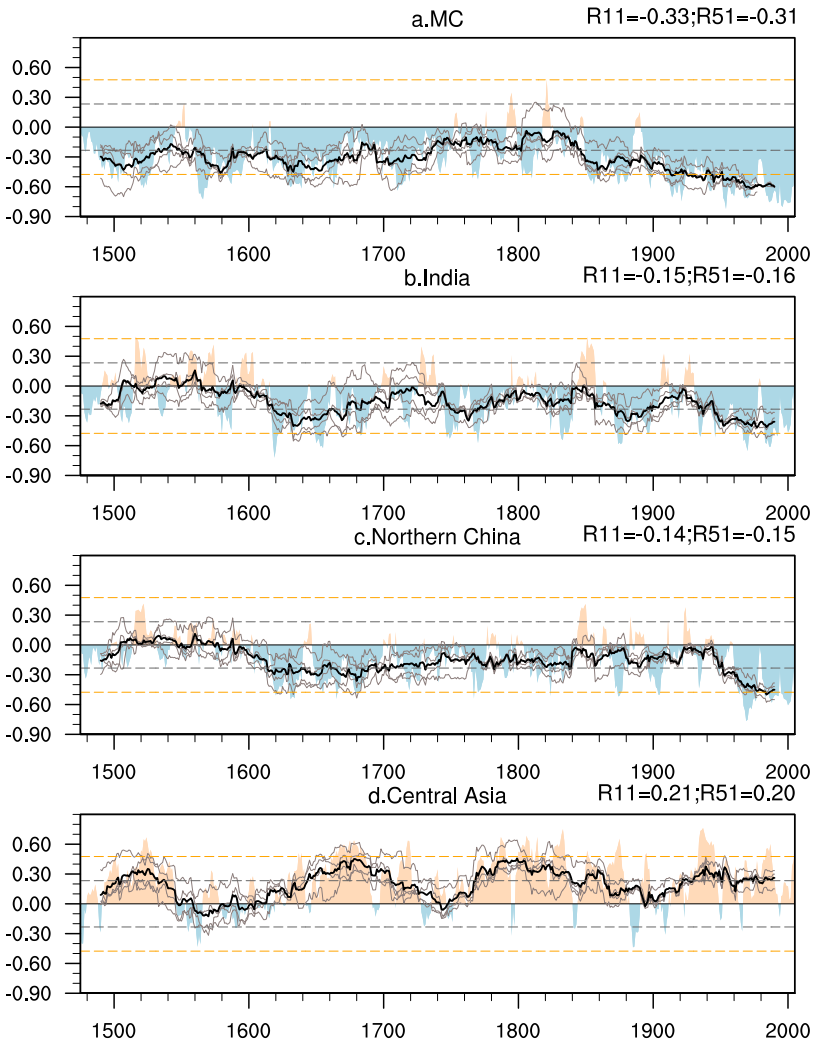

Figure 3.7 11-year (shadings) and 51-year (lines) rolling correlations between Niño indices and the rainfall indices in ENSO developing years. Shadings are averages of four Niño reconstructions. Gray Lines are individual Niño indices and black line is the average of them. Dotted lines are cutoff correlations at the 90% significance level with n-2 degree of freedom (orange lines: DOF=9, gray lines: DOF=49).

3.5.2. ENSO decaying phase

For the ENSO decaying phase, in a similar fashion, I show the rainfall-ENSO relationship before (Figure 3.8a) and after 1900 (Figure 3.8b). Apparent differences are found between the two. First, positive correlations are found over a large area of central Asia-northwestern China after 1900, but the relationship is more inhomogeneous before 1900. Second, significant negative correlations are found over India and northern China before 1900, but very few significant correlations exist after 1900. Third, positive correlations are located over the southeastern China before 1900, while after 1900 they are located over the YRV. Fourth, over the MC, the correlations are largely negative before 1900, while positive correlations prevail after 1900. These remarkable differences suggest that during ENSO decaying phases the Asian rainfall-ENSO relationship is highly variable over the past five centuries and what is seen today is not a robust long-term signal.

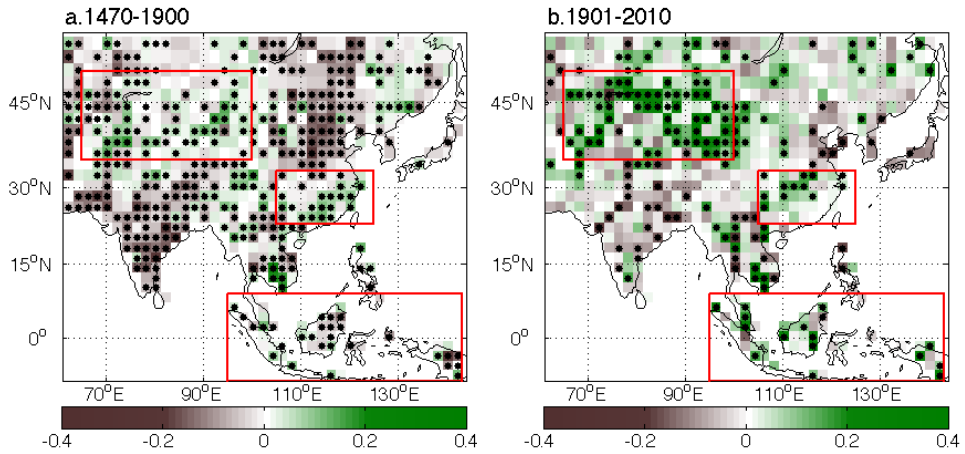

Figure 3.8 Relationship between Asian summer precipitation and decaying ENSO events. Same as Figure 3.6, except for the summer precipitation in ENSO decaying years.

To find out the changing points of decaying ENSO-AM rainfall relationship over the past 544 years, I take three regions of interest to examine the time evolution of the precipitation-ENSO relationship during the decaying phase of ENSO, which are the Yangtze River Valley-southeastern China (YRV-SEC, 23-33°N; 105-125°E), the MC (9°S-9°N; 95-143°E), and central Asia (35-50°N, 65-100°E).

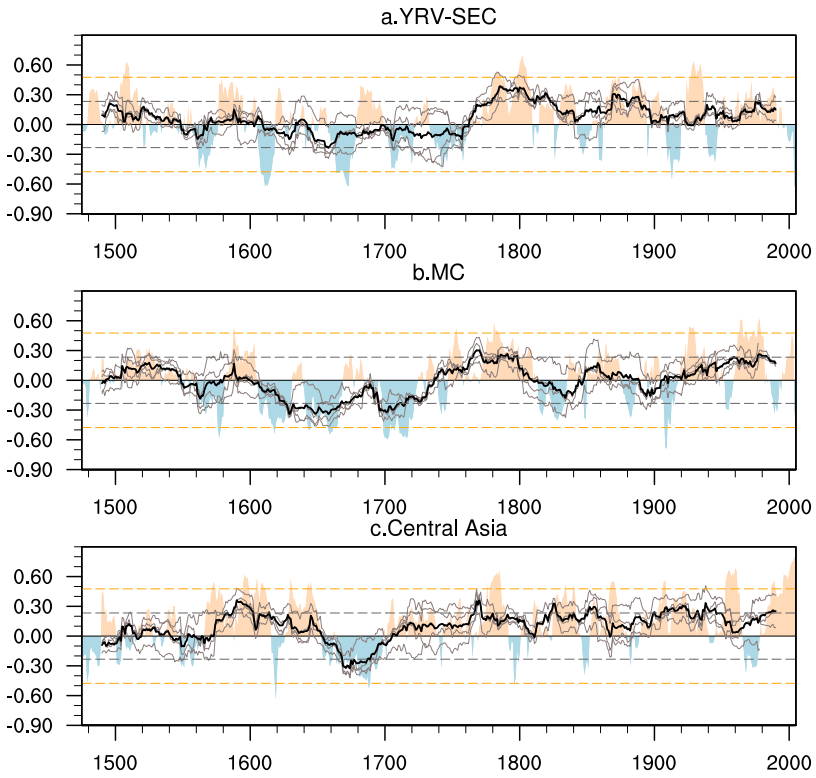

Figure 3.9 Same as Figure 3.7 except for the correlations between Niño indices and the rainfall indices in ENSO decaying years.

As shown in Figure 3.9, the relationship is nonstationary for all three regions indicated by the three indices on both interdecadal timescale (shading) and multidecadal to centennial (lines) timescales. The YRV-SEC rainfall-ENSO and MC rainfall-ENSO relationships seem to undergo similar low-frequency changes throughout the past 500 years (Figure 3.9a, b). The correlation between the two rainfall-ENSO relationships is 0.51 (0.39) on the centennial (interdecadal) timescale. A noticeable centennial shift from negative to positive relationship is found during 1740 to 1760 (lines in Figure 3.9a, b). After 1760, the YRV-SEC-ENSO relation is overall positive ($r=0.15$, $p<0.05$). Another centennial shift is found in the middle-late 16th century but less evident. These results suggest that during the ENSO decaying phase the relationship between ENSO and Asian summer monsoon rainfall over the YRV-SEC and MC is highly variable on the centennial time scale. The Central Asia rainfall-ENSO relationship (Figure 3.9c) is less coherent with those between ENSO and YRV-SEC and MC rainfall. After 1700, the correlation is largely positive ($r=0.20$, $p<0.01$); before 1700, the relation is more variable ($r=-0.02$,

insignificant). The mid-18th century change in the YRV-SEC (MC) rainfall-ENSO relationship is evident. The cause of such a sudden change deserves further investigation, probably through numerical experiments.

3.6. Discussion

3.6.1. Mechanisms of the monsoon-ENSO relationship: present and the past

Wang and Fan (1999) identified two major convective heat sources that drive the Asian summer monsoon system, thus distinguishing the ISM variability with the WNP-EASM variability. The former is impacted by the heat source centered in the Bay of Bengal-India-Arabian Sea region, and the latter is controlled by the convection center anchored in the South China Sea and the Philippine Sea. ENSO affects Asian summer monsoon through changing the two convective heat sources directly and indirectly (Wang et al. 2001).

During a La Niña developing stage, convection over the MC is enhanced under the direct response to the enhanced Walker circulation due to atmospheric equatorial wave adjustment. The enhanced precipitation heating then excites ascending Rossby waves to its west and north of the equator where the Bay of Bengal-India heat source locates, causing enhanced rainfall over India. Opposite anomalies occur during an El Niño episode. The coherent change of ISM and EASM in REOF1 reflects the impact of anomalous Indian convection on northeast EASM through a "Silk Road" zonal wave train pattern during boreal summer (Enomoto et al. 2003). This Silk Road wave train pattern is a part of the circumglobal teleconnection (CGT) (Ding and Wang 2005). A schematic diagram illustrating these processes can be found in Wang et al. (2017, Figure 9).

Ashok et al. (2004) show that when a positive IOD event simultaneously occurs with El Niño, the ENSO influence on ISM can be reduced by introducing an anomalous divergence center in the eastern tropical Indian Ocean. It is also shown that positive IOD events amplify the ENSO-induced dryness over the MC. Nevertheless, the ENSO influence seems to remain largely dominant and robust. Mooley and Munot (1993) have shown that the ISM is consistently negatively correlated with a developing ENSO from 1871 to 1990.

REOF2 (Figure 3.1a) represents strengthening of the subtropical EASM rain belt during a rapid decay of El Niño when the heat source over the Philippine Sea is suppressed due to enhanced WNP subtropical high (SH). The opposite is nearly true during the decay of strong La Niña events. During the decaying phase of a *strong* El Niño, the El Niño-induced WNP anticyclonic anomaly (WNPAC) can interact with underlying dipolar SST anomalies in the Indo-Pacific warm pool, thereby maintaining the WNPAC and leading to a prolonged Niño impact on East Asia (Wang et al. 2000a, 2013b). A *weak* El Niño, during its rapid transition to La Niña, may also enhance the post-El Niño summer rainfall over the Yangtze River Catchment, nevertheless through a different physical process: the WNPAC re-emerges as a forced response to the rapid cooling in the central-eastern Pacific (Wang et al. 2017a).

Wang et al. (2017) have shown that over the past 60 years, the only robust seasonal signal for EASM is the wet (dry) anomalies over central North China during the La Niña (El Niño) developing summer. The response of rainfall variability over the middle and lower reach of the YRV during the ENSO decaying summer largely depends on the ENSO intensity (Wang et al. 2017a). Besides, the migratory nature of the EA subtropical frontal zone and the associated rainfall variability on the subseasonal timescale also contributes to the relatively weak PC2-ENSO correlation (Table 3.1). The background mean state in tropical and North Pacific SSTs also plays a role in altering WNP convective anomaly (Wu and Wang 2002) and thus changing the EASM-ENSO relationship.

It seems that the afore-discussed mechanisms for the modern AM-ENSO relationship can, to a great extent, work for the past as well. During the ENSO developing phase, the ENSO induced chain reaction of precipitation anomalies over the MC and through India to northern China is shown by the overall coherent variations displayed in Figure 3.7a, b and c. The ENSO-rainfall relations over the MC and India are less coherent and largely non-linear, maybe reflecting the aforementioned IOD influences on the ISM. The in-phase and opposite-sign relationship over central arid Asia (Figure 3.7d) can be explained by the monsoon-desert coupling mechanism (Hoskins and Wang 2006), which attributes the drying to the interaction between the anomalous monsoon heating-induced circulation anomalies and the mean westerly flow. It is quite remarkable that despite of the large

uncertainties associated with proxy reconstructions, such a chain-reaction system is still discernable and sustained for almost five centuries. During the ENSO decaying phase, the large interdecadal to centennial variations over the past 500 years (Figure 3.9) echo the highly variable EASM-decaying ENSO relationship in the present. Such a relationship is proved to be rather fragile and nonstationary over time.

3.6.2. Possible reasons for the multidecadal to centennial changes of the monsoon-ENSO relationship

It is a great challenge to fully explain the causes of secular (interdecadal-centennial) changes in the RAP-ENSO relationship shown in Figure 3.7 and Figure 3.9, because (1) the fitted reconstruction data are insufficient and different proxies usually have large discrepancies, and (2) models have limited skills in simulating interdecadal-centennial variations. Here I further examine the Pacific Decadal Oscillation (PDO) and long-term changes in ENSO intensity as an effort to detect possible factors that may contribute to low-frequency variations of the monsoon-ENSO relationship. The external effective radiative forcing is not examined because it is not independent from the ENSO intensity on this timescale ($r=0.62$, $p<0.01$).

Figure 3.10a shows normalized PDO induces derived from five groups and their ensemble mean. Note the considerable spread among the five proxy PDO indices. Nevertheless, similar evolutions between the PDO and the ISM-developing ENSO relationship (Fig. 7b) as well as the EASM-developing ENSO relationship (Fig. 7c) are notable. The correlation between the ISM-ENSO (EASM-ENSO) relation and 51-year smoothed PDO ensemble is 0.64 (0.77, $p<0.01$). In particular, the strengthening ISM-ENSO relation at 1620 coincides a phase reversal of the PDO. The weakened EASM-ENSO relation from 1900 to 1940 is also accompanied by a period of positive PDO.

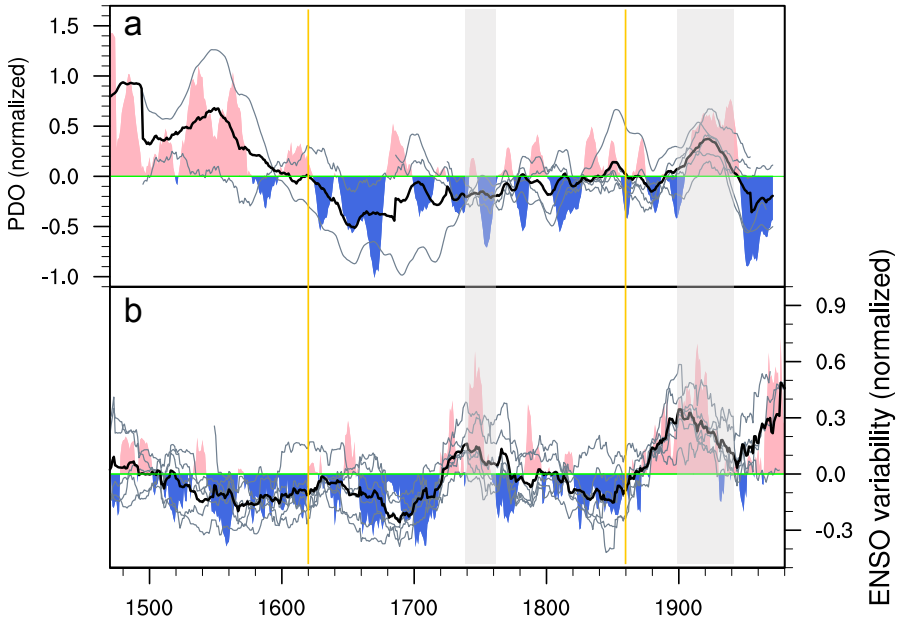

Figure 3.10 11-year (shadings) and 51-year smoothed normalized PDO indices (a) and ENSO amplitude variability (b). Black lines are ensemble means. Five PDO indices include D'Arrigo et al. (2001, 1700 and 1790 reconstructions), MacDonald and Case (2005), Shen et al. (2006), and Biondi et al. (2001). Six Niño indices include D'Arrigo et al. (2005), Cook et al. (2008), Braganza et al. (2009), Li et al. (2011; 2013), Emile-Geay et al. (2013). Gray bars mark the characteristic periods of 1740 to 1760, and 1900 to 1940; yellow lines mark the characteristic years 1620 and 1860.

The ENSO intensity (Figure 3.10b) seems to be linked to the MC rainfall-developing ENSO relation (Figure 3.7a). After around 1860, strengthened ENSO corresponds to strengthened monsoon-ENSO tie over the MC (Figure 3.7a). The correlation between MC rainfall-ENSO relation and the ENSO intensity is -0.43 ($p<0.05$) on the multidecadal to centennial scale. For the AM rainfall-decaying ENSO relationship (Figure 3.9), it seems that its centennial change may be more related to the centennial variations of the ENSO intensity (Figure 3.10b). The correlations of 51-year smoothed ENSO intensity are 0.25 ($p<0.20$) with the YRV-SEC rainfall-ENSO relation, 0.40 ($p<0.10$) with both those of the MC rainfall and Central Asian rainfall. The largely strengthened ENSO amplitude since 1720 (Figure 3.10b) could cause the dramatic sign-changes in monsoon-ENSO relationship around 1740 and 1760 over the MC (Figure 3.9b) and YRV-SEC (Figure 3.9a) regions.

Due to the limited quality of the proxy data, the causes of the secular change of the AM-ENSO relationship discussed above remain to be confirmed. The causality between PDO and ENSO-AM relationship remains elusive. It is likely that the centennial variations of the ENSO intensity are more important in modulating the monsoon-ENSO relations during the decaying phase of an El Niño.

3.7. Conclusions

The RAP records phase-dependent influences of the ENSO on Asian summer precipitation since 1470. Two major modes of interannual variability are identified. The first mode features coherent variations over the MC, India and northern China, and this "chain reaction" is associated with the developing phase of the low-frequency (5-year) component of ENSO. The second mode shows variation centers over the YRV, which is associated with the decaying phase of ENSO and/or the rapid transition of the biennial component of ENSO. Mechanisms for the modern monsoon-ENSO relationship can be extended back in time, and still provide reasonable explanations for the past monsoon behavior before the instrumental period.

During the ENSO developing phase, the AM-ENSO relationship is relatively stable albeit periods of breaks occasionally take place on the interdecadal timescale. The MC-India-northern China chain-reaction in response to ENSO tends to be largely steady since around 1620. Meanwhile, the MC rainfall-ENSO relation is more robust than the ISM-ENSO relation, likely due to the counter-impact of the IOD on the ISM. Of interest is that the ENSO tie with the Indian and northern China rainfall tends to be strengthened in the early 1600s, concurring with the abrupt strengthening of the Indian summer monsoon.

During the ENSO decaying phase, the rainfall-ENSO relationship has gone through large interdecadal to centennial changes over the YRV-SEC, the MC and the central Asia for the past five centuries. An evident sign reversal in the rainfall-ENSO relationship over the YRV-SEC and the MC occurred from 1740 to 1760, which is suggested by various Niño proxies and their ensemble.

It remains a great challenge to understand the causes of the secular (interdecadal-centennial) changes in the Asian summer monsoon (ASM)-ENSO relationship. Nevertheless, evidence presented shows that the Pacific Decadal Oscillation is linked to multidecadal to centennial change of ASM-ENSO relationship (Figure 3.10a), especially for the ISM and EASM during the ENSO developing phase (Figure 3.7b,c). The strengthening ISM-ENSO relation at 1620 coincides with a phase reversal of PDO (Figure 3.10a); the weak EASM-ENSO relation from 1900 to 1940 also concurs with a positive phase of PDO (Figure 3.10a). During the ENSO decaying phase (Figure 3.9), on the other hand, the centennial reversal of sign of the YRV-SEC (MC) rainfall-ENSO relation from 1740 to 1760 seems to follow an overall strengthening of ENSO intensity since 1720 (Figure 3.10b).

The present results are made based on the ensembles of various proxy reconstructions with considerable spreads. While it does not clarify the reasons for the secular change of the complicated AM-ENSO relationship, it provides a reasonably comprehensive documentation of the interdecadal through centennial changes of the ENSO association with various Asian monsoon components. While one should not overlook the effects of external forcing such as solar-volcanic and greenhouse gases, fluctuations of the ASM-ENSO relationship on the multidecadal to centennial scale are likely dominated by internal processes within the coupled climate system. However, concrete conclusions can only be drawn after further testing with plausible numerical simulations. Future research should continue focusing on discovering possible causes of the low-frequency changes in the monsoon-ENSO relationship using general circulation models and paleoclimate proxy reconstructions.

Citation: Shi, H., and B. Wang, 2018: How does the Asian summer precipitation-ENSO relationship change over the past 544 years? *Clim. Dyn.*, **doi:10.1007/s00382-018-4392-z. http://link.springer.com/10.1007/s00382-018-4392-z**

Chapter 4. Proxy evidence of decadal to centennial variations of Asian summer precipitation since 1470

4.1. Abstract

Aspiring features of decadal, multidecadal and centennial variations of the Asian summer precipitation are revealed by analysis of the new Reconstructed Asian summer Precipitation (RAP) dataset from 1470 to 2013. Significant low-frequency periodicities of the All Asian Rainfall (AAR) index are found on decadal (8-10 years), quasi-bidecadal (22 years), and multidecadal (50-54 years), as well as centennial time scales. The decadal and multidecadal peaks are mainly from the monsoon Asia and Maritime Continent, while the 22-year peak is from the arid Asia. A remarkable abrupt shift of leading frequency from multidecadal to decadal is detected around AD 1700 across the entire Asian land, which nearly concurs with a dramatic upswing of the AAR. The leading EOF modes on the decadal, multidecadal and centennial time scales all exhibit a similar spatially uniform structure, suggesting a cross-time scale, in-phase variation of the rainfall across the continental Asia. The leading decadal mode shows that an enhanced AAR is associated with a mega-La Niña, a warm extratropical North Atlantic and cool tropical South Atlantic. The leading multidecadal mode is significantly correlated with the reconstructed Atlantic Multidecadal Oscillation (AMO) index as well as the proxy mega-ENSO index. Centennial variation of the AAR follows more closely the volcanic forcing variation, while is uncorrelated with solar forcing variability. Note that both the AAR-mega-ENSO and AAR-AMO relationships are nonstationary and experienced significant secular changes, especially around AD 1700; so is the AAR-volcanic forcing relation. Comparison with previous results and the uncertainties involved are discussed in detail.

4.2. Introduction

The Asian monsoon and global monsoon vary across timescales (Wang 2006a; Wang et al. 2014, 2017c). The recent half century has witnessed significant interdecadal changes of the East Asian summer monsoon (EASM) in the late 1970s and the early 1990s (1992-94) in terms of precipitation pattern (Ding et al. 2008, 2009; Zhou et al. 2009; Kwon et al. 2007; Yim et al. 2014). Interdecadal shift of the India summer monsoon (ISM) from above normal and below normal was observed around 1970 (Goswami 2006), followed by decrease of potential predictability in the mid- to late- 1970s (Goswami 2004). Since the late 1970s, the inverse relationship between the ISM rainfall and Niño-3.4 SST anomalies had broken down (e.g., Kumar et al. 1999). Concomitantly, a notable change between the EASM and ENSO in northern China and Japan has emerged (Wu and Wang 2002), and the negative correlation between Indonesian monsoon rainfall and ENSO has become enhanced (Chang et al. 2004). Wang et al. (2008) showed that since the late 1970s the relationships between ENSO and the western North Pacific, East Asian, and Indonesian monsoons have all become enhanced during ENSO's developing, mature, and decaying phases, overriding the weakening of the Indian monsoon–ENSO anticorrelation during the developing phase. The strengthening of overall coupling between the Asian-Australian Monsoon (A–AM) system and ENSO was attributed mainly to the amplification of ENSO amplitude. However, the instrumental data is too short for a robust analysis of the multidecadal to centennial variability of the monsoon.

Several studies have analyzed proxy monsoon records spanning the past millennium or two, most of which focus on the ISM (Zhu and Wang 2002; Sinha et al. 2011, 2015; Sankar et al. 2016; Shi et al. 2017a; Goswami et al. 2016). Since the decadal to centennial variations and responses to external forcing often occur beyond regional scales, it is more proper to look at larger spatial scale rainfall reconstructions for detecting coherent changes of the EASM and ISM, as well as adjacent regions in Asia. This has not been done.

Among the major challenges to understand decadal to multidecadal climate variability are to distinguish whether such changes arise from internal coupled dynamic modes or are

driven by forcings external to the coupled climate system, as well as to determine their relative contributions. In the groundbreaking work of Wang et al. (2013), the decadal variations of the Northern Hemisphere (NH) summer monsoon rainfall are largely attributed to internal coupled dynamics even under a warming climate of 20th century. A 500-year preindustrial control run with a coupled Earth System Model (NUIST-ESM, Cao et al. 2015, 2018) supported the view that the multidecadal NH monsoon variations are likely results of internal variability of the earth climate system (Wang et al. 2018). Two major sources of predictability for decadal variations of NH land monsoon rainfall are identified: North Atlantic-Southern Indian Ocean SST dipole measured by the NAID index and Interdecadal Pacific Oscillation (IPO)-like east-west Pacific Ocean SST contrast measured by the mega-ENSO index (Wang et al. 2018). It has been shown that skillful prediction of the NH land monsoon rainfall can be made a decade ahead by using a hybrid dynamic-empirical model. One may question the uncertainties associated with the model, or the nonstationarity associated with the empirical forecasting techniques. Now with increasing availability of long-term proxy records, I can look at these questions with reconstructed rainfall and SST indices, as proxy evidences alongside the model simulation results to better address the uncertainty issue.

Centennial variability of the global monsoon has been attributed to, through forced coupled model experiments, the effective radiative forcing, namely the combination of solar and volcanic forcing (Liu et al. 2009, 2012). It is worth to examine how well the Asian summer precipitation responds to the same external forcing on the centennial timescale with reconstructed proxy records.

Building upon our previous work of the Reconstructed Asian summer Precipitation (RAP) (Shi et al. 2018), here I present an in-depth analysis of the low-frequency variations of the past Asian summer precipitation on the decadal, multidecadal and centennial timescales.

4.3. Data and methods

The RAP dataset is a gridded 544-year (from AD 1470 to 2013) summer (primarily June-July-August, JJA) precipitation reconstruction generated by merging two complementary

proxies including 453 tree ring width chronologies and 71 historical documentary records over the Asian land region (8.75°S to 55.25°N, 61.25°E to 143.25°E) (Shi et al. 2018). Skillful reconstruction is found over various parts of Asia. It has been demonstrated the RAP dataset well captures the large-scale year-to-year rainfall variability over the EASM and ISM domain (together they are referred to as the Monsoon Asia), as well as the arid central Asia, and the perennial rainfall region of the Maritime Continent (MC) during the 20th century (Shi et al. 2018). The RAP is also in general agreement with other proxies (speleothems and ice cores) during the period of 1470-1920. The remarkably abrupt change of the ISM during the 1600s recorded in the upwelling proxy over the Arabian Sea is also captured by the RAP (Shi et al. 2018).

To examine the global SST patterns associated with the decadal-multidecadal variations of the RAP over the industrial period, I have examined several long records of instrumental SSTs. The Kaplan Extended SST V2 (1856 to present) is derived by statistically combining the monthly anomalies from the United Kingdom Meteorological Office historical SST data set (MOHSST5) of the Global Ocean Surface Temperature Atlas (GOSTA) (Kaplan et al. 1998) and the NOAA operational global SST analysis with in situ (ship and buoy) and satellite SST (Reynolds and Smith 1994). The spatial coverage of the Kaplan SST data is much better than that of the Hadley Centre SST data set (HadSST2) before 1900 (Nick A. Rayner et al., 2006, https://www.metoffice.gov.uk/hadobs/hadsst2/). Thus, the Kaplan Extended SST V2 dataset is used in this study. The data were provided by the NOAA/OAR/ERSL PSD, Boulder, USA (https://www.esrl.noaa.gov/psd/data/gridded/data.kaplan_sst.html). The Hadley Centre Sea Ice and Sea Surface Temperature data set (HadISST) (Rayner 2003, https://www.metoffice.gov.uk/hadobs/hadisst/) from 1870 to 2013 is also used to determine the SST pattern associated with the constructed proxy mega-ENSO indices.

This work also utilizes a collection of climate reconstructions over the Common Era overlapping with RAP, including both internal dynamic variables and external forcing. First, the recent reconstruction of global hydroclimate and dynamical variables (Steiger et al. 2018), which combine 2,978 paleoclimate proxy data with the physical constraints from an atmosphere-ocean climate model, was used. I selected the gridded 2-m air

temperature reconstruction and the reconstructed Atlantic Multidecadal Oscillation (AMO) index from this product. Two additional AMO indices (Mann et al. 2009; Wang et al. 2017b) and one NIÑO4 index (Liu et al. 2017b) were used. Besides, the global surface temperature filed reconstructed by Mann et al. (2009) were used.

Two last millennial forcing reconstructions (Crowley 2000; Mann et al. 2005) together with various reconstructed total solar irradiance (TSI) series (Schmidt et al. 2012; Vieira et al. 2011; Shapiro et al. 2011) and ice-core based volcanic eruption indices (Gao et al. 2008 and V2; Sigl et al. 2015) were used to investigate the precipitation response to external forcing. The details of procedures with which these proxy datasets were constructed are referred to the original literature and for brevity they are not repeated here.

Spectral analysis and wavelet analysis were applied to detect periodicities and their long-term changes. For the spectral analysis, the forward Fast Fourier transformation was used with the modified Daniell window with span of 4 (averaging 3 periodogram estimates). Continuous wavelet transform was applied to obtain wavelet power spectrum of the normalized variance of target time series (Torrence and Compo 1998). The software used was provided by A. Grinsted (http://www.glaciology.net/wavelet-coherence).

The empirical orthogonal function (EOF) analysis was utilized to display spatial features of the leading variability modes on different timescales. On each timescale, the EOF analysis was conducted during the time periods when the targeting periodicity is dominant based on the results of the wavelet analysis. For example, decadal EOFs were calculated during the 1700 to 1950 period when the 10- and 22-year periodicities are dominant; the multidecadal EOFs were calculated during 1470 to 1700 period when the 50-54 year periodicities are dominant. The centennial EOFs were calculated for the entire 544 years.

To extract signals of different frequencies, a 4-year running mean minus 21-year running mean was applied to the data (the RAP and SSTs) to extract the decadal component; a 21-year running mean minus 45-year running mean was applied to extract the multidecadal

component; and a 45-year smoothing minus trend was applied to the data to obtain the centennial component. I conducted sensitivity tests by comparing the results derived from two band-pass filtering methods with 8 to 40 year band-pass for decadal signal, 40 to 80 year band-pass for multidecadal signal, and 80-year low-pass onto detrended data for centennial signal. Compared to the Lanczos bandpass/lowpass filtering (Duchon 1979), the running average method used here preserves the power/magnitude of each component better without losing much data on each end of the record. While the Butterworth bandpass filter (Russell 2006) could not effectively generate any multidecadal signal after around 1900 compared with both the Lanczos bandpass filtering and the running average method.

Statistical tests for correlation and regression coefficients between the RAP and observed SSTs are determined by the effective degrees of freedom after taking into account of autocorrelations (Livezey and Chen 1983). When correlating the RAP with other reconstruction series, the correlation coefficients are considerably lower. In these cases, the statistical significance of correlation coefficients is determined with a simplified Monte Carlo method following Hope (1968), which is a relatively less strict test but still enables meaningful interpretations.

4.4. Decadal-to-centennial variability of the Asian summer rainfall

4.4.1. Major low-frequency periodicities of all Asian summer rainfall

To examine the low-frequency variability of the Asian summer rainfall, I first hope to identify the leading periodicities, and the periods during which they dominate. To this end, I first constructed an All Asian summer Rainfall Index (AARI) by area-weighted averaging summer precipitation over the entire Asian land. The rationale for making the AARI lies in the fact that the leading EOF modes on decadal, multidecadal and centennial time scales all show a nearly homogenous spatial pattern (4.4.3). Figure 4.1 shows the time series of AARI from 1470 to 2013.

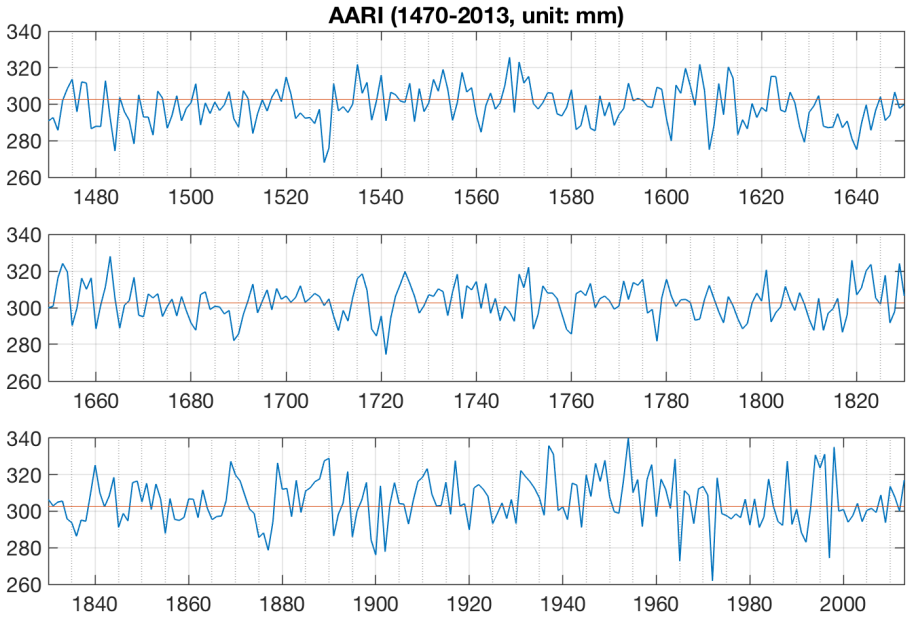

Figure 4.1 Yearly AARI (mm/summer) from 1470 to 2013. The red line is the mean precipitation (303mm) over the entire 544 years

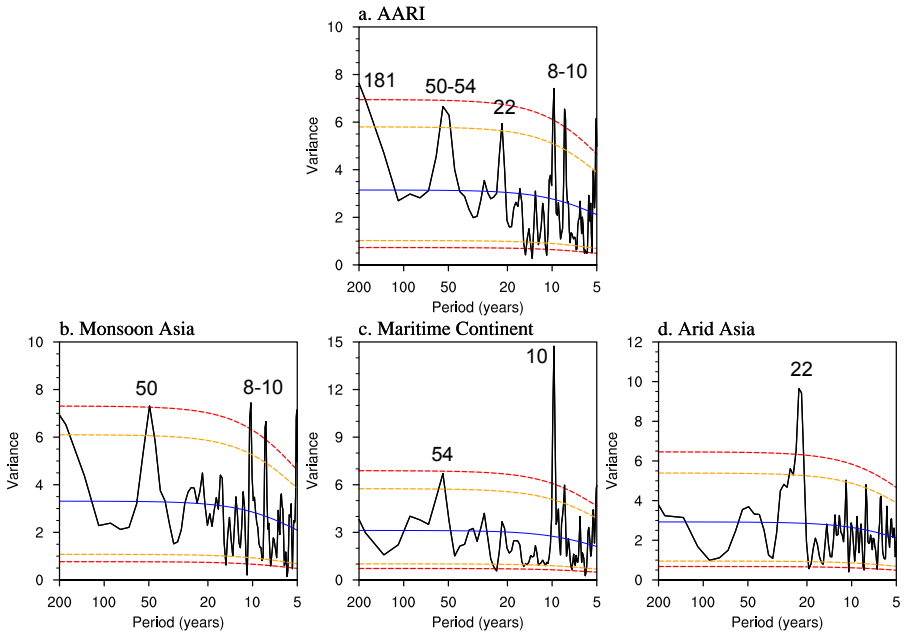

Figure 4.2 Power spectra for the AARI and regional boreal summer rainfall indices. Blue lines are the Markov Red Noise spectra. Red and orange dash lines indicate upper (lower) confidence bounds at 95% and 90% significance levels, respectively.

Spectral analysis of the yearly AARI reveals four major significant spectral peaks: decadal (8-10 years), quasi-bidecadal (22 years), multidecadal (50-54 years), and

possibly on centennial and longer time scale (Figure 4.2a). The centennial rhyme detected here appears to be consistent with the periodicity found by Liu et al. (2009) for the NH summer monsoon. The 8-10-year and ~50-year periodicities are also found in the EOF2 and EOF3 modes in Shi et al. (2018).

The wavelet analysis has detected an interesting and surprising shift of decadal-multidecadal variations that occurred around AD 1700 (Figure 4.3): Before AD 1700, the 50-year peak is the only significant and dominant periodicity (Figure 4.4, first column top), and after AD 1700, the decadal and 22-year peaks emerge and become significant periodicities (Figure 4.4, first column bottom).

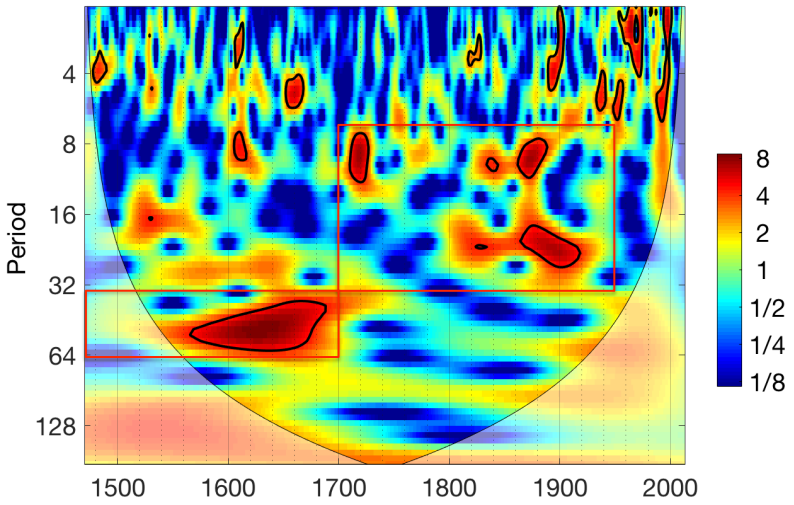

Figure 4.3 Wavelet of the AARI for 1470 to 2013 period.

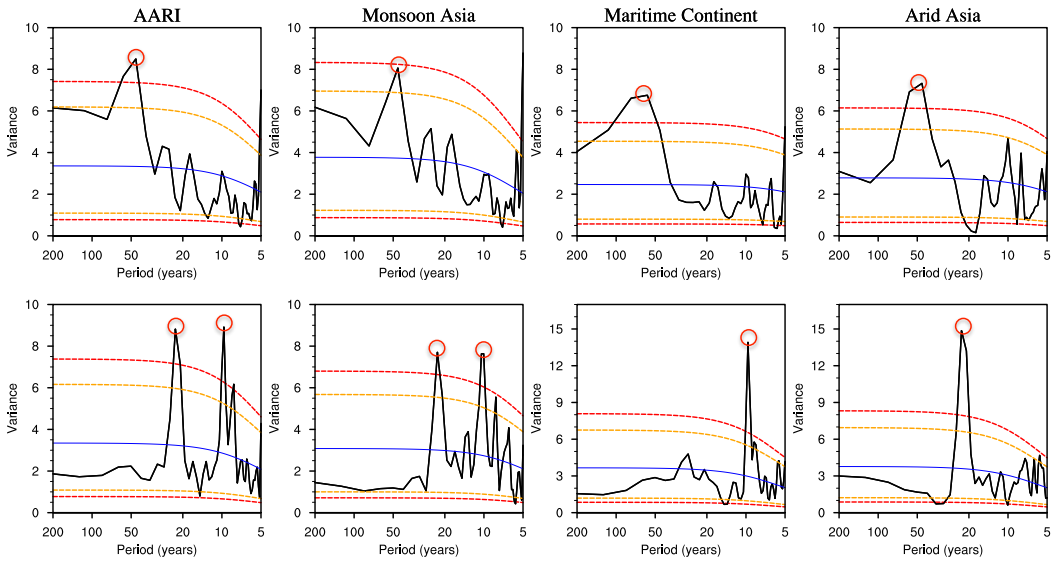

Figure 4.4 Change of the dominant periodicity in Asian summer rainfall around AD 1700. The top and bottom panels show the power spectra before and after AD 1700, respectively, for the AARI and regional boreal summer rainfall indices. Blue lines are the Markov Red Noise spectra. Red and orange dash lines indicate upper (lower) confidence bounds at 95% and 90% significance levels, respectively.

4.4.2. Regionality of the decadal to multidecadal variation of the Asian summer precipitation

To examine the regionality of the periodicities of the Asian summer rainfall, the entire Asian domain is further divided into three sub-regions: (i) the Monsoon Asia, following the definition of monsoon rainfall domain (Wang and Ding 2008); (ii) the arid Asia, defined as the region north and west of the monsoon domain where the summer rainfall below 1 mm/day; and (iii) the Maritime Continent (MC) (8.75°S to 10.25°N, 95.25°E to 143.25°E). These three regions represent three different rainfall regimes. The arid central Asia represents semi-arid region and a Mediterranean regime of rainfall (summer dry while winter wet) with wet season mainly occurring from December to March. The MC is a special region which includes primarily the perennial rain regime (Wang and LinHo 2002) but also a part of NH and southern hemisphere (SH) monsoon regions in the deep tropics. Three regional boreal summer rainfall indices are calculated with area weighting.

Power spectra of the three yearly regional rainfall indices show that the 22-year peak is mainly from the arid Asia (Figure 4.2d), while the 10- and 50-year peaks are from the monsoon Asia (Figure 4.2a) and the MC (Figure 4.2c).

Spectral analysis is further conducted for the 1470 to 1699 and 1700 to 1950 periods, separately based on the finding that an abrupt change of dominant frequency exists around AD 1700. As shown in Figure 4.4, all three regions show significant multidecadal (50-54 years) peaks before 1700 (top panel). After 1700, 10-year periodicity dominates the MC, while 22-year periodicity dominates the arid Asia (bottom panel). Both 10- and 22-year peaks appear in the monsoon Asia.

The regional spectral analysis reveals that (i) three sub-regions have collectively contributed to the major periodicities of the 544-year AARI, i.e. the 10- and 50-year periodicities by the monsoon Asia and the MC, while the 22-year peak by the arid Asia; (ii) before AD 1700 all three sub-regions are solely dominated by multidecadal (~50 year) variation without significant decadal variability; (iii) after AD 1700 all three sub-regions are dominated by decadal and quasi-bidecadal variations without significant multidecadal variation; (iv) the frequency shift from multidecadal to decadal around AD 1700 is an Asian-wide phenomenon across all three different climate regimes; and (v) the decadal variability occurs in the wet monsoon Asia and MC, while quasi-bidecadal variability mainly occur in the arid Asia as well as monsoon Asia.

4.4.3. Leading modes of decadal-to-centennial variability of the Asian summer rainfall

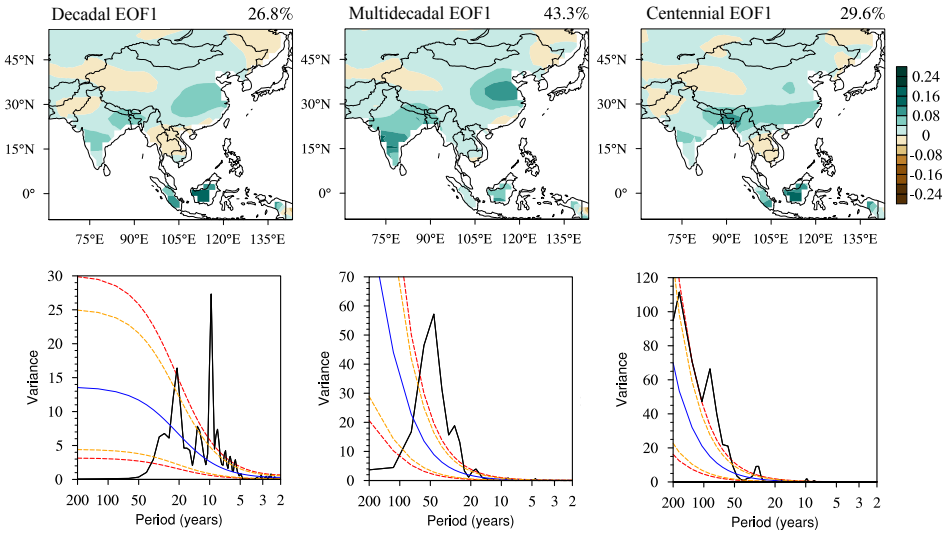

Figure 4.5 Leading EOFs on decadal to centennial timescales and power spectra of corresponding PCs.

Figure 4.5 shows the leading EOF modes on decadal (during 1700 -1950), multidecadal (during 1470-1700) and centennial timescales (during 1470-2013), respectively, as well as the power spectra of the corresponding PCs. All three EOFs show overall uniform wetting patterns with somewhat different maximum loading regions (Figure 4.5). The leading decadal mode accounts for about 27% of the total band-filtered variance with a sharp peak around 10 years. This peak is dominated by the MC rainfall as the outstanding maximum loading is seen over there. The central eastern China also shows a relatively high loading at 10-year variability. The leading mode of multidecadal variation with a peak around 50 years accounts for a large portion (43%) of the total band-filtered variance. Among the three EOFs, multidecadal EOF1 is the most uniform compared with the other two. The maximum loading is found over India and East China north of Yangtze River. This agrees with modern instrumental analysis from India and northern China (Kripalani and Kulkarni 2001), and is also shown by the long-term speleothem records in these two regions (Berkelhammer et al. 2010). The leading mode of centennial variation shows a 91-year peak and accounts for about one third of the total centennial variance with major loading at Boneo and Bangladesh.

The multidecadal PC1 is highly correlated with all three regional indices (Table 1), consistent with the results from spectral analyses of the regional indices shown in the upper panels of Figure 4.4. On the other hand, the decadal PC1, correlates with the MC and monsoon Asia indices very well but poorly with the arid Asia indices, though significant (Table 1), which is also consistent with the results of the regional spectral analyses shown in the lower panels of Figure 4.4. Centennial PC1 is highly correlated with the monsoon Asia and MC indices but poorly with the arid Asia index. The major periodicity (91 years) differs somewhat from the centennial signal in the AARI shown in Figure 4.2a.

Overall, the spatial patterns of the decadal, multidecadal and centennial variations tend to share similar spatial structure characterized by nearly in phase variations among the rainfall over South and East Asia, as well as the MC. The arid Asia shares the common 50-year periodicity with other regions before AD 1700; after AD 1700, it is dominated by

the 22-year periodicity and is less coherent with the decadal (10-year) and centennial variations of other regions.

Table 4.1 Correlation coefficients between PCs and regional RAP indices on decadal to centennial timescales. All CCs (except specified) are statistically significant at 99% significance level following Livezey and Chen (1983).

	All Asia	Monsoon Asia	Arid Asia	MC
Decadal PC1 (1700-1950)	0.86	0.63	0.39	0.91
Multidecadal PC1 (1470-1700)	0.96	0.95	0.82	0.86
Centennial PC1 (1470-2013)	0.93	0.83	*0.38 (90%)*	0.95

4.5. Causes of the decadal-to-centennial variability of the Asian summer rainfall

4.5.1. Internal factors associated with decadal PC1 (1700 to 1950)

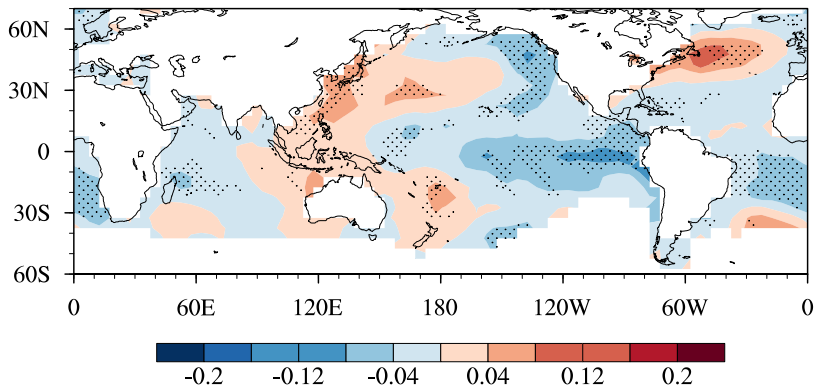

Figure 4.6 Observed decadal SST anomalies (K) regressed onto decadal RAP PC1. Dotted areas indicate statistically significant regression at 95% level following Livezey and Chen (1983). The SST data used cover the period of 1856-1950.

In order to understand the origin of the leading modes, I examine the SST anomalies associated with the leading decadal PC of Asian summer rainfall (Figure 4.6). Cold SSTs are seen over the equatorial central-eastern Pacific Ocean and warm SSTs over the subtropical western Pacific and MC, which correspond to the enhanced rainfall over the MC, Bangladesh and Yangtze River Valley (Figure 4.5). This SST anomaly pattern bears similarity with the Pacific decadal oscillation (PDO) in the North Pacific and the spatial SST pattern associated with the mega-ENSO index in the entire Pacific (Wang et al.

2013a). Over the North Atlantic, significant warming is found in mid-latitude ocean (40°-60°N) and cooling in the tropical South Atlantic (0°-30°S). The Indian Ocean features significant cooling in the southwestern part.

4.5.2. Constructing proxy mega-ENSO series

The mega-ENSO index is defined as the temperature anomalies over the western Pacific K-shape region minus the eastern Pacific triangle area (Wang et al. 2013, Figure 4.7). It is one of the key indices in studying the decadal variability of the Asian summer precipitation and NH land monsoon rainfall. However, no direct reconstruction of the mega-ENSO index is found in the literature. Thus, I use two girded global surface temperature reconstructions to construct the mega-ENSO index for the period of 1470 to 2013. To distinguish from the accurate mega-ENSO index from observation, I call it proxy mega-ENSO.

The first one is generated with the 2-m surface temperature reconstruction by Steiger et al. (2018), and it is well correlated with the observed mega-ENSO index during 1870-2013 ($r=0.86$, $p<0.01$). The other one is constructed with the surface temperature field from Mann et al. (2009), which well reflects the decadal feature of the mega-ENSO observation (4-year smoothed index) with a correlation of 0.86 ($p<0.01$) on the decadal timescale during 1870-2013.

To further justify the constructed proxy mega-ENSO indices, I calculated the correlation maps between the proxy mega-ENSO series and 4-year smoothed global SSTs from 1870 to 2013 (Figure 4.7). Both correlation patterns largely resemble the mega-ENSO pattern in the Pacific(Wang et al. 2013a).

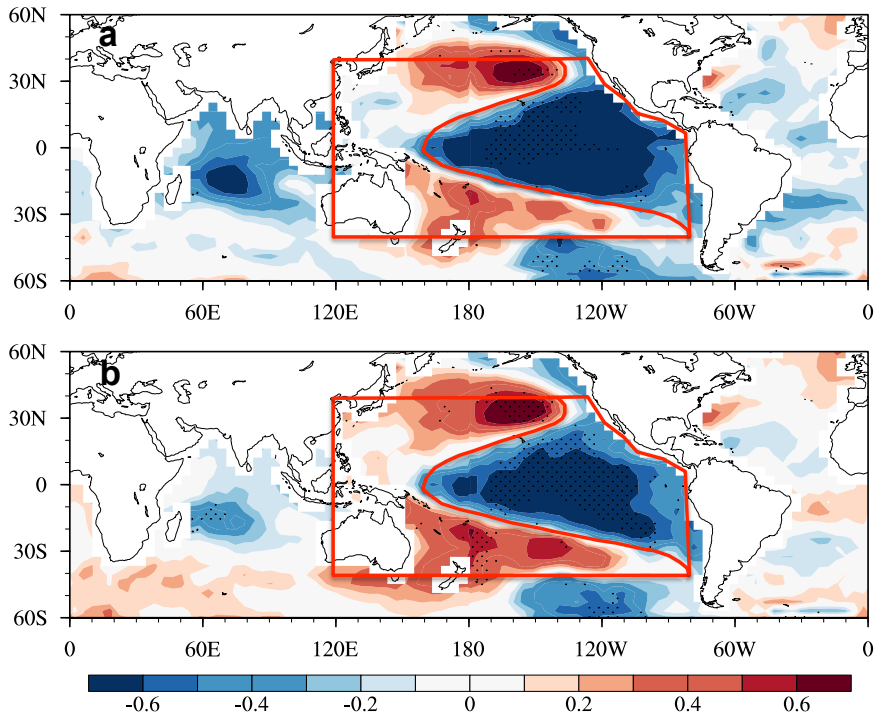

Figure 4.7 Observed decadal SST anomalies correlated with proxy mega-ENSO indices constructed with (a) Steiger and (b) Mann reconstructions. Dotted areas indicate statistically significant correlation at 95% level following Livezey and Chen (1983). The western Pacific K-shape region and the eastern Pacific triangle regions that are used to define the mega-ENSO index was outline by the red lines.

4.5.3. Internal factors associated with multidecadal AARI (1470-1700)

To examine the origins of the multidecadal variation of the Asian summer precipitation, I need SST data from 1470 to 1700. However, before 1850, no instrumental observation is available. So, I focus on the integrated quantities measured by the reconstructed oceanic indices.

Figure 4.8 compared the multidecadal component of the AARI with the multidecadal PC1, the reconstructed AMO index, as well as the constructed proxy mega-ENSO index. The 15-year smoothed AARI agrees very well with the multidecadal PC1, indicating that the AARI faithfully represents the leading mode of multidecadal variability of the entire Asia summer rainfall. The AARI is found significantly correlated with the reconstructed AMO index (Steiger et al. 2018) with a correlation coefficient of 0.40 ($p<0.05$). It is also significantly correlated with the constructed proxy mega-ENSO based on the 2-m surface temperature field (Steiger et al. 2018) ($r=0.32$, $p<0.1$). This suggests that enhanced AAR

is associated with warm North Atlantic and a mega-La Niña, a conclusion consistent with the relationship of NH land monsoon rainfall with AMO, and that with mega-ENSO during the instrumental period (Wang et al. 2018).

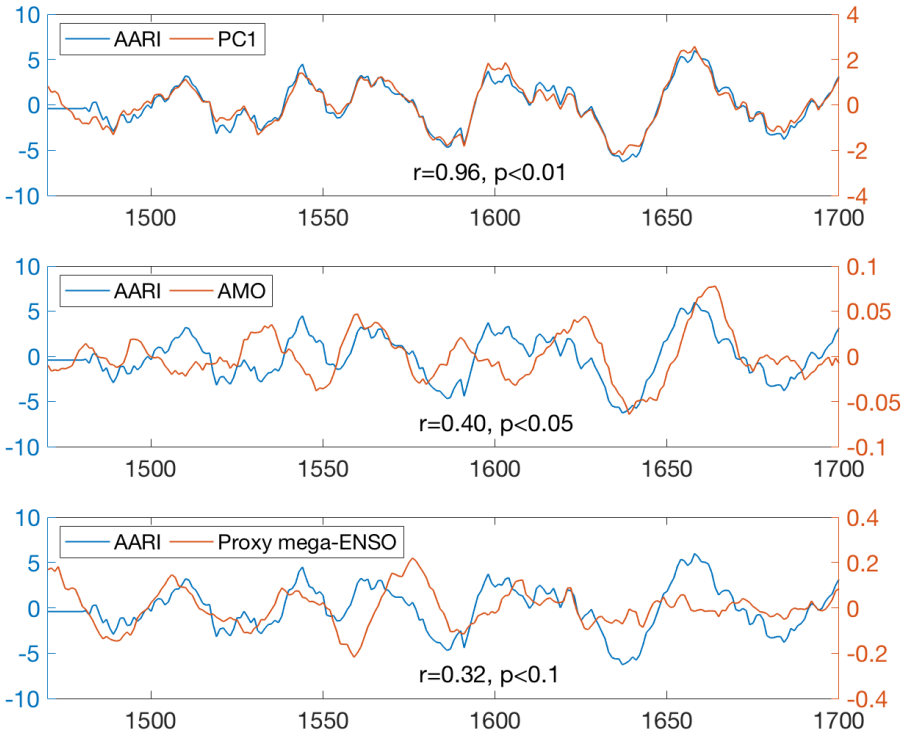

Figure 4.8 Multidecadal variation of the AARI in relation to PC1, AMO and proxy mega-ENSO during 1470 to 1700.

4.5.4. External factors associated with centennial variations of AARI

The spectral analysis of the effective radiative forcing (ERF), including insolation and volcanic forcing, indicates that the dominant periodicity of the ERF is on the centennial time scale (Liu et al. 2009). Therefore, I examine its relationship with AARI. Centennial variation of the AARI index is in an excellent agreement with the centennial PC1 (Figure 4.9a). The centennial variation of AARI seems to follow the effective radiative forcing (ERF) (Figure 4.9b) ($r=0.33$, $p<0.1$). However, by comparing individual forcing of the ERF, I found that the AARI does not correlate with the solar forcing ($r=-0.01$, insignificant), but it follows the variation of the volcanic forcing with a correlation

coefficient of 0.47 ($p<0.05$). The result here suggests existence of a significant impact of the volcanism on the AARI on the centennial time scale.

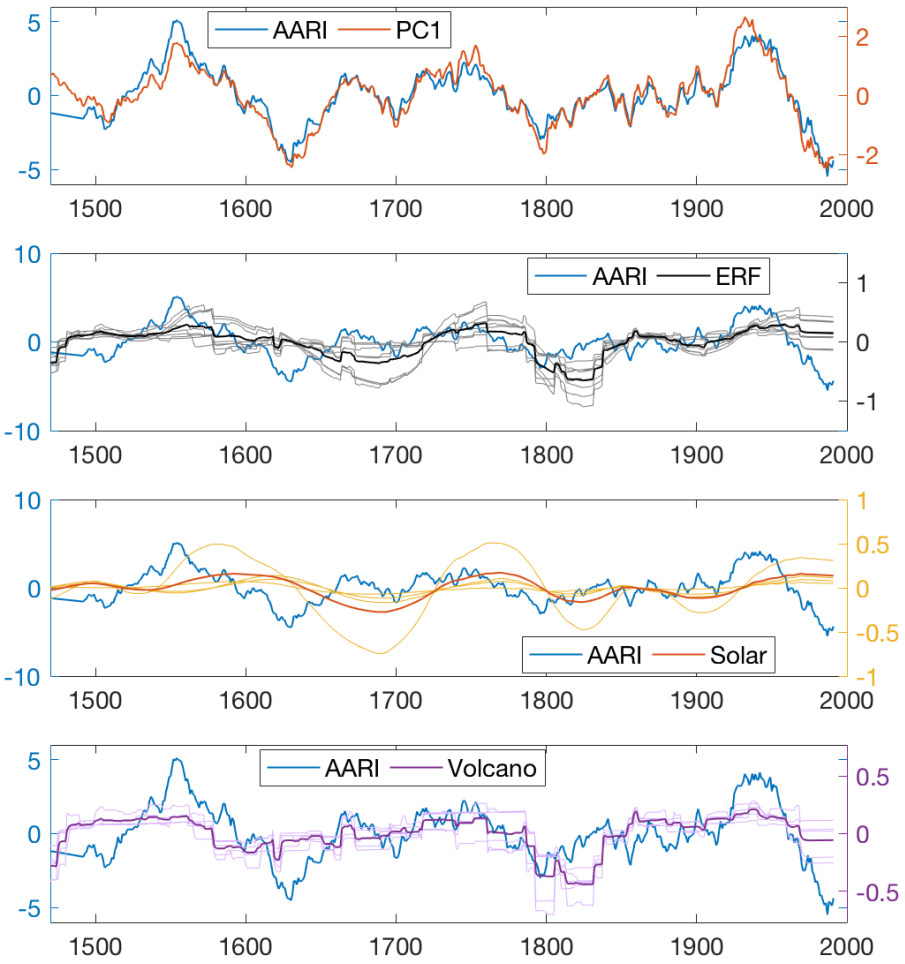

Figure 4.9 Centennial variation of the AARI in relation to PC1, effective radiative forcing, solar forcing and volcanic forcing. Thin lines are individual reconstructions, and the thick lines are average of them

4.6. Secular changes of the decadal monsoon-circulation relations

In this section, I further examine whether the relationships identified in subsection 4.1 and 4.3 have changed over the past 544 years, including the relationships between AARI and the proxy mega-ENSO, the AMO, and the volcanic forcing. Rolling correlations with 101-year window between these indices and the AARI are calculated for this purpose and

the results are shown in Figure 4.10. All series are 4-year running means (except the proxy mega-ENSO index derived using the data of Mann et al. 2009). Considerable spread can be found among the AARI correlations with each individual reconstruction (black lines, Figure 4.10), indicating uncertainties exist with the interpretations based on their averages (red thick lines, Figure 4.10).

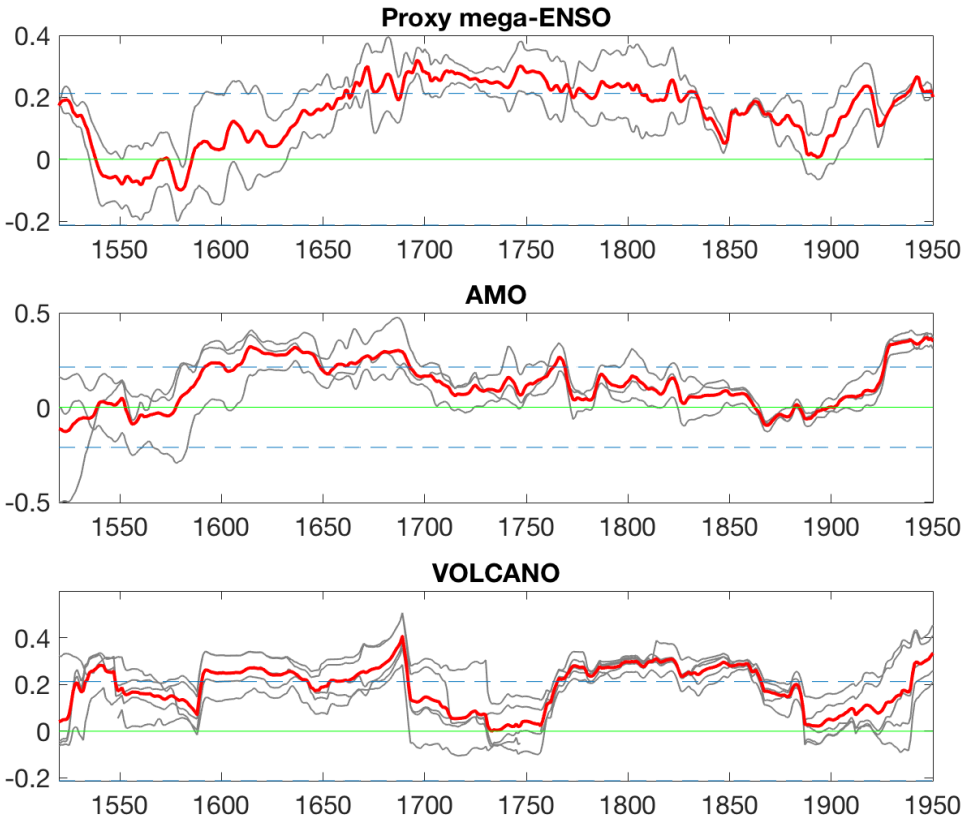

Figure 4.10 Nonstationarity of decadal relationship between AARI and proxy mega-ENSO, AMO, and volcanic forcing. Black lines are AARI correlations with each individual reconstruction, and red thick lines are average of them. Dashed lines are cutoff correlations at the 90% significance level based on a simplified Monte Carlo test (Hope, 1968).

Figure 4.10 shows that all these relationships are nonstationary. The proxy mega-ENSO-AARI relationship is largely significantly positive since around 1670, except for a brief weakening during the late 1800s and early 1900s. Before 1670, the correlation coefficient between AARI and proxy mega-ENSO is near zero and insignificant. The AMO-AARI relationship, on the other hand, is significantly positive from around 1600 to 1700. Afterwards, the relationship weakens and comes back up around 1930. One thing worth

noting is that the AARI-AMO relationship seems to resemble that between the AARI and volcanic forcing.

4.7. Discussion

4.7.1. Comparison with other observations

The 11-year and 21-year periodicities of the ISM are known in the literature. The former has been linked to the sunspot number variation (Iyengar and Raghu Kanth 2005), and the latter to tidal forcing (Campbell et al. 1983). The 50-80-year periodicity is found in the ISM with both observation and proxies (e.g. Goswami 2006; Goswami et al. 2016), and it has been largely attributed to the impact of AMO (e.g. Goswami et al. 2006; Sankar et al. 2016; Zhang and Delworth 2006).

Decadal to multidecadal periodicities are found in various parts of the EASM domain, and leading periodicities include 12 years, 27 years, 30-40 years, and 80 years (Wang et al. 2000b; Ding et al. 2008; Zhu and Wang 2002; Zhou et al. 2009). These, however, are not very consistent with the coherent changes of the Asian monsoon identified in this study, indicating strong regionality of the low-frequency variations of the EASM.

Using observed data from 1901-2015, Li et al. (2018) discussed the decadal predictability of the EA land monsoon rainfall (LMR) and established its linkage with central-eastern tropical Pacific cooling and the warming over western tropical Pacific and extratropical North Pacific during May to October. Over the Pacific Ocean sector, the SST pattern associated with the decadal PC1 (Figure 4.6) largely resembles that in their study, suggesting that the AAR and EASM may partially share the same origins of variability sources. The SST anomalies associated with the decadal PC1 (Figure 4.6) is also close to those associated with the NHLSM (Wang et al. 2018), where the mega-ENSO SST pattern dominates the entire Pacific. The warming in the northern Atlantic Ocean is less uniform compared with the SST anomalies constructing the North Atlantic-Indian Ocean dipole (NAID) index.

The AMO-ISM relationship is found nonstationary, but its behavior varies from study to study. Shi et al. (2017) found well-defined positive correlation between ISM and AMO

from late 17th century to the early 18th century, as well as after the late 19th century; Sankar et al. (2016) found a positive correlation during the last century and half, but none before 1750. Our study shows a good relationship from roughly 1590 to 1690 (Figure 4.10). Such inconsistency could be due to the monsoon proxy in use, the represented region of the proxy, and uncertainties associated with the AMO reconstructions.

Previous studies also show that the Pacific Decadal Oscillation (PDO) could play a role in the multidecadal changes of the ISM across its primary active timescale, since the timescale-dependent variations are interlinked (Shi et al. 2017a; Goswami et al. 2016). Here in our study the mega-ENSO index by definition largely represents the PDO variability (Wang et al. 2013a) and the two are inversely correlated on the decadal timescale. Our study shows that the mega-ENSO (western minus eastern Pacific) is significantly positively correlated with the monsoon on the multidecadal timescale during 1470 to 1700 (Figure 4.8). However, when the decadal component is added, the mega-ENSO-monsoon relationship largely weakened during this time period (Figure 4.10). Shi et al. (2017) shows, though with large divergence among PDO reconstructions, that the PDO-ISM relationship might have reversed sign before 1850 or earlier. Both studies suggest that the PDO-monsoon relationship is very likely nonstationary.

Previous studies have shown significant centennial (107 years) and quasi-bicentennial (192 years) periodicities of the global monsoon (Liu et al. 2009, 2012), which generally agrees with those found in the AARI (91 years and 181 years). Recently, increasing number of research have concluded that volcanic forcing plays a significant role in monsoon variability (e.g. Liu et al. 2016, 2017a, 2018), and the climate impacts of volcanic eruptions can last beyond decades through changing ocean heat content and circulation (Robock 2000; Slawinska and Robock 2018; Stenchikov et al. 2009). Our results concur with the significant impacts of volcanic eruptions on the Asian summer precipitation on the decadal to centennial timescales (Figure 4.9 and Figure 4.10).

4.7.2. The AD 1700 shift

Various proxy sources including the RAP have recorded a remarkable strengthening of the ISM during the 1600s (Sinha et al. 2011; Shi et al. 2018; Anderson et al. 2002). The

AARI also shows strengthening since about 1640 (Figure 4.1). Sinha et al. (2011) suggests that there is likely a regime shift of the ISM from break spell-dominated during 1400-1700 to active spell-dominated during 1700-2007.

One interesting finding worth noting in this study is that AD 1700 marks several evident changes in the AAR and its relationship with other major modes of climate variability. Such changes include: (i) the leading periodicity of AARI shifts from multidecadal (50-55 years) to decadal (10 and 22 years) (Figure 4.2) across all Asian land areas (Figure 4.4); (ii) the monsoon and mega-ENSO relationship strengthens as the decadal signals become dominant (Figure 4.10); and (iii) the monsoon-AMO and monsoon-volcano correlations drop around AD 1700 (Figure 4.10). Coincide with this shift, recent study of Shi and Wang (2018) found a centennial reversal of EASM-decaying ENSO relation around 1750.

What cause these abrupt changes in the Asian summer rainfall and their relationship with mega-ENSO and AMO? I speculate that both internal and external factors might be at play.

Internally, the shift of the leading periodicity of AARI from multidecadal (50-55 years) to decadal (10 and 22 years) may be linked to the changes in the decadal properties of the central Pacific (CP) El Niño events. Using a newly reconstructed NIÑO4 index, which well represents CP El Niño events (Liu et al. 2017b), I found that the decadal signal (10-year periodicity) becomes more significant during 1700 to 1950 period compared with that during 1470 to 1699 (Figure 4.11).

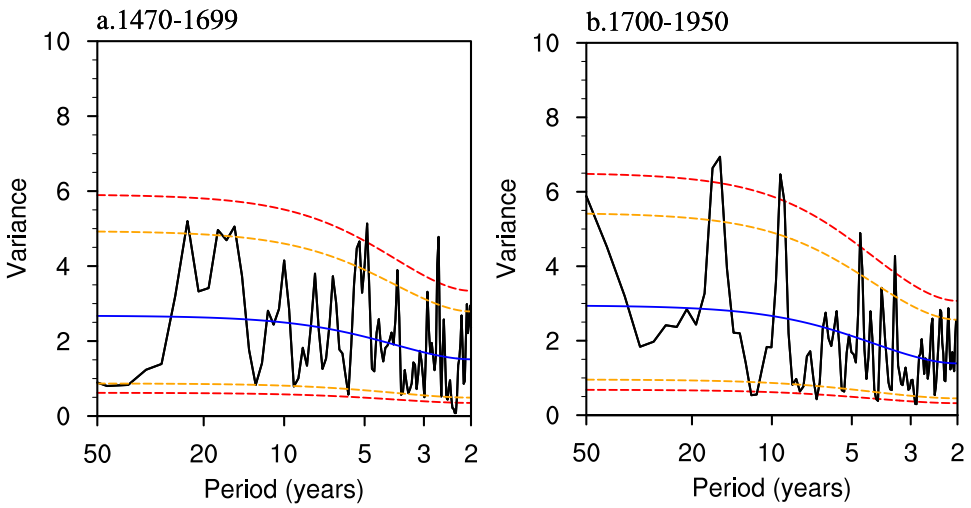

Figure 4.11 Same as Figure 4.4 but for NIÑO4 reconstruction (Liu et al., 2017) for (a) before and (b) after 1700

Externally, the AD 1700 climate shift could be linked to changes in solar and volcanic activities associated with the background climate change from the Little Ice Age (LIA) to current warming. Research has shown that AMO is influenced by external forcing and aerosol emissions (Booth et al. 2012; Otterå et al. 2010; Wang et al. 2017b). During the LIA, frequent volcanic eruptions seem to have enhanced its impacts on the AMO (Figure 4.12). The correlation between 15-year smoothed volcanic forcing series and the AMO is 0.58 ($p<0.01$) before 1850, compared with 0.36 (insignificant) after 1850. Before 1700, 58% of the variance of the AMO can be explained by the volcanic forcing ($r=0.76$, $p<0.01$), suggesting a strong tie between the two during this time period. After 1700, the correlation decreases, and the AMO-monsoon relation starts weakening (Figure 4.10).

The change of decadal variability around AD 1700 might also be related to changes in the 11-year solar cycle. Recent research by Jin et al. (2018) shows that during an epoch of strong 11-year solar cycle, this quasi-decadal insolation cycle can force a decadal variations of the EASM through exciting an anomalous SST pattern resembles that associated with the PDO. I noted that roughly after the Maunder Minimum (from 1645 to 1715, Eddy et al. 1976), solar irradiation is on the ascending half of a quasi-bicentennial cycle, during which the 11-yr solar activity increases (Abdussamatov 2016, 2015), As a result, the decadal (10-year) monsoon variability is expected to be enhanced since 1700.

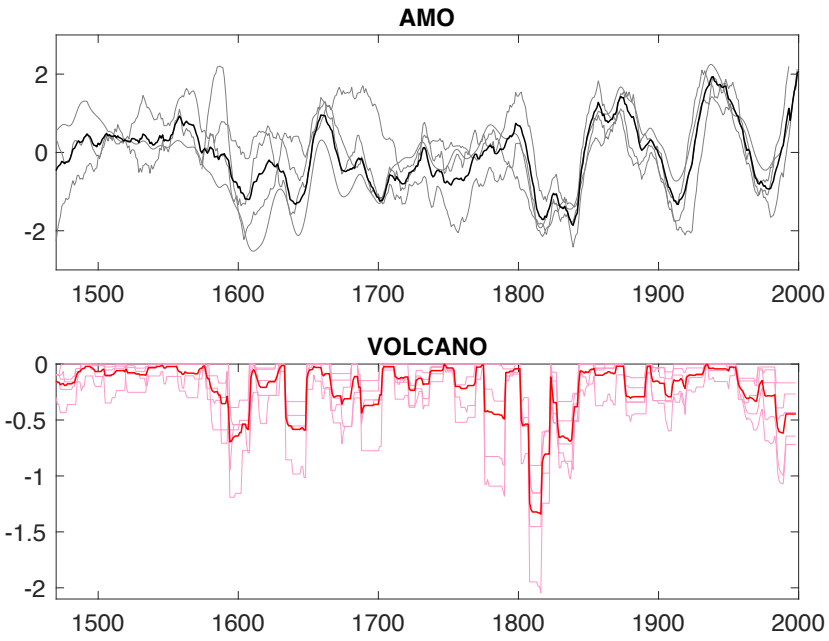

Figure 4.12 AMO and volcanic forcing since 1470. Shown are 15-year running averaged series. Thick lines are averages of all reconstructions. Thin lines are individual reconstructions, and the thick lines are average of them

4.8. Conclusions

Using the new Reconstructed Asian summer Precipitation (RAP) dataset (Shi et al. 2018) from 1470 to 2013, decadal to centennial variations of the Asian summer precipitation was examined. Some interesting findings are summarized as follows.

(i) Significant decadal (8-10 years), quasi-bidecadal (22 years), and multidecadal (50-54 years) periodicities are found in the area-averaged All Asia Rainfall Index (AARI). An evident frequency shift from multidecadal (50-54 year) to decadal occurred around AD 1700 (Figure 4.2 and Figure 4.3).

(ii) Further examination of three regional indices, which are area-weighted rainfall over the monsoon Asia, maritime continent (MC) and Arid Asia, indicates that the 10- and 50-year peaks are from the monsoon Asia and MC, while the 22-year peak is mainly from the arid Asia (Figure 4.2); before AD 1700, the 50-54 year peak is the only significant and dominant periodicity for all three regions; after AD 1700, the decadal and 22-year peaks become significant periodicities, specifically, the MC is dominated by a 10-year

periodicity; the arid Asia is dominated by a 22-year periodicity; and the monsoon Asia exhibits both 10 and 20-year periodicities (Figure 4.4).

(iii) The leading EOF modes on the decadal, multidecadal and centennial timescales all exhibit a similar spatially uniform structure, suggesting a nearly in-phase variations among the rainfall over South Asia and East Asia, as well as the MC on different time scales. The multidecadal EOF1 is the most uniform and the decadal EOF1 is the least uniform with relatively strong loading over the MC (Figure 4.5).

(iv) The leading decadal mode of Asian summer rainfall variability is associated with a mega-ENSO pattern, a north-south dipole SST pattern between the northern North Atlantic and tropical South Atlantic, and a cool southwestern Indian Ocean (Figure 4.6).

(v) Multidecadal variation (50-54 years) of the AARI is well correlated with the AMO, and the mega-ENSO index (Figure 4.8). On the centennial timescale, the RAP more closely follows the volcanic forcing rather than the effective radiative forcing, because the solar forcing does not correlate with the centennial RAP (Figure 4.9).

(vi) Both the AARI-mega-ENSO and AARI-AMO relationships are nonstationary and experience significant secular changes. The former is consistently strong *after* AD 1700, while the latter is strong *before* AD 1700 as well as after around 1930. The AARI-AMO relationship is found to some degree following that of the AARI-volcanic forcing relationship over the past 544 years. (Figure 4.10).

The present study period has its uniqueness because it covers the coldest part of the LIA and current unprecedented warming. Accompanied by many changes in the climate system associated with the transition between the two eras, I speculate that the role that external forcing played may be magnified. Frequent volcanic eruptions and solar forcing transition from minima to maxima could excite the variations of internal coupled ocean-atmospheric modes like the AMO and mega-ENSO, thus influence the global circulation/precipitation.

Volcanic impacts have been taken into consideration in the operational decadal prediction system (Illing et al. 2018). Future projections have started to include pseudo-eruption scenarios under RCPs (Bethke et al. 2017). With still little known, solar could be a potential predictability source as well (Smith et al. 2012). Understanding how these external forcings can interact with the internal dynamics from observations and reconstructions can help to identify climate models' deficiencies and to better project future changes.

Chapter 5. Concluding remarks

5.1. Key findings

In this research, a new long-term monsoon rainfall record is reconstructed and is used to explore changes in monsoon-ENSO relation and the decadal-to-centennial rainfall variability. In Chapter 2, the Reconstructed Asian summer Precipitation (RAP) dataset is generated. It spans 544 years (from AD 1470 to 2013) and covers Asian land (8.75°S-55.25°N, 61.25°E-143.25°E) with 2 by 2 degree grids (Figure 2.1). It is reconstructed by merging combining of two sets of complementary proxies including 453 tree ring width chronologies and 71 historical documentary records (Figure 2.1a), and it is evaluated with various data sources (Figure 2.2). Verified against observation, skillful reconstructions are found in East and North China, Indochina peninsula, Maritime Continent (MC), northern India and Pakistan, mid-latitude Asia, and southern Japan (Figure 2.5). Compared with each individual single proxy-type reconstruction, the RAP yields quantitatively improved validation skill (Figure 2.5, Figure 2.6). It also shows significant positive correlation with long-term instrumental records dated back to early 1800s in India and later 1700s in Seoul, Korea (Table 2.1). The RAP reproduces realistic 20^{th} century precipitation climatology (Figure 2.8) and large-scale year-to-year rainfall variability when averaged over the monsoon Asia, arid central Asia, and entire Asia (Figure 2.1b, Figure 2.9). For the pre-instrumental period, the RAP is in general agreement with other proxies such as speleothem $\delta^{18}O$ records in China and India, and ice cores over the Himalaya and Tibetan plateau (Figure 2.10). It also captures the remarkably abrupt change during the 1600s recorded in the upwelling proxy over the Arabian Sea (Figure 2.12). Overall, the RAP is shown best to illustrate large-scale rainfall variability with more uncertainties in representing small-scale or local rainfall anomalies.

The analysis of RAP variability during 544 years reveals four leading long-term variability modes of the Asian summer precipitation, including (i) a biennial El Niño-Southern Oscillation (ENSO) mode, (ii) a low-frequency ENSO mode, (iii) a central Pacific El Niño-like decadal mode, and (iv) an interdecadal mode (Figure 2.13, Figure 2.14, Figure 2.15). It provides a valuable dataset for study of the large-scale Asian summer precipitation variability, especially on the decadal and longer timescales.

In Chapter 3, the RAP is shown to have recorded the phase-dependent influences of the ENSO on Asian summer precipitation since 1470. Two major modes of *interannual* variability (Figure 3.1) are found to be associated with the ENSO developing and decaying phases, respectively (Figure 3.2, Figure 3.3). The mechanisms behind the modern monsoon-ENSO relationship can reasonably well explain the past monsoon behavior. In response to a developing ENSO, precipitation anomalies from the MC via India to northern China are in phase, and this "chain reaction" tends to be largely steady since around 1620AD (Figure 3.6, Figure 3.7) when the Indian summer monsoon abruptly strengthened (Figure 2.12c); while during the decaying phase, the summer rainfall-ENSO relationship over the Yangtze River Valley-southern East China (YRV-SEC), the MC and central Asia, has gone through large multidecadal to centennial changes over the past five centuries (Figure 3.8, Figure 3.9).

Further I found that the strengthening of the link between developing-ENSO and Indian-northern China rainfall since 1620AD concurred with a phase reversal of the Pacific Decadal Oscillation (Figure 3.10). A remarkable reversal of sign in the AM-decaying ENSO relationship occurred roughly from 1740 to 1760 over the Yangtze River valley (YRV)- southern East China (SEC) and MC, which may be associated with the long-term strengthening of ENSO intensity (Figure 3.10).

In Chapter 4, interesting features of the decadal to centennial variability of the Asian summer precipitation are documented and discussed. Significant low-frequency periodicities on decadal (8-10 years), quasi-bidecadal (22 years), semi-centennial (50-54 years), and centennial timescales are found for the area-averaged All Asian Rainfall Index (AARI) (Figure 4.2). A remarkable abrupt frequency shift from semi-centennial to

decadal occurred around AD 1700 across the entire Asian land (Figure 4.4), which nearly concurs with the dramatic upswing of the Indian summer monsoon (Figure 2.12c) and the AAR (Figure 4.1). Further more, before AD 1700, the 50-54 year peak is the only significant and dominant periodicity for the monsoon Asia, MC and arid Asia; while after AD 1700, the decadal and 22-year peaks become significant periodicities, specifically, the MC is dominated by a 10-year periodicity; the arid Asia is dominated by a 22-year periodicity; and the monsoon Asia exhibits both 10 and 20-year periodicities (Figure 4.4).

A similar spatially uniform structure is found in the three leading EOF modes of Asian summer rainfall on the decadal, semi-centennial and centennial timescales (Figure 4.5), suggesting a tendency of in-phase variations among the rainfall over South Asia, East Asia, and MC across the decadal to centennial time scales (Table 4.1). The leading decadal mode of AAR is associated with a mega-ENSO pattern in the Pacific, a cool southwestern Indian Ocean, and a north-south dipole SST pattern between the northern North Atlantic and tropical South Atlantic (Figure 4.6). The leading mode of semi-centennial (or multi-decadal variation) is significantly correlated with the reconstructed Atlantic Multidecadal Oscillation (AMO) and the proxy mega-ENSO (Figure 4.8). Centennial variation of the AAR follows more closely the volcanic forcing variation than the effective radiative forcing, while is uncorrelated with solar forcing variability (Figure 4.9). Both the AARI-mega-ENSO and AARI-AMO relationships are nonstationary and experience significant centennial changes, especially around AD 1700 (Figure 4.10). The AARI-AMO relationship is found largely following that of the AARI-volcanic forcing relationship over the past 544 years (Figure 4.10).

5.2. Discussion and future work

Many interesting phenomena arise from examining the RAP and comparing with other paleoclimate proxies, and some of them lend observational evidences to existing model studies. One impartant aspect is the nonstationarity of the monsoon-forcing (both internal and external) relationship on both interannual (Figure 3.7 and Figure 3.9) and decadal (Figure 4.10) timescales. The results call for caution to paleoclimate reconstruction as well as future projections. Knowledge of such nonstationarity could be applied to risk

model of climate extremes, as well as to tuning coupled dynamic models for improved decadal prediction skill.

However, due to the lack of circulation data in paleoclimate reconstructions, it remains a challenge to explain the mechanisms. Large spreads among the proxies introduce uncertainties, and concrete conclusions can only be obtained with utilization of model simulations and experiments. The recent simulation from Community Earth System Model (CESM) Last Millennium Ensemble (LME, Otto-Bliesner et al. 2016) provides a powerful tool to understand the climate variability of the past millennium. It includes ensemble simulations with all major natural and anthropogenic forcing, as well as various single-forcing experiments. I hope to utilize this dataset, together with the RAP to examine the AD 1700 shift found in this dissertation, as well as processes and attribution of multi-year drought/megadrought events.

The study period of this dissertation has its uniqueness because it embraces the transition from the coldest part of the Little Ice Age (LIA) to current unprecedented warming. Frequent volcanic eruptions and solar forcing changing from minima to maxima may have magnified the role external forcing played to impact precipitation. Although current warming seems to be indomitable, one cannot rule out the possibility that the coming era could be a cold one because of the little knowledge we have about the sun. The paleoclimate records in various places of the world also indicate the multi-centennial fluctuations of the earth temperature (Figure 5.1). Understanding the rainfall behavior in the LIA and during its transition could to some degree prepare us for a potential cold-future scenario.

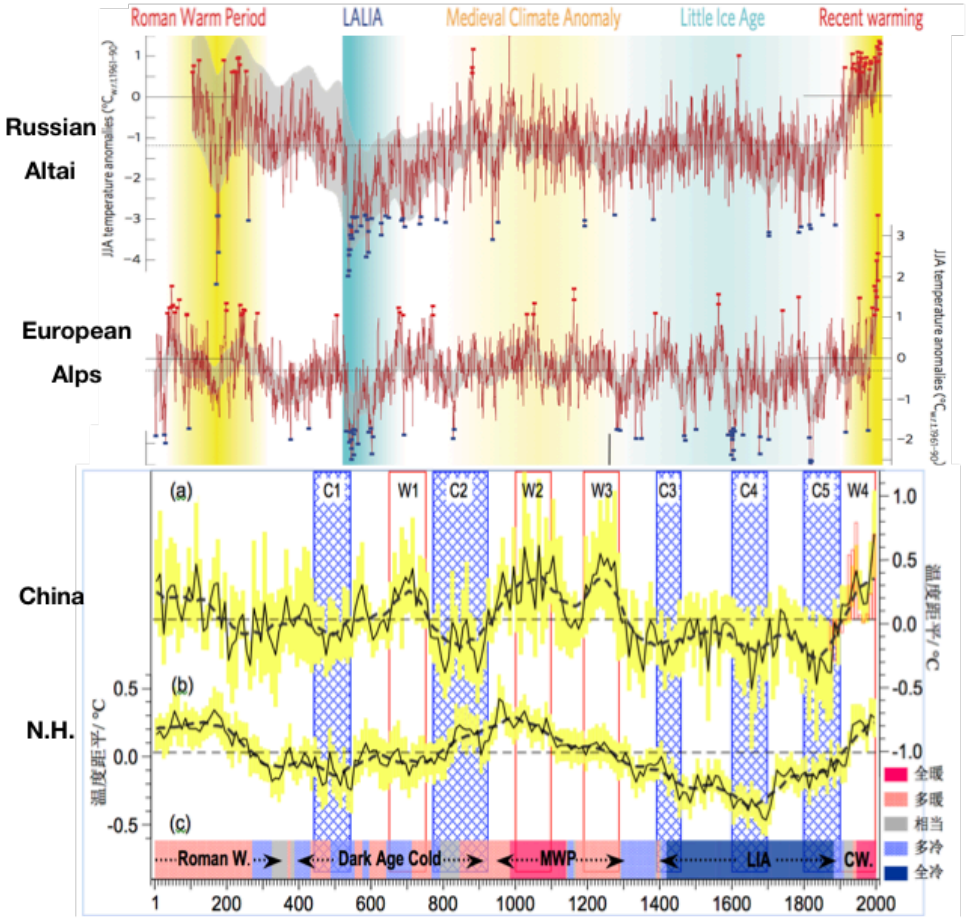

Figure 5.1 2000-year of temperature variations in different parts of the world. Figure is adapted from Büntgen et al. 2016 and Zheng et al. 2014c.

Bibliography

Abdussamatov, H., 2015: Current long-term negative average annual energy balance of the earth leads to the new little ice age. *Therm. Sci.*, **19**, 279–288.

Abdussamatov, H. I., 2016: The new Little Ice Age has started. *Evidence-Based Climate Science: Data Opposing CO2 Emissions as the Primary Source of Global Warming: Second Edition*, 307–328.

Anderson, D. M., J. T. Overpeck, and A. K. Gupta, 2002: Increase in the Asian southwest monsoon during the past four centuries. *Science (80-.).*, **297**, 596–599, doi:10.1126/science.1072881.

Ashok, K., and N. H. Saji, 2007: On the impacts of ENSO and Indian Ocean dipole events on sub-regional Indian summer monsoon rainfall. *Nat. Hazards*, **42**, 273–285, doi:10.1007/s11069-006-9091-0.

——, Z. Guan, and T. Yamagata, 2001: Impact of the Indian Ocean dipole on the relationship between the Indian monsoon rainfall and ENSO. *Geophys. Res. Lett.*, **28**, 4499–4502, doi:10.1029/2001GL013294.

——, ——, N. H. Saji, and T. Yamagata, 2004: Individual and combined influences of ENSO and the Indian Ocean Dipole on the Indian summer monsoon. *J. Clim.*, **17**, 3141–3155, doi:10.1175/1520-0442(2004)017<3141:IACIOE>2.0.CO;2.

Ashrit, R. G., K. R. Kumar, and K. K. Kumar, 2001: ENSO-monsoon relationships in a greenhouse warming scenario. *Geophys. Res. Lett.*, **28**, 1727, doi:10.1029/2000GL012489.

Barnett, T. P., L. Dümenil, U. Schlese, E. Roeckner, and M. Latif, 1989: The Effect of Eurasian Snow Cover on Regional and Global Climate Variations. *J. Atmos. Sci.*, **46**, 661–686, doi:10.1175/1520-0469(1989)046<0661:TEOESC>2.0.CO;2. http://dx.doi.org/10.1175/1520-0469(1989)046%3C0661:TEOESC%3E2.0.CO;2%5Cnhttp://journals.ametsoc.org/doi/abs/10.1175/1520-0469(1989)046%3C0661:TEOESC%3E2.0.CO;2.

Berkelhammer, M., A. Sinha, M. Mudelsee, H. Cheng, R. L. Edwards, and K. Cannariato, 2010: Persistent multidecadal power of the Indian Summer Monsoon. *Earth Planet. Sci. Lett.*, **290**, 166–172, doi:10.1016/j.epsl.2009.12.017.

Bethke, I., S. Outten, O. H. Otterå, E. Hawkins, S. Wagner, M. Sigl, and P. Thorne, 2017: Potential volcanic impacts on future climate variability. *Nat. Clim. Chang.*, **7**, 799–805, doi:10.1038/nclimate3394.

Biondi, F., A. Gershunov, and D. R. Cayan, 2001: North Pacific Decadal Climate Variability since 1661. *J. Clim.*, **14**, 5–10, doi:10.1175/1520-0442(2001)014<0005:NPDCVS>2.0.CO;2. http://journals.ametsoc.org/doi/abs/10.1175/1520-0442%282001%29014%3C0005%3ANPDCVS%3E2.0.CO%3B2.

Blanford, H. F., 1884: On the Connexion of the Himalaya Snowfall with Dry Winds and Seasons of Drought in India. *Proc. R. Soc. London*, **37**, 3–22, doi:10.1098/rspl.1884.0003. http://rspl.royalsocietypublishing.org/cgi/doi/10.1098/rspl.1884.0003.

Booth, B. B. B., N. J. Dunstone, P. R. Halloran, T. Andrews, and N. Bellouin, 2012: Aerosols implicated as a prime driver of twentieth-century North Atlantic climate

variability. *Nature*, **484**, 228–232, doi:10.1038/nature10946.
Bradley, R. S., and P. D. Jones, 1993: "Little Ice Age" summer temperature variations: their nature and relevance to recent global warming trends. *The Holocene*, **3**, 367–376, doi:10.1177/095968369300300409. http://journals.sagepub.com/doi/10.1177/095968369300300409.
Braganza, K., J. L. Gergis, S. B. Power, J. S. Risbey, and A. M. Fowler, 2009: A multiproxy index of the El Niño-Southern Oscillation, A.D. 1525-1982. *J. Geophys. Res. Atmos.*, **114**, doi:10.1029/2008JD010896.
Büntgen, U., and Coauthors, 2016: Cooling and societal change during the Late Antique Little Ice Age from 536 to around 660 AD. *Nat. Geosci.*, doi:10.1038/ngeo2652.
Bureau, C. M., 1981: Atlas of Flood and Drought in China in the Last 500 Years. *Cart. Press*, 332.
Campbell, W. H., J. B. Blechman, and R. A. Bryson, 1983: Long- period tidal forcing of Indian monsoon rainfall: an hypothesis. *J. Clim. Appl. Meteorol.*, **22**, 287–296.
Cao, J., B. Wang, B. Xiang, J. Li, T. Wu, X. Fu, L. Wu, and J. Min, 2015: Major modes of short-term climate variability in the newly developed NUIST Earth System Model (NESM). *Adv. Atmos. Sci.*, **32**, 585–600, doi:10.1007/s00376-014-4200-6.
——, and Coauthors, 2017: The NUIST Earth System Model (NESM) version 3: Description and preliminary evaluation. *Geosci. Model Dev. Discuss.*, 1–53, doi:10.5194/gmd-2017-206. https://www.geosci-model-dev-discuss.net/gmd-2017-206/.
Chang, C. P., 2004: *The East Asian Monsoon*. World Scientific Publishing Company, Singapore,.
——, P. Harr, and J. Ju, 2001: Possible roles of atlantic circulation on the weakening Indian monsoon rainfall-ENSO relationship. *J. Clim.*, **14**, 2376–2380, doi:10.1175/1520-0442(2001)014<2376:PROACO>2.0.CO;2.
——, Z. Wang, J. Ju, and T. Li, 2004: On the relationship between western maritime continent monsoon rainfall and ENSO during northern winter. *J. Clim.*, **17**, 665–672, doi:10.1175/1520-0442(2004)017<0665:OTRBWM>2.0.CO;2.
Chen, J. H., and Coauthors, 2016: On the timing of the East Asian summer monsoon maximum during the Holocene—Does the speleothem oxygen isotope record reflect monsoon rainfall variability? *Sci. China Earth Sci.*, **59**, 2328–2338, doi:10.1007/s11430-015-5500-5.
Chen, L. X., M. Dong, and Y. N. Shao, 1992: The characteristics of interannual variations on the East Asian monsoon. *J. Meteorol. Soc. Japan. Ser. II*, **70**, 397–421.
Chen, Z., X. He, E. R. Cook, H.-S. He, W. Chen, Y. Sun, and M. Cui, 2011: Detecting dryness and wetness signals from tree-rings in Shenyang, Northeast China. *Palaeogeogr. Palaeoclimatol. Palaeoecol.*, **302**, 301–310, doi:10.1016/j.palaeo.2011.01.018. http://linkinghub.elsevier.com/retrieve/pii/S0031018211000332 (Accessed November 2, 2014).
Cheng, H., and Coauthors, 2012: The climatic cyclicity in semiarid-arid central Asia over the past 500,000 years. *Geophys. Res. Lett.*, **39**, doi:10.1029/2011GL050202.
Chinese Academy of Meteorological Science, 1981: *Yearly charts of dryness/wetness in China for the last 500-year period*. Beijing, China,.
Clemens, S., 2006: Extending the historical record by proxy. *the Asian monsoon*,

Springer Berlin Heidelberg, 615–630.
Cook, E. R., 2015: Asian monsoon variability over the past millennium reconstructed from long tree-ring records: The Monsoon Asia Drought Atlas, version 2 (MADAv2). *AGU Chapman Conference: "Evolution of the Asian Monsoon and its Impact on Landscape, Environment and Society: Using the Past as the Key to the Future,"*, Hong Kong, China, Amer. Geophys. Union.
Cook, E. R., D. M. Meko, D. W. Stahle, and M. K. Cleaveland, 1999: Drought reconstructions for the continental United States. *J. Clim.*, **12**, 1145–1163, doi:10.1175/1520-0442(1999)012<1145:DRFTCU>2.0.CO;2.
——, R. Seager, M. a. Cane, and D. W. Stahle, 2007: North American drought: Reconstructions, causes, and consequences. *Earth-Science Rev.*, **81**, 93–134, doi:10.1016/j.earscirev.2006.12.002. http://linkinghub.elsevier.com/retrieve/pii/S0012825206001784.
——, R. D. D'Arrigo, and K. J. Anchukaitis, 2008: *ENSO reconstructions from long tree-ring chronologies: Unifying the differences*. H.F. Diaz, Ed.
Cook, E. R., K. J. Anchukaitis, B. M. Buckley, R. D. D'Arrigo, G. C. Jacoby, and W. E. Wright, 2010a: Asian Monsoon Failure and Megadrought During the Last Millennium. *Science (80-.).*, **328**, 486–489, doi:10.1126/science.1185188. http://www.ncbi.nlm.nih.gov/pubmed/20413498 (Accessed September 3, 2014).
Cook, E. R., K. J. Anchukaitis, B. M. Buckley, R. D. D'Arrigo, G. C. Jacoby, and W. E. Wright, 2010b: Supporting Online Material-Asian monsoon failure and megadrought during the last millennium. *Science (80-.).*, **328**, 486–489. www.sciencemag.org/cgi/content/full/328/5977/486/DC1.
Cook, E. R., P. J. Krusic, K. J. Anchukaitis, B. M. Buckley, T. Nakatsuka, and M. Sano, 2013: Tree-ring reconstructed summer temperature anomalies for temperate East Asia since 800 C.E. *Clim. Dyn.*, **41**, 2957–2972, doi:10.1007/s00382-012-1611-x.
Cosford, J., H. Qing, D. Mattey, B. Eglington, and M. Zhang, 2009: Climatic and local effects on stalagmite δ13C values at Lianhua Cave, China. *Palaeogeogr. Palaeoclimatol. Palaeoecol.*, **280**, 235–244, doi:10.1016/j.palaeo.2009.05.020.
Crowley, T. J., 2000: Causes of Climate Change Over the Past 1000 Years. *Science (80-.).*, **289**, 270–277, doi:10.1126/science.289.5477.270. http://www.sciencemag.org/cgi/doi/10.1126/science.289.5477.270.
D'Arrigo, R., R. Villalba, and G. Wiles, 2001: Tree-ring estimates of Pacific decadal climate variability. *Clim. Dyn.*, **18**, 219–224, doi:10.1007/s003820100177. http://link.springer.com/10.1007/s003820100177.
D'Arrigo, R., E. R. Cook, R. J. Wilson, R. Allan, and M. E. Mann, 2005: On the variability of ENSO over the past six centuries. *Geophys. Res. Lett.*, **32**, 1–4, doi:10.1029/2004GL022055.
Dai, A., K. E. Trenberth, and T. Qian, 2004: A Global Dataset of Palmer Drought Severity Index for 1870–2002: Relationship with Soil Moisture and Effects of Surface Warming. *J. Hydrometeorol.*, **5**, 1117–1130, doi:10.1175/JHM-386.1. http://journals.ametsoc.org/doi/abs/10.1175/JHM-386.1.
DelSole, T., and J. Shukla, 2009: Artificial skill due to predictor screening. *J. Clim.*, **22**, 331–345, doi:10.1175/2008JCLI2414.1.
Ding, Q., and B. Wang, 2005: Circumglobal teleconnection in the Northern Hemisphere summer. *J. Clim.*, **18**, 3483–3505, doi:10.1175/JCLI3473.1.

Ding, Y., and J. C. L. Chan, 2005: The East Asian summer monsoon: an overview. *Meteorol. Atmos. Phys.*, **89**, 117–142, doi:10.1007/s00703-005-0125-z. http://link.springer.com/10.1007/s00703-005-0125-z.

——, Z. Wang, and Y. Sun, 2008: Inter-decadal variation of the summer precipitation in East China and its association with decreasing Asian summer monsoon. Part I: Observed evidences. *Int. J. Climatol.*, **28**, 1139–1161, doi:10.1002/joc.1615.

——, Y. Sun, Z. Wang, Y. Zhu, and Y. Song, 2009: Inter-decadal variation of the summer precipitation in China and its association with decreasing Asian summer monsoon Part II: Possible causes. *Int. J. Climatol.*, **29**, 1926–1944, doi:10.1002/joc.1759.

Draper, N. R., and H. Smith, 1998: *Applied Regression Analysis*. 307–312 pp.

Duan, K., T. Yao, and L. G. Thompson, 2004: Low-frequency of southern Asian monsoon variability using a 295-year record from the Dasuopu ice core in the central Himalayas. *Geophys. Res. Lett.*, **31**, doi:10.1029/2004GL020015.

Duchon, C. E., 1979: Lanczos Filtering in One and Two Dimensions. *J. Appl. Meteorol.*, doi:10.1175/1520-0450(1979)018<1016:LFIOAT>2.0.CO;2.

Eddy, J. A., P. A. Gilman, and D. E. Trotter, 1976: Solar rotation during the Maunder Minimum. *Sol. Phys.*, **46**, 3–14, doi:10.1007/BF00157550.

Emile-Geay, J., K. M. Cobb, M. E. Mann, and A. T. Wittenberg, 2013: Estimating central equatorial pacific SST variability over the past millennium. part II: Reconstructions and implications. *J. Clim.*, **26**, 2329–2352, doi:10.1175/JCLI-D-11-00511.1.

Enomoto, T., B. J. Hoskins, and Y. Matsuda, 2003: The formation mechanism of the Bonin high in August. *Q. J. R. Meteorol. Soc.*, **129**, 157–178, doi:10.1256/qj.01.211.

Fang, K., N. Davi, X. Gou, F. Chen, E. Cook, J. Li, and R. D'Arrigo, 2010: Spatial drought reconstructions for central High Asia based on tree rings. *Clim. Dyn.*, **35**, 941–951, doi:10.1007/s00382-009-0739-9. http://link.springer.com/10.1007/s00382-009-0739-9 (Accessed November 2, 2014).

——, H. Seppä, and D. Chen, 2015: Interdecadal hydroclimate teleconnections between Asia and North America over the past 600 years. *Clim. Dyn.*, **44**, 1777–1787, doi:10.1007/s00382-014-2266-6.

Feba, F., K. Ashok, and M. Ravichandran, 2018: Role of changed Indo-Pacific atmospheric circulation in the recent disconnect between the Indian summer monsoon and ENSO. *Clim. Dyn.*, 1–10, doi:10.1007/s00382-018-4207-2. http://link.springer.com/10.1007/s00382-018-4207-2.

Feng, S., Q. Hu, Q. Wu, and M. E. Mann, 2013: A gridded reconstruction of warm season precipitation for asia spanning the past half millennium. *J. Clim.*, **26**, 2192–2204, doi:10.1175/JCLI-D-12-00099.1.

Fu, C., and X. Teng, 1988: The relationship between ENSO and climate anomaly in China during the summer time (in Chinese). *Sci. Atmos. Sin.*, 133–141.

Gao, C., A. Robock, and C. Ammann, 2008: Volcanic forcing of climate over the past 1500 years: An improved ice core-based index for climate models. *J. Geophys. Res. Atmos.*, **113**, doi:10.1029/2008JD010239.

Ge, Q., J. Zheng, Z. Hao, Y. Liu, and M. Li, 2016: Recent advances on reconstruction of climate and extreme events in China for the past 2000 years. *J. Geogr. Sci.*, **26**, 827–854, doi:10.1007/s11442-016-1301-4.

Goswami, B. N., 2004: Interdecadal change in potential predictability of the Indian

summer monsoon. *Geophys. Res. Lett.*, **31**, doi:10.1029/2004GL020337.
——, 2006: The Asian Monsoon: Inter- decadal variability. *The Asian Monsoon*, B. Wang, Ed., Praxis Springer Berlin Heidelberg, 295–328.
——, M. S. Madhusoodanan, C. P. Neema, and D. Sengupta, 2006: A physical mechanism for North Atlantic SST influence on the Indian summer monsoon. *Geophys. Res. Lett.*, **33**, doi:10.1029/2005GL024803.
——, R. H. Kripalani, H. P. Borgaonkar, and B. Preethi, 2016: *Multi-Decadal Variability in Indian Summer Monsoon Rainfall Using Proxy Data*.
Gou, X., L. Gao, Y. Deng, F. Chen, M. Yang, and C. Still, 2015: An 850-year tree-ring-based reconstruction of drought history in the western Qilian Mountains of northwestern China. *Int. J. Climatol.*, **35**, 3308–3319, doi:10.1002/joc.4208.
Hahn, D. G., and J. Shukla, 1976: An Apparent Relationship between Eurasian Snow Cover and Indian Monsoon Rainfall. *J. Atmos. Sci.*, **33**, 2461–2462, doi:10.1175/1520-0469(1976)033<2461:AARBES>2.0.CO;2. http://journals.ametsoc.org/doi/abs/10.1175/1520-0469%281976%29033%3C2461%3AAARBES%3E2.0.CO%3B2.
Harris, I., P. D. Jones, T. J. Osborn, and D. H. Lister, 2014: Updated high-resolution grids of monthly climatic observations - the CRU TS3.10 Dataset. *Int. J. Climatol.*, **34**, 623–642, doi:10.1002/joc.3711. http://doi.wiley.com/10.1002/joc.3711 (Accessed July 11, 2014).
Hope, A. C. A., 1968: A Simplified Monte Carlo Significance Test Procedure. *J. R. Stat. Soc. Ser. B (Methodological),* **30**, 582–598, doi:10.2307/2984263.
Hoskins, B. J., and B. Wang, 2006: Large-scale atmospheric dynamics. *the Asian monsoon*, Springer, Berlin, Heidelberg, 357–415.
Huang, R.-H., and Y. Wu, 1989: The influence of ENSO on the summer climate change in China and its mechanism. *Adv. Atmos. Sci.*, **6**, 21–32, doi:10.1007/BF02656915.
Illing, S., C. Kadow, H. Pohlmann, and C. Timmreck, 2018: Assessing the impact of a future volcanic eruption on decadal predictions. *Earth Syst. Dyn.*, **9**, 701–715, doi:10.5194/esd-9-701-2018. https://www.earth-syst-dynam.net/9/701/2018/.
Iyengar, R. N., and S. T. G. Raghu Kanth, 2005: Intrinsic mode functions and a strategy for forecasting Indian monsoon rainfall. *Meteorol. Atmos. Phys.*, **90**, 17–36, doi:10.1007/s00703-004-0089-4.
Jin, C., J. Liu, B. Wang, M. Yan, and L. Ning, 2018: Decadal variations of East Asian Summer Monsoon forced by 11-year insolation cycle. *J. Clim.*, **submitted**.
Kang, S., A. Bräuning, and H. Ge, 2014: Tree-ring based evidence of the multi-decadal climatic oscillation during the past 200 years in north-central China. *J. Arid Environ.*, **110**, 53–59, doi:10.1016/j.jaridenv.2014.06.003.
Kaplan, A., M. A. Cane, Y. Kushnir, A. C. Clement, M. Benno Blumenthal, and B. Rajagopalan, 1998: Analyses of global sea surface temperature 1856-1991. *J. Geophys. Res.*, **103589**, 567–18, doi:10.1029/97JC01736.
Kathayat, G., and Coauthors, 2016: Indian monsoon variability on millennial-orbital timescales. *Sci. Rep.*, **6**, doi:10.1038/srep24374.
Keshavamurty, R., 1982: Response of the atmosphere to sea surface temperature anomalies over the equatorial Pacific and the teleconnections of the Southern Oscillation. *J. Atmos. Sci.*, **39**, 1241–1259, doi:10.1175/1520-0469(1982)039<1241:ROTATS>2.0.CO;2.

http://journals.ametsoc.org/doi/abs/10.1175/1520-0469(1982)039%3C1241:ROTATS%3E2.0.CO;2.
Kripalani, R. H., and A. Kulkarni, 2001: Monsoon rainfall variations and teleconnections over South and East Asia. *Int. J. Climatol.*, **21**, 603–616, doi:10.1002/joc.625.
Krishnamurthy, L., and V. Krishnamurthy, 2014: Influence of PDO on South Asian summer monsoon and monsoon-ENSO relation. *Clim. Dyn.*, **42**, 2397–2410, doi:10.1007/s00382-013-1856-z.
Kumar, K. K., B. Rajagopalan, and M. A. Cane, 1999: On the weakening relationship between the indian monsoon and ENSO. *Science (80-.).*, **284**, 2156–2159, doi:10.1126/science.284.5423.2156.
Kwon, M. H., J. G. Jhun, and K. J. Ha, 2007: Decadal change in east Asian summer monsoon circulation in the mid-1990s. *Geophys. Res. Lett.*, **34**, 1–6, doi:10.1029/2007GL031977.
Lau, K.-M., and P. J. Sheu, 1988: Annual cycle, quasi‐biennial oscillation, and southern oscillation in global precipitation. *J. Geophys. Res. Atmos.*, **93**, 10975–10988, doi:10.1029/JD093iD09p10975.
Lau, K.-M., and H. T. Wu, 2001: Principal modes of rainfall-SST variability of the Asian Summer Monsoon: A reassessment of the Monsoon-ENSO relationship. *J. Clim.*, **14**, 2880–2895, doi:10.1175/1520-0442(2001)014<2880:PMORSV>2.0.CO;2.
Lau, N. C., and M. J. Nath, 2000: Impact of ENSO on the variability of the Asian-Australian Monsoons as simulated in GCM experiments. *J. Clim.*, **13**, 4287–4309, doi:10.1175/1520-0442(2000)013<4287:IOEOTV>2.0.CO;2.
Lee, J. Y., and B. Wang, 2014: Future change of global monsoon in the CMIP5. *Clim. Dyn.*, **42**, 101–119, doi:10.1007/s00382-012-1564-0.
Li, H. C., D. L. Gu, and L. D. Stott, 1998: Applications of interannual-resolution stable isotope records of speleothem: climatic changes in Beijing and Tianjin, China during the past 500 years - the delta O-18 record. *Sci. China Ser. D-Earth Sci.*, 362–368.
Li, J., X. Gou, E. R. Cook, and F. Chen, 2006: Tree-ring based drought reconstruction for the central Tien Shan area in northwest China. *Geophys. Res. Lett.*, **33**, doi:10.1029/2006GL025803.
——, S. P. Xie, E. R. Cook, G. Huang, R. D'arrigo, F. Liu, J. Ma, and X. T. Zheng, 2011: Interdecadal modulation of El Niño amplitude during the past millennium. *Nat. Clim. Chang.*, **1**, 114–118, doi:10.1038/nclimate1086.
——, and Coauthors, 2013: El Niño modulations over the past seven centuries. *Nat. Clim. Chang.*, **3**, 822–826, doi:10.1038/nclimate1936.
——, S. P. Xie, and E. R. Cook, 2014: El Niño phases embedded in Asian and North American drought reconstructions. *Quat. Sci. Rev.*, **85**, 20–34, doi:10.1016/j.quascirev.2013.11.014.
Li, J., B. Wang, J. Li, and B. Wang, 2018: Origins of the decadal predictability of East Asian land summer monsoon rainfall. *J. Clim.*, JCLI-D-17-0790.1, doi:10.1175/JCLI-D-17-0790.1. http://journals.ametsoc.org/doi/10.1175/JCLI-D-17-0790.1.
Li, T., B. Wang, C.-P. Chang, and Y. Zhang, 2003: A Theory for the Indian Ocean Dipole–Zonal Mode*. *J. Atmos. Sci.*, **60**, 2119–2135, doi:10.1175/1520-0469(2003)060<2119:ATFTIO>2.0.CO;2. http://journals.ametsoc.org/doi/abs/10.1175/1520-

0469%282003%29060%3C2119%3AATFTIO%3E2.0.CO%3B2.
Li, Z. H., J. H. Zhu, J. N. Cai, and S. W. Wang, 2005: Flood in Huaihe Valley Since 1470. *Meteorology*, **31**, 24–28.
Liu, F., J. Chai, B. Wang, J. Liu, X. Zhang, and Z. Wang, 2016: Global monsoon precipitation responses to large volcanic eruptions. *Sci. Rep.*, **6**, doi:10.1038/srep24331.
——, J. Li, B. Wang, J. Liu, T. Li, G. Huang, and Z. Wang, 2017a: Divergent El Niño responses to volcanic eruptions at different latitudes over the past millennium. *Climate Dynamics*.
——, T. Zhao, B. Wang, J. Liu, and W. Luo, 2018: Different Global Precipitation Responses to Solar, Volcanic, and Greenhouse Gas Forcings. *J. Geophys. Res. Atmos.*, **123**, 4060–4072, doi:10.1029/2017JD027391.
Liu, J., B. Wang, Q. Ding, X. Kuang, W. Soon, and E. Zorita, 2009: Centennial variations of the global monsoon precipitation in the last millennium: Results from ECHO-G model. *J. Clim.*, **22**, 2356–2371, doi:10.1175/2008JCLI2353.1.
——, ——, S. Y. Yim, J. Y. Lee, J. G. Jhun, and K. J. Ha, 2012: What drives the global summer monsoon over the past millennium? *Clim. Dyn.*, **39**, 1063–1072, doi:10.1007/s00382-012-1360-x.
Liu, Y., and Coauthors, 2017b: Recent enhancement of central Pacific El Niño variability relative to last eight centuries. *Nat. Commun.*, **8**, doi:10.1038/ncomms15386.
Livezey, R. E., and W. Y. Chen, 1983: Statistical Field Significance and its Determination by Monte Carlo Techniques. *Mon Weather Rev,* **111**, 46–59.
MacDonald, G. M., and R. A. Case, 2005: Variations in the Pacific Decadal Oscillation over the past millennium. *Geophys. Res. Lett.*, **32**, L08703, doi:10.1029/2005GL022478. http://doi.wiley.com/10.1029/2005GL022478.
Mann, M. E., E. Gille, J. Overpeck, W. Gross, R. S. Bradley, F. T. Keimig, and M. K. Hughes, 2000: Global Temperature Patterns in Past Centuries: An Interactive Presentation. *Earth Interact.*, **4**, 1–1, doi:10.1175/1087-3562(2000)004<0001:GTPIPC>2.3.CO;2. http://journals.ametsoc.org/doi/abs/10.1175/1087-3562%282000%29004%3C0001%3AGTPIPC%3E2.3.CO%3B2.
——, M. A. Cane, S. E. Zebiak, and A. Clement, 2005: Volcanic and solar forcing of the tropical Pacific over the past 1000 years. *J. Clim.*, **18**, 447–456, doi:10.1175/JCLI-3276.1.
——, and Coauthors, 2009: Global signatures and dynamical origins of the little ice age and medieval climate anomaly. *Science (80-.).*, **326**, 1256–1260, doi:10.1126/science.1177303.
McGregor, S., A. Timmermann, and O. Timm, 2010: A unified proxy for ENSO and PDO variability since 1650. *Clim. Past*, **6**, 1–17, doi:10.5194/cp-6-1-2010.
Meehl, G. A., and Coauthors, 2007: 2007: Global Climate Projections. *Clim. Chang. 2007 Contrib. Work. Gr. I to Fourth Assess. Rep. Intergov. Panel Clim. Chang.*, 747–846, doi:10.1080/07341510601092191. http://www.ipcc.ch/pdf/assessment-report/ar4/wg1/ar4-wg1-chapter10.pdf.
Mooley, D. A., and B. Parthasarathy, 1984: Indian summer monsoon and the east equatorial pacific sea surface temperature. *Atmosphere-Ocean*, **22**, 23–35, doi:10.1080/07055900.1984.9649182.

http://www.tandfonline.com/doi/abs/10.1080/07055900.1984.9649182.
——, and A. A. Munot, 1993: Variation in the relationship of the Indian summer monsoon with global factors. *Proc. Indian Acad. Sci. - Earth Planet. Sci.*, **102**, 89–104, doi:10.1007/BF02839184.
Otterå, O. H., M. Bentsen, H. Drange, and L. Suo, 2010: External forcing as a metronome for Atlantic multidecadal variability. *Nat. Geosci.*, **3**, 688–694, doi:10.1038/ngeo955.
Otto-Bliesner, B. L., and Coauthors, 2016: Climate Variability and Change since 850 CE: An Ensemble Approach with the Community Earth System Model. *Bull. Am. Meteorol. Soc.*, **97**, 735–754, doi:10.1175/BAMS-D-14-00233.1. http://journals.ametsoc.org/doi/10.1175/BAMS-D-14-00233.1.
Palmer, T. N., Č. Branković, P. Viterbo, and M. J. Miller, 1992: Modeling Interannual Variations of Summer Monsoons. *J. Clim.*, **5**, 399–417, doi:10.1175/1520-0442(1992)005<0399:MIVOSM>2.0.CO;2. http://journals.ametsoc.org/doi/abs/10.1175/1520-0442%281992%29005%3C0399%3AMIVOSM%3E2.0.CO%3B2.
Rasmusson, E. M., and T. H. Carpenter, 1983: The Relationship Between Eastern Equatorial Pacific Sea Surface Temperatures and Rainfall over India and Sri Lanka. *Mon. Weather Rev.*, **111**, 517–258, doi:10.1175/1520-0493(1983)111<0517:TRBEEP>2.0.CO;2.
Rayner, N. A., 2003: Global analyses of sea surface temperature, sea ice, and night marine air temperature since the late nineteenth century. *J. Geophys. Res.*, **108**, 4407, doi:10.1029/2002JD002670. http://doi.wiley.com/10.1029/2002JD002670.
Rayner, N. A., P. Brohan, D. E. Parker, C. K. Folland, J. J. Kennedy, M. Vanicek, T. J. Ansell, and S. F. B. Tett, 2006: Improved analyses of changes and uncertainties in sea surface temperature measured in Situ since the mid-nineteenth century: The HadSST2 dataset. *J. Clim.*, **19**, 446–469, doi:10.1175/JCLI3637.1.
Reynolds, R. W., and T. M. Smith, 1994: Improved global sea surface temperature analyses using optimum interpolation. *J. Clim.*, **7**, 929–948, doi:10.1175/1520-0442(1994)007<0929:IGSSTA>2.0.CO;2.
Robock, A., 2000: Volcanic eruptions and climate. *Rev. Geophys.*, **38**, 191–219, doi:10.1029/1998RG000054.
Ropelewski, C. F., and M. S. Halpert, 1987: Global and regional scale precipitation patterns associated with the El-Nino/southern oscillation. *Mon. Weather Rev.*, **115**, 1606–1626, doi:10.1175/1520-0493(1987)115<1606:GARSPP>2.0.CO;2. http://portal.iri.columbia.edu/portal/server.pt/gateway/PTARGS_0_5643_7853_0_0_18/Ropelewski.and.Halpert.1987.patterns.precip.enso.pdf%5Cnpapers2://publication/uuid/88EE2AC4-654A-4BC1-A754-0B8D50820D7E.
Russell, D., 2006: Electronic Supplement to Development of a Time-Domain, Variable-Period Surface Wave Magnitude Procedure for Application at Regional and Teleseismic Distances, Part I: Theory. *Bull. Seismol. Soc. Am.*,. http://www.seismosoc.org/Publications/BSSA_html/bssa_96-2/05055-esupp/.
Saji, N. H., B. N. Goswami, P. N. Vinayachandran, and T. Yamagata, 1999: A dipole mode in the tropical Indian ocean. *Nature*, **401**, 360–363, doi:10.1038/43855.
Sankar, S., L. Svendsen, B. Gokulapalan, P. V Joseph, and O. M. Johannessen, 2016: The relationship between Indian summer monsoon rainfall and Atlantic multidecadal

variability over the last 500 years. *Tellus, Ser. A Dyn. Meteorol. Oceanogr.*, **68**, doi:10.3402/tellusa.v68.31717. https://www.scopus.com/inward/record.uri?eid=2-s2.0-85011005552&doi=10.3402%2Ftellusa.v68.31717&partnerID=40&md5=382ff9e7965689cc6ce9d2b3ff647232.

Schmidt, G. A., and Coauthors, 2012: Climate forcing reconstructions for use in PMIP simulations of the Last Millennium (v1.1). *Geosci. Model Dev.*, **5**, 185–191, doi:10.5194/gmd-5-185-2012.

Schneider, U., A. Becker, P. Finger, A. Meyer-Christoffer, B. Rudolf, and M. Ziese, 2015: *GPCC Full Data Reanalysis Version 7.0 at 0.5°: Monthly Land-Surface Precipitation from Rain-Gauges built on GTS-based and Historic Data*. 1-13 pp. ftp://ftp.dwd.de/pub/data/gpcc/html/fulldata_v7_doi_download.html.

Seber, G. A., 1984: *Multivariate Observations*. G.A.F. Seber, Ed. John Wiley & Sons, Inc., Hoboken, NJ, USA, 686 pp. http://doi.wiley.com/10.1002/9780470316641.

Shao, X., L. Huang, H. Liu, E. Liang, X. Fang, and L. Wang, 2005: Reconstruction of precipitation variation from tree rings in recent 1000 years in Delingha, Qinghai. *Sci. China Ser. D*, **48**, 939, doi:10.1360/03yd0146. http://219.238.6.200/article?code=03yd0146&jccode=08.

Shapiro, A. I., W. Schmutz, E. Rozanov, M. Schoell, M. Haberreiter, A. V. Shapiro, and S. Nyeki, 2011: A new approach to the long-term reconstruction of the solar irradiance leads to large historical solar forcing. *Astron. Astrophys.*, **529**, A67.

Shen, C., W.-C. Wang, W. Gong, and Z. Hao, 2006: A Pacific Decadal Oscillation record since 1470 AD reconstructed from proxy data of summer rainfall over eastern China. *Geophys. Res. Lett.*, **33**, L03702, doi:10.1029/2005GL024804. http://doi.wiley.com/10.1029/2005GL024804.

Shi, F., B. Yang, A. Mairesse, L. Von Gunten, J. Li, A. Bräuning, F. Yang, and X. Xiao, 2013: Northern Hemisphere temperature reconstruction during the last millennium using multiple annual proxies. *Clim. Res.*, **56**, 231–244, doi:10.3354/cr01156.

——, J. Li, and R. J. S. Wilson, 2014: A tree-ring reconstruction of the South Asian summer monsoon index over the past millennium. *Sci. Rep.*, **4**, doi:10.1038/srep06739.

——, K. Fang, C. Xu, Z. Guo, and H. P. Borgaonkar, 2017a: Interannual to centennial variability of the South Asian summer monsoon over the past millennium. *Clim. Dyn.*, **49**, 2803–2814, doi:10.1007/s00382-016-3493-9.

——, S. Zhao, Z. Guo, H. Goosse, and Q. Yin, 2017b: Multi-proxy reconstructions of May-September precipitation field in China over the past 500 years. *Clim. Past*, **13**, 1919–1938, doi:10.5194/cp-13-1919-2017.

Shi, H., and B. Wang, 2018: How does the Asian summer precipitation-ENSO relationship change over the past 544 years? *Clim. Dyn.*, doi:10.1007/s00382-018-4392-z. http://link.springer.com/10.1007/s00382-018-4392-z.

——, ——, E. R. Cook, J. Liu, and F. Liu, 2018: Asian Summer Precipitation over the Past 544 Years Reconstructed by Merging Tree Rings and Historical Documentary Records. *J. Clim.*, **31**, 7845–7861, doi:10.1175/JCLI-D-18-0003.1. http://journals.ametsoc.org/doi/10.1175/JCLI-D-18-0003.1.

Shukla, J., and D. A. a Mooley, 1987: Empirical Prediction of the Summer Monsoon Rainfall over India. *Mon. Weather Rev.*, **115**, 695–704, doi:10.1175/1520-

0493(1987)115<0695:EPOTSM>2.0.CO;2. http://www.scopus.com/inward/record.url?eid=2-s2.0-0023486795&partnerID=tZOtx3y1.

Sigl, M., and Coauthors, 2015: Timing and climate forcing of volcanic eruptions for the past 2,500 years. *Nature*, **523**, 543–549, doi:10.1038/nature14565.

Sikka, D. R., 1980: Some aspects of the large scale fluctuations of summer monsoon rainfall over India in relation to fluctuations in the planetary and regional scale circulation parameters. *Proc. Indian Acad. Sci. - Earth Planet. Sci.*, **89**, 179–195, doi:10.1007/BF02913749.

Sinha, A., K. G. Cannariato, L. D. Stott, H. Cheng, R. L. Edwards, M. G. Yadava, R. Ramesh, and I. B. Singh, 2007: A 900-year (600 to 1500 A.D.) record of the Indian summer monsoon precipitation from the core monsoon zone of India. *Geophys. Res. Lett.*, **34**, doi:10.1029/2007GL030431.

——, M. Berkelhammer, L. Stott, M. Mudelsee, H. Cheng, and J. Biswas, 2011: The leading mode of Indian Summer Monsoon precipitation variability during the last millennium. *Geophys. Res. Lett.*, **38**, doi:10.1029/2011GL047713.

——, G. Kathayat, H. Cheng, S. F. M. Breitenbach, M. Berkelhammer, M. Mudelsee, J. Biswas, and R. L. Edwards, 2015: Trends and oscillations in the Indian summer monsoon rainfall over the last two millennia. *Nat. Commun.*, **6**, doi:10.1038/ncomms7309.

Slawinska, J., and A. Robock, 2018: Impact of volcanic eruptions on decadal to centennial fluctuations of Arctic sea ice extent during the Last Millennium and on initiation of the Little Ice Age. *J. Clim.*, **31**, 2145–2167, doi:10.1175/JCLI-D-16-0498.1.

Smith, D. M., A. A. Scaife, and B. P. Kirtman, 2012: What is the current state of scientific knowledge with regard to seasonal and decadal forecasting? *Environ. Res. Lett.*, **7**, doi:10.1088/1748-9326/7/1/015602.

Sontakke, N. A., N. Singh, and H. N. Singh, 2008: Instrumental period rainfall series of the Indian region (AD 1813-2005): Revised reconstruction, update and analysis. *Holocene*, **18**, 1055–1066, doi:10.1177/0959683608095576.

Spath, H., 1985: *Cluster dissection and analysis: theory, FORTRAN programs, examples*. New York: Halsted Press, 226 pp.

Stahle, D. S., and Coauthors, 1998: Experimental Dendroclimatic Reconstruction of the Southern Oscillation. *Bull. Am. Meteorol. Soc.*, **79**, 2137–2152, doi:10.1175/1520-0477(1998)079<2137:EDROTS>2.0.CO;2.

Steiger, N. J., J. E. Smerdon, E. R. Cook, and B. I. Cook, 2018: A reconstruction of global hydroclimate and dynamical variables over the Common Era. *Sci. Data*, **5**, 180086, doi:10.1038/sdata.2018.86. http://www.nature.com/articles/sdata201886.

Stenchikov, G., T. L. Delworth, V. Ramaswamy, R. J. Stouffer, A. Wittenberg, and F. Zeng, 2009: Volcanic signals in oceans. *J. Geophys. Res. Atmos.*, **114**, doi:10.1029/2008JD011673.

Tan, L., Y. Cai, H. Cheng, Z. An, and R. L. Edwards, 2009: Summer monsoon precipitation variations in central China over the past 750 years derived from a high-resolution absolute-dated stalagmite. *Palaeogeogr. Palaeoclimatol. Palaeoecol.*, **280**, 432–439, doi:10.1016/j.palaeo.2009.06.030.

——, ——, Z. An, R. L. Edwards, H. Cheng, C. C. Shen, and H. Zhang, 2011:

Centennial- to decadal-scale monsoon precipitation variability in the semi-humid region, northern China during the last 1860 years: Records from stalagmites in huangye cave. *Holocene*, **21**, 287–296, doi:10.1177/0959683610378880.

——, and Coauthors, 2015: A Chinese cave links climate change, social impacts, and human adaptation over the last 500 years. *Sci. Rep.*, **5**, doi:10.1038/srep12284.

Tan, M., 2016: Circulation background of climate patterns in the past millennium: Uncertainty analysis and re-reconstruction of ENSO-like state. *Sci. China Earth Sci.*, **59**, 1225–1241, doi:10.1007/s11430-015-5256-6.

Tejavath, C. T., A. Karumuri, S. Chakraborty, and R. Ramesh, 2017: The Indian summer monsoon climate during the Last Millennium, as simulated by the PMIP3. *Clim. Past Discuss.*, 1–27, doi:10.5194/cp-2017-24. https://www.clim-past-discuss.net/cp-2017-24/.

Thompson, L. G., 1997: Tropical Climate Instability: The Last Glacial Cycle from a Qinghai-Tibetan Ice Core. *Science (80-.).*, **276**, 1821–1825, doi:10.1126/science.276.5320.1821. http://www.sciencemag.org/cgi/doi/10.1126/science.276.5320.1821.

——, T. Yao, E. Mosley-Thompson, M. E. Davis, K. A. Henderson, and P. N. Lin, 2000: A high-resolution millennial record of the South Asian Monsoon from Himalayan ice cores. *Science (80-.).*, **289**, 1916–1919, doi:10.1126/science.289.5486.1916.

Thompson, L. G., and Coauthors, 2006a: Abrupt tropical climate change: Past and present. *Proc. Natl. Acad. Sci.*, **103**, 10536–10543, doi:10.1073/pnas.0603900103. http://www.pnas.org/content/103/28/10536.abstract.

Thompson, L. G., T. Yao, M. E. Davis, E. Mosley-Thompson, T. A. Mashiotta, P. N. Lin, V. N. Mikhalenko, and V. S. Zagorodnov, 2006b: Holocene climate variability archived in the Puruogangri ice cap on the central Tibetan Plateau. *Annals of Glaciology*, Vol. 43 of, 61–69.

Torrence, C., and G. P. Compo, 1998: A Practical Guide to Wavelet Analysis. *Bull. Am. Meteorol. Soc.*, **79**, 61–78, doi:10.1175/1520-0477(1998)079<0061:APGTWA>2.0.CO;2.

Vieira, L. E. A., S. K. Solanki, N. A. Krivova, and I. Usoskin, 2011: Evolution of the solar irradiance during the Holocene⋆⋆⋆; Evolution of the solar irradiance during the Holocene⋆⋆⋆. *A&A*, **531**, doi:10.1051/0004-6361/201015843.

Walker, G. T., and E. W. Bliss, 1932: World Weather V - NAO. *Mem. R. Meteorol. Soc.*, **IV**, 54–84, doi:10.1002/qj.49705422601.

Wang, B., 2006a: *The Asian Monsoon*. 787 pp. http://books.google.com/books?id=yRT57TENzT8C&pg=PT206&lpg=PT206&dq=weather+along+the+monsoon+trough&source=web&ots=JOJ27ZXYPw&sig=jNIakYHsIFFL9XXUYd6aA1CEdfw&hl=en#PPT207,M1%0Ahttp://link.springer.com/10.1007/3-540-37722-0.

——, 2006b: *the Asian monsoon*. Springer Science & Business Media,.

——, and Z. Fan, 1999: Choice of South Asian Summer Monsoon Indices. *Bull. Am. Meteorol. Soc.*, **80**, 629–638, doi:10.1175/1520-0477(1999)080<0629:COSASM>2.0.CO;2.

——, and LinHo, 2002: Rainy Season of the Asian–Pacific Summer Monsoon*. *J. Clim.*, **15**, 386–398, doi:10.1175/1520-0442(2002)015<0386:RSOTAP>2.0.CO;2. http://journals.ametsoc.org/doi/abs/10.1175/1520-

0442%282002%29015%3C0386%3ARSOTAP%3E2.0.CO%3B2.
——, and T. Li, 2004: East Asian monsoon and ENSO interaction. *East Asian Monsoon*, C.P. Chang, Ed., World Scientific Publishing Company, Singapore, 172–212.
——, and Q. Ding, 2008: Global monsoon: Dominant mode of annual variation in the tropics. *Dyn. Atmos. Ocean.*, **44**, 165–183, doi:10.1016/j.dynatmoce.2007.05.002.
——, R. Wu, and X. Fu, 2000a: Pacific-East Asian teleconnection: How does ENSO affect East Asian climate? *J. Clim.*, **13**, 1517–1536, doi:10.1175/1520-0442(2000)013<1517:PEATHD>2.0.CO;2.
——, ——, and K.-M. Lau, 2001: Interannual Variability of the Asian Summer Monsoon : Contrasts between the Indian and the Western North Pacific – East Asian Monsoons *. *J. Clim.*, **14**, 4073–4090, doi:10.1175/1520-0442(2001)014<4073:IVOTAS>2.0.CO;2.
——, ——, and T. Li, 2003: Atmosphere-warm ocean interaction and its impacts on Asian-Australian monsoon variation. *J. Clim.*, **16**, 1195–1211, doi:10.1175/1520-0442(2003)16<1195:AOIAII>2.0.CO;2.
——, Q. Ding, and J. G. Jhun, 2006: Trends in Seoul (1778-2004) summer precipitation. *Geophys. Res. Lett.*, **33**, doi:10.1029/2006GL026418.
——, J. Yang, T. Zhou, and B. Wang, 2008: Interdecadal changes in the major modes of Asian-Australian monsoon variability: Strengthening relationship with ENSO since the late 1970s. *J. Clim.*, **21**, 1771–1789, doi:10.1175/2007JCLI1981.1.
——, and Coauthors, 2009: Advance and prospectus of seasonal prediction: Assessment of the APCC/ CliPAS 14-model ensemble retrospective seasonal prediction (1980-2004). *Clim. Dyn.*, **33**, 93–117, doi:10.1007/s00382-008-0460-0.
——, J. Liu, H.-J. Kim, P. J. Webster, S.-Y. Yim, and B. Xiang, 2013a: Northern Hemisphere summer monsoon intensified by mega-El Nino/southern oscillation and Atlantic multidecadal oscillation. *Proc. Natl. Acad. Sci.*, **110**, 5347–5352, doi:10.1073/pnas.1219405110. http://www.pnas.org/cgi/doi/10.1073/pnas.1219405110.
——, B. Xiang, and J. Lee, 2013b: Subtropical high predictability establishes a promising way for monsoon and tropical storm predictions. *Proc. Natl. Acad. Sci. U. S. A.*, **110**, 2718–2722, doi:10.1073/pnas.1214626110. http://www.pubmedcentral.nih.gov/articlerender.fcgi?artid=3581955&tool=pmcentrez&rendertype=abstract.
——, J.-Y. Lee, and B. Xiang, 2015: Asian summer monsoon rainfall predictability: a predictable mode analysis. *Clim. Dyn.*, **44**, 61–74, doi:10.1007/s00382-014-2218-1. http://link.springer.com/10.1007/s00382-014-2218-1.
——, J. Li, and Q. He, 2017a: Variable and robust East Asian monsoon rainfall response to El Niño over the past 60 years (1957–2016). *Adv. Atmos. Sci.*, **34**, 1235–1248, doi:10.1007/s00376-017-7016-3.
——, and Coauthors, 2018: Toward predicting changes in the land monsoon rainfall a decade in advance. *J. Clim.*, **31**, 2699–2714, doi:10.1175/JCLI-D-17-0521.1.
Wang, J., B. Yang, F. C. Ljungqvist, J. Luterbacher, T. J. Osborn, K. R. Briffa, and E. Zorita, 2017b: Internal and external forcing of multidecadal Atlantic climate variability over the past 1,200 years. *Nat. Geosci.*, **10**, 512–517, doi:10.1038/ngeo2962.
Wang, P., S. Clemens, L. Beaufort, P. Braconnot, G. Ganssen, Z. Jian, P. Kershaw, and

M. Sarnthein, 2005a: Evolution and variability of the Asian monsoon system: State of the art and outstanding issues. *Quat. Sci. Rev.*, **24**, 595–629, doi:10.1016/j.quascirev.2004.10.002.

Wang, P. X., B. Wang, H. Cheng, J. Fasullo, Z. T. Guo, T. Kiefer, and Z. Y. Liu, 2014: The global monsoon across timescales: Coherent variability of regional monsoons. *Clim. Past*, **10**, 2007–2052, doi:10.5194/cp-10-2007-2014.

Wang, P. X., B. Wang, H. Cheng, J. Fasullo, Z. Guo, T. Kiefer, and Z. Liu, 2017c: The global monsoon across time scales: Mechanisms and outstanding issues. *Earth-Science Rev.*, **174**, 84–121, doi:10.1016/j.earscirev.2017.07.006. https://linkinghub.elsevier.com/retrieve/pii/S0012825216302070.

Wang, S., and Z. C. Zhao, 1979: AN ANALYSES OF HISTORICAL DATA OF DROUGHTS AND FLOODS IN LAST 500 YEARS IN CHINA. *Acta Geogr. Sin.*, **34**, 329–342. http://www.geog.com.cn/CN/10.11821/xb197904005.

——, D. Y. Gong, J. L. Ye, and Z. H. Chen, 2000b: Seasonal Precipitation Series of Eastern China Since 1880 and the Variability. *Acta Geogr. Sin.*, 281–293.

Wang, Y., and Coauthors, 2005b: The holocene Asian monsoon: Links to solar changes and North Atlantic climate. *Science (80-.).*, **308**, 854–857, doi:10.1126/science.1106296.

Webster, P. J., 2006: The coupled monsoon system. *The Asian Monsoon*, 3–66.

Webster, P. J., and S. Yang, 1992: Monsoon and Enso: Selectively Interactive Systems. *Q. J. R. Meteorol. Soc.*, **118**, 877–926, doi:10.1002/qj.49711850705.

Webster, P. J., V. O. Magaña, T. N. Palmer, J. Shukla, R. A. Tomas, M. Yanai, and T. Yasunari, 1998: Monsoons: Processes, predictability, and the prospects for prediction. *J. Geophys. Res. Ocean.*, **103**, 14451–14510, doi:10.1029/97JC02719. http://doi.wiley.com/10.1029/97JC02719.

Webster, P. J., A. M. Moore, J. P. Loschnigg, and R. R. Leben, 1999: Coupled ocean-atmosphere dynamics in the Indian Ocean during 1997-98. *Nature*, **401**, 356–360, doi:10.1038/43848.

Wilson, R., E. Cook, R. D'arrigo, N. Riedwyl, M. N. Evans, A. Tudhope, and A. Rob, 2010: Reconstructing ENSO: The influence of method, proxy data, climate forcing and teleconnections. *J. Quat. Sci.*, **25**, 62–78, doi:10.1002/jqs.1297.

Wu, R., and B. Wang, 2002: A contrast of the East Asian summer monsoon-ENSO relationship between 1962-77 and 1978-93. *J. Clim.*, **15**, 3266–3279, doi:10.1175/1520-0442(2002)015<3266:ACOTEA>2.0.CO;2.

Xu, C., M. Sano, and T. Nakatsuka, 2013: A 400-year record of hydroclimate variability and local ENSO history in northern Southeast Asia inferred from tree-ring δ18O. *Palaeogeogr. Palaeoclimatol. Palaeoecol.*, **386**, 588–598, doi:10.1016/j.palaeo.2013.06.025.

Xu, H., and Coauthors, 2015: Late Holocene Indian summer monsoon variations recorded at Lake Erhai, Southwestern China. *Quat. Res. (United States)*, **83**, 307–314, doi:10.1016/j.yqres.2014.12.004.

Yang, B., S. Kang, F. C. Ljungqvist, M. He, Y. Zhao, and C. Qin, 2014: Drought variability at the northern fringe of the Asian summer monsoon region over the past millennia. *Clim. Dyn.*, **43**, 845–859, doi:10.1007/s00382-013-1962-y.

Yang, F., F. Shi, S. Kang, S. Wang, Z. Xiao, T. Nakatsuka, and J. Shi, 2013a: Comparison of the dryness/wetness index in China with the Monsoon Asia Drought

Atlas. *Theor. Appl. Climatol.*, **114**, 553–566, doi:10.1007/s00704-013-0858-4.
——, N. Wang, F. Shi, F. C. Ljungqvist, S. Wang, Z. Fan, and J. Lu, 2013b: Multi-Proxy Temperature Reconstruction from the West Qinling Mountains, China, for the Past 500 Years. *PLoS One*, **8**, doi:10.1371/journal.pone.0057638.
Yang, S., 1996: Enso-snow-monsoon associations and seasonal-interannual predictions. *Int. J. Climatol.*, **16**, 125–134, doi:10.1002/(SICI)1097-0088(199602)16:2<125::AID-JOC999>3.0.CO;2-V.
Yatagai, A., and T. Yasunari, 1995: Interannual Variations of Summer Precipitation in the Arid/semi-arid Regions in China and Mongolia : Their Regionality and Relation to the Asian Summer Monsoon. *J. Meteorol. Soc. Japan. Ser. II*, **73**, 909–923, doi:10.2151/jmsj1965.73.5_909. https://www.jstage.jst.go.jp/article/jmsj1965/73/5/73_5_909/_article.
Yi, L., H. Yu, J. Ge, Z. Lai, X. Xu, L. Qin, and S. Peng, 2012: Reconstructions of annual summer precipitation and temperature in north-central China since 1470 AD based on drought/flood index and tree-ring records. *Clim. Change*, **110**, 469–498, doi:10.1007/s10584-011-0052-6.
Yim, S. Y., B. Wang, and M. H. Kwon, 2014: Interdecadal change of the controlling mechanisms for East Asian early summer rainfall variation around the mid-1990s. *Clim. Dyn.*, **42**, 1325–1333, doi:10.1007/s00382-013-1760-6.
Zhang, D., 1983: Method to reconstruct climatic series for the past 500 years and its reliability. *Collect. Pap. Meteorol. Sci. Technol.*, **4**, 17–26.
——, and C. Liu, 1993: Continuation (1980-1992) of the yearly charts of dryness/wetness in China for the last 500 years period. *Meteorol. Mon.*, **19**, 41–45.
Zhang, P., and Coauthors, 2008: A test of climate, sun, and culture relationships from an 1810-year Chinese cave record. *Science (80-.).*, **322**, 940–942, doi:10.1126/science.1163965.
Zhang, Q.-B., G. Cheng, T. Yao, X. Kang, and J. Huang, 2003: A 2,326-year tree-ring record of climate variability on the northeastern Qinghai-Tibetan Plateau. *Geophys. Res. Lett.*, **30**, doi:10.1029/2003GL017425. http://doi.wiley.com/10.1029/2003GL017425.
Zhang, R., and T. L. Delworth, 2006: Impact of Atlantic multidecadal oscillations on India/Sahel rainfall and Atlantic hurricanes. *Geophys. Res. Lett.*, **33**, doi:10.1029/2006GL026267.
Zhang, R., A. Sumi, and M. Kimoto, 1996: Impact of El Nino on the East Asian Monsoon: A diagnostic study of the ’86/87 and ’91/92 events. *J. Meteorol. Soc. Japan*, **74**, 49–62, doi:10.1017/CBO9781107415324.004.
Zheng, J., Q. Ge, Z. Hao, H. Liu, Z. Man, Y. Hou, and X. Fang, 2014a: Paleoclimatology proxy recorded in historical documents and method for reconstruction on climate change. *Qua- ternary Sci.*, **34**, 1186–1196.
——, Z. Hao, X. Fang, and Q. Ge, 2014b: Changing characteristics of extreme climate events during past 2000 years in China. *Prog. Geogr.*, **33**, 3–12, doi:10.11820/dlkxjz.2014.01.001.
Zheng, J., Z. Hao, X. Zhang, H. Liu, M. Li, and Q. Ge, 2014c: Drought/flood spatial patterns in centennial cold and warm periods of the past 2000 years over eastern China. *Chinese Sci. Bull. (Chinese Version)*, **59**, 2964, doi:10.1360/N972014-00393. http://csb.scichina.com:8080/kxtb/CN/abstract/abstract515527.shtml.

Zhou, T., D. Gong, J. Li, and B. Li, 2009: Detecting and understanding the multi-decadal variability of the East Asian Summer Monsoon - Recent progress and state of affairs. *Meteorol. Zeitschrift*, **18**, 455–467, doi:10.1127/0941-2948/2009/0396.

Zhu, J., and S. Wang, 2002: 80 yr oscillation of summer rainfall over North China and East Asian Summer Monsoon. *Geophys. Res. Lett.*, **29**, 11–17, doi:Artn 1672\rDoi 10.1029/2001gl013997. http://www.scopus.com/inward/record.url?eid=2-s2.0-0037101724&partnerID=40&md5=cca530d5bb4c63f6f80f61ba05f9a5c7.